ENERGY LOSS DYNAMICS
OF INTENSE HEAVY ION BEAMS
INTERACTING WITH DENSE MATTER

Vom Fachbereich Physik der
TECHNISCHEN UNIVERSITÄT DARMSTADT

zur Erlangung des Grades eines
Doktors der Naturwissenschaften
(Dr. rer. nat.)

genehmigte Dissertation von

Dmitry Varentsov

aus Sankt-Petersburg

DARMSTADT   2002
D 17

In thesis I will try to get my teeth
Into the heating caused by heavy ion
Intensive beam which hard, like lion
Can tear solid target to the death.

ZUSAMMENFASSUNG

Intensive Ionenstrahlen sind herrvorragend geeignet große Volumina von *hoher Energiedichte* (HE) in Materie mit sehr homogenen physikalischen Parametern zu erzeugen. Die experimentelle Erforschung von Materie unter extremen Zuständen von Druck, Temperatur und Dichte ist von hohem Interesse in Gebieten der Grundlagenforschung, der Plasmaphysik, der Bestimmung der Zustandsgleichung von Materie (EOS, *equation of state*), der Astrophysik, der Geophysik, für Trägheitsfusionsanwendungen, sowie zusätzlich für die Auslegung von grundlegenden kernphysikalischen Experimenten.

Ein wichtiges Problem in der Erforschung hoher Energiedichte in Materie ist die Untersuchung der physikalischen Prozesse, die beim Abbremsen intensiver hochenergetischer Ionenstrahlen auftreten. Hohe Energiedichte, die durch intensive Ionenstrahlen in ursprünglich Festkörpertargets erzeugt wird, führt zur Erzeugung von makroskopischen Volumina dichter, stark gekoppelter Plasmen. Aufgrund der hydrodynamischen Antwort der geheizten Materie nimmt die spezifische Dichte des Targets auf der Strahlachse ab und folgendermassen wird auch der Energieverlust der Ionen, die das Target durchlaufen, reduziert. Aus diesem Grund kann die Bestimmung des Energieverlustes des Ionenstrahlpulses während der Wechselwirkungszeit wichtige Informationen über physikalische Prozesse in HE Materie liefern.

Bei der GSI-Darmstadt werden hochenergetische Ionenstrahlen verwendet, um über Wechselwirkung mit Festkörpertargets HE Zustände in Materie zu erzeugen. Eine neue Diagnostiktechnik für HE Experimente, bei der derselbe intensive Strahl hochenergetischer Schwerionen, welcher das Target heizt, dazu verwendet wird Informationen über den Zustand im Innern der Targetmaterie aufzuzeigen, wird hier vorgestellt. Dies geschieht durch Messung der *Energie-Verlust-Dynamik* (EVD) des Ionenstrahles, der die Rückseite des Targets verlässt. Ein neuartiges, zeitauflösendes Energieverlust Spektrometer wurde zu diesem Zweck entwickelt. Dieses Spektrometer, *Scintillations Bragg-Peak Spektrometer* genannt, erlaubt es über einen weiten Bereich Präzisionsmessungen von Ionenstrahlenergiepektren mit ns Zeitauflösung zu messen.

Zum ersten mal wurde die Energieverlustdynamik intensiver Schwerionenstrahlen während der Wechselwirkung mit Materie experimentell beobachtet. EVD Messungen intensiver ($10^8 - 10^{10}$ Ionen/Puls) fokussierter Strahlen von ²³⁸U, ⁸⁶Kr, ⁴⁰Ar und ¹⁸O Ionen mit 150–350 MeV/u Anfangsenergie, die mit festen Edelgastargets, wie Neon bzw. Xenonkristallen wechselwirkten, wurden durchgeführt. Eine signifikante Verringerung des Ionenstrahlenergieverlustes während der Wechselwirkungszeit, basierend auf der schnellen hydrodynamischen Antwort des Targetmaterials, wurde beobachtet.

Um die experimentell beobachteten physikalischen Phänomene interpretieren zu können, wurden theoretische Berechnungen der Energieverlustdynamik durchgeführt. Ein hoch entwickelter, zweidimensionaler Hydrocode (BIG-2), sowie unterschiedliche EOS Modelle für die Edelgaskristalle, insbesondere SESAME (Los Alamos, USA) und ChTEOS (Chernogolovka, Russland), wurden verwendet. Ein Vergleich der Simulationsergebnisse mit gemessenen EVD Daten hat ergeben, dass SESAME in Parameterbereichen, in denen eine korrekte Beschreibung von Phasenübergängen nötig ist, ungenügent exakt ist. Simulationen, die mit ChTEOS durchgeführt wurden, stimmen mit den gemessenen EVD Daten, insbesondere im Fall von Neonkristallen, besser überein.

Wir sind davon überzeugt, dass die entwickelte EVD Diagnostikmethode ein extrem nützliches Werkzeug für HE Experimente darstellt, indem sie experimentelle Daten für die Verifikation von Computer-Hydrodynamik-Codes und den hierbei zugrunde liegenden theoretischen Modellen der Materie zur Verfügung stellt. Die Bestimmung der Energie-Verlust-Dynamik soll als Standarddiagnostikmethode in zukünftigen schwerionenstrahlinduzierten HE Experimenten installiert werden.

SUMMARY

Intense heavy ion beams are an excellent tool to create large volumes of *high energy density* (HED) matter with very uniform physical conditions. Experimental study of matter under extreme conditions of density, temperature and pressure is of considerable interest to fundamental research in the fields of plasma physics, equation-of-state (EOS) of matter, astrophysics, geophysics and for the Inertial Fusion Energy applications as well as for designing basic nuclear physics experiments.

One important problem in high-energy-density matter research is investigation of physical processes that occur during the slowing down of *intense beams* of energetic heavy ions in matter. High energy density induced by an intense heavy ion beam in an initially solid target leads to the creation of macroscopic volumes of dense, strongly coupled plasmas. Due to the fast hydrodynamic response of the heated target material, the line density of the target decreases and consequently the energy loss of the ion beam penetrating through the target is also reduced. Therefore measuring the energy loss of the ion beam during the interaction would provide important information about the physical processes in HED matter.

At the GSI-Darmstadt, intense beams of energetic heavy ions have been used to generate HED states in matter by impact on solid targets. A novel diagnostic technique for the HED matter experiments, where the same intense beam of energetic heavy ions that heats the target material is used to provide information about the physical state of the interior of the target has been proposed. This is accomplished by measuring the *energy loss dynamics* (ELD) of the beam emerging from the back surface of the target. For this purpose, a new time-resolving energy loss spectrometer based on an original principle has been developed. This spectrometer, called *scintillating Bragg-peak* spectrometer allows for wide-range precision measurements of heavy-ion beam energy spectra with nanosecond time resolution.

For the first time the energy loss dynamics of intense heavy ion beams interacting with dense matter has been observed experimentally. The ELD measurements of intense ($10^8 - 10^{10}$ particles/pulse) focused beams of ^{238}U, ^{86}Kr, ^{40}Ar and ^{18}O ions with 150–350 MeV/nucleon initial energy interacting with rare-gas solid (RGS) targets, such as solid **Ne** and solid **Xe** have been carried out. A significant reduction in the ion beam energy loss during the interaction has been recorded which is due to the rapid hydrodynamic response of the ion-beam heated target matter.

In order to interpret the experimentally observed physical phenomena, theoretical calculations of the energy loss dynamics have been performed. For these calculations a sophisticated two-dimensional hydrodynamic code BIG-2 has been employed as well as different EOS models for the RGS target materials, namely, the SESAME (Los Alamos, USA) and ChTEOS (Chernogolovka, Russia). A comparison of the simulation results and the measured ELD data has shown that the SESAME EOS tables for RGS materials have a limited accuracy in certain parameter regimes where a correct description of the phase transitions is essential. The simulations performed with the ChTEOS model are in better agreement with the experimental ELD data, in particular for solid **Ne** targets.

We believe that the developed ELD diagnostic technique is an extremely useful tool for HED matter experiments, providing experimental data for verification of hydrodynamic computer codes and underlying theoretical models. The ELD measurements will be employed as a standard diagnostics in future experiments on investigation of the HED matter induced by intense heavy ion beams.

Table of Contents

Abbreviations and symbols used

AMeV	*MeV per nucleon*
DA	*Differential Algebra*
ELD	*Energy Loss Dynamics*
EOS	*Equation of State*
FWHM	*Full Width at Half Maximum*
GSI	*Gesellschaft für Schwerionenforschung, Darmstadt, Germany*
HED	*High Energy Density*
HI-HEX	*Heavy Ion Heating and Expansion*
HIPP	*Heavy Ion Plasma Physics*
IFE	*Inertial Fusion Energy*
IPCP	*Institute for Problems of Chemical Physics, Chernogolovka, Russia*
PL	*Plasma Lens*
RGS	*Rare Gas Solid*
SBP	*Scintillating Bragg-peak (spectrometer)*

$\mathcal{E}$	*specific deposited energy*
$\mathcal{F}_\mathrm{E}(E)$	*energy distribution function*
$\mathcal{F}_\mathcal{R}(\mathcal{R})$	*range distribution function*
Γ	*plasma nonideality (coupling) parameter*
$I(x,t)$	*specific luminescence profile*
$\mathcal{L}$	*stopping (Coulomb) logarithm*
$\mathcal{R}$	*ion range*
$\mathcal{R}_\mathrm{sc}$	*ion range in a scintillator*
$\mathcal{S}$	$= -\frac{dE}{dx}$ — *stopping power*
$\mathcal{S}_\mathrm{sc}$	*stopping power of a scintillator*
v_0	$= \alpha \cdot c$ — *Bohr velocity*
$\bar{Z}_p$	*ion charge state*

List of Figures

1   Introduction

Experimental and theoretical investigations on interaction processes of energetic heavy ions with matter remain a traditional subject of research for atomic and nuclear physics. A special place among these studies is devoted to an important practical application, Inertial Fusion Energy (IFE). At present, much research work is being carried out in the field of heavy-ion beam driven IFE all over the world. The main purpose of this research is the investigation of basic physical phenomena involved in designing future IFE targets and drivers. Recent developments in heavy-ion driven IFE stimulated and promoted other fundamental physical studies such as the investigation of properties of matter at high-energy-density (HED) states and dense nonideal plasmas.

Intense heavy ion beams are a very efficient tool to create large volumes of HED matter with very uniform physical conditions. Matter under extreme conditions of density, temperature and pressure is frequently found in extraterrestrial objects such as stars and giant planets. HED matter can have super-solid densities, temperatures of the order of millions of Kelvin and pressures in the range of megabars. Experimental study of the HED matter is of considerable interest to basic research on the equation of state (EOS) properties of matter, thermodynamic and hydrodynamic behavior of dense plasmas. Such experiments will enable one to probe the validity of existing theories on stellar formation and evolution, compressibility of inertial fusion targets and existing models for strongly coupled high density plasmas. These phenomena are related to the field of plasma physics, astrophysics, geophysics and planetary sciences.

One important problem in HED and IFE research is the investigation of physical processes that take place during the slowing down of *intense beams* of energetic heavy ions in matter. High energy density deposited by an intense heavy ion beam in an initially solid target leads to the creation of macroscopic volumes of dense nonideal plasma. However, due to fast hydrodynamic response of the heated target material the line density of the target decreases. This leads to a reduction in the energy loss of the beam penetrating through the target. Therefore, measuring the *energy loss dynamics* (ELD) of the ion beam during the interaction with a target provides important information about physical processes in HED matter. Investigation of the energy loss dynamics of intense heavy ion beams interacting with dense matter is subject of the present work.

Besides the motivation for HED matter physics and IFE applications, the ELD studies are also important for fundamental nuclear physics experiments. Presently, in many research laboratories world-wide (for example, GSI-Darmstadt in Germany, MSU in USA, RIKEN in Japan, GANIL and LPS Caen in France, CERN in Switzerland and many others) research projects for experiments with accelerated radioactive beams are proposed. In order to generate a sufficient number of radioactive nuclei for experiments, an intense primary heavy ion beam is required. During the interaction of such an intense ion beam with a target, the same processes as in heavy-ion beam induced HED matter experiments take place: due to

a high deposition power, the line density of the target and accordingly, the energy loss of the primary ions is decreasing during the interaction. Since the energy of the secondary particles is directly related to the energy of the primary ions, the hydrodynamic response of the ion-beam heated target matter will lead to a significant additional broadening of the secondary beam energy spectrum. At the same time, the energy acceptance of ion-optical systems which are used for separation, transport and further acceleration of radioactive beams is usually not more than a few percent. Therefore, investigation of the ELD of intense heavy ion beams interacting with dense matter is an important subject for the design of basic nuclear physics experiments.

By the time this study had started, no experimental information on the energy loss dynamics of intense heavy ion beams interacting with dense matter was available. All the previous experimental work described the stopping power of matter neglecting the influence of the ion beam on the target conditions and therefore, change of the energy loss during the interaction is not considered. On the other hand, the theoretical calculations of the ELD are very complicated. In such calculations, besides the simulation of all relevant hydrodynamic processes in the ion-beam heated target matter, a detailed model for the equation-of-state of the target material at extreme conditions, which must include all the possible phase transitions (up to plasma phase transition) is needed. However, the presently available wide-range EOS models have a limited accuracy in certain parameter regions, especially for relatively low (below 1 eV) temperatures and high densities. Thus an experimental verification of hydrodynamic codes and underlying theoretical models, such as EOS of high-energy-density matter, is a very important task.

The heavy ion synchrotron SIS-18 at the Gesellschaft für Schwerionenforschung (GSI, Darmstadt) is a unique facility worldwide that delivers intense beams of highly energetic heavy ions. Using these heavy ion beams, it is possible to heat rather large volumes of matter at solid state density to extreme conditions of temperature and pressure. The present ELD experiments have therefore been carried out at the HHT ("high temperature") experimental area of the plasma physics group at GSI.

In chapter 2 an overview of the research carried out previously in the fields related to the present work is given. These fields include atomic processes occurring during slowing down of heavy ion beams in matter as well as the effects related to high energy density states that can be induced in the target material by intense beams. Heating of the target by intense, focused heavy ion beams can induce exotic HED states in matter and generate extended volumes of dense plasmas in initially solid material. In this chapter the idea of measuring the energy loss dynamics (ELD) of intense heavy ion beams is introduced which can serve as an excellent diagnostic tool in HED matter experiments.

In addition, in this chapter previous experimental and theoretical work on a new generation of high-current pulsed magnetic lenses is reviewed. These devices can be an attractive alternative to conventional steel-dominated or superconducting magnets as to be used in the construction of a magnetic spectrometer for ELD measurements as well as for other applications, such as strong final focusing systems and beam transport lines.

Chapter 3 introduces the GSI accelerator facilities, the HHT experimental area, ion beam and target diagnostic methods as well as target preparation issues relevant to the ELD experiments.

In chapter 4 a new technique to measure the energy loss of intense heavy ion beams with time resolution is described. In this technique the effects of complete slowing down of a beam in the bulk of fast scintillating medium are employed. Based on this principle, a new simple and elegant time-resolving spectrometer which is called *scintillating Bragg-peak* (SBP) spectrometer has been developed. Different constructions of this instrument along with a mathematical model and a computer code developed for the data processing are described.

In chapter 5 the results of recently performed ELD experiments as well as computer simulations of the observed phenomena are presented. In the first section, the ELD experiments that have been carried out with different heavy ion beams and different target materials are described. The second section of this chapter is devoted to theoretical calculations of the experimentally observed physical phenomena. A comparison of the simulation results and the experimental data is also provided.

Finally, in Chapter 6 the conclusions drawn from this study are noted, outlining the main results. Possible future extensions of the work are also suggested.

2 Review of the field

In this chapter an overview of the research carried out previously in the fields relevant to the work presented in this thesis is given. These fields include atomic processes occurring during slowing down of heavy ion beams in matter as well as the effects connected to high energy density states that can be induced in the target material by intense beams. Some basic theoretical concepts of the energy loss of relativistic heavy ions due to ionization of the medium and related effects are discussed with emphasis on their application to the present work. Specific aspects of the interaction of highly energetic ion beams with dense target matter are addressed as well. Heating of the target by intense focused heavy ion beams can induce exotic high-energy-density (HED) states in matter and generate dense plasma in extended volumes of initially solid material. This will lead to new interesting target related phenomena like hydrodynamics. This issue is an important subject of study for the *heavy ion plasma physics (HIPP)* research, which has rapidly developed over the past two decades. Finally, the idea to measure the *energy loss dynamics (ELD)* of intense heavy ion beams is introduced. The ELD measurements can serve as an excellent diagnostic tool for high-energy-density matter created by intense heavy ion beams. The advantages of the ELD diagnostics as well as the special requirements and challenges in developing an appropriate instrument for such measurements are discussed.

2.1 Penetration of heavy ions through matter

The subject of penetration of energetic heavy ions through matter has fascinated generations of physicists over the past many decades because of its applications to basic and applied sciences as well as to industry. As a result, there has been a continuous effort among the scientific community to improve the understanding of various complex physical processes that are involved in such beam-matter interactions. These include the dissipation of energy of the projectile ions due to

interaction with bound and free electrons of the target matter, elastic and inelastic nuclear collisions and evolution of the charge-state distribution of the projectile ions. The momentum transfer to the target nuclei in elastic (Coulomb) nuclear collisions is small compared to the electronic energy loss because of the mass ratio factor, m_e/m_i, and for projectile energies above 0.1–1 AMeV[1] it can be neglected. Therefore, the energy transfer to the target electrons is the dominating mechanism of the projectile energy loss in this energy region. Influence of inelastic nuclear collisions (nuclear reactions) on the slowing down of a heavy ion beam in the medium will be briefly discussed in sec. 4.3.4.

The energy loss of projectile particles to electrons may be separated into two parts, namely, energy loss due to the bound electrons and the energy loss due to the free electrons. The first process is called *cold stopping* whereas the latter is important when slowing down of an ion beam takes place in a pre-ionized (hot) material, such as plasma (*plasma effects*). Theoretical aspects of the cold electronic stopping will be addressed in the following section while the stopping power of hot matter due to free electron contribution in an ideal as well as in a non-ideal (dense, strongly-coupled) plasmas will be briefly discussed in sec. 2.1.2.

2.1.1   Cold stopping

The theory of cold electronic stopping has been developed in many parts, since there are many physical processes which must be included in a complete description of the energy loss. Numerous review articles on this subject have been published over the past decades (see, e. g., [Ahl80, Sch97, Sig98, Wei00a, Wea02] and references therein). Theoretical and experimental papers on this subject are still being published (e. g., [Sch98a, Zhu00, Sig02]), indicating that this field of research is still developing and attracting serious attention. In this section the theoretical aspects of these physical phenomena will be briefly addressed on qualitative basis.

The overall form of an expression describing the electronic energy loss of an ion in a medium can be obtained from classical arguments [Jac75], considering the momentum transfer to a target electron in a Coulomb potential, or by integrating the differential Rutherford scattering cross section [Rut11], $\mathcal{S} = n_e \int d\sigma \cdot \Delta E$. In SI units this expression for *stopping power* $\mathcal{S}$ can be written as:

$$-\frac{dE}{dx} \equiv \mathcal{S} = \frac{e^4}{4\pi\epsilon_0^2} \frac{\bar{Z}_p^2 \, n_e^{\mathrm{bound}}}{m_e \, v^2} \, \mathcal{L} \, . \tag{2.1}$$

Here $\bar{Z}_p$ is the charge of the projectile ion (in case of bare ions $\bar{Z}_p = Z_p$, where Z_p is the atomic number), $v = \beta c$ is ion velocity, m_e and n_e^{bound} are the electron mass and number density of bound electrons, respectively. The minus sign on the left-hand side indicates that the formula gives the energy *lost* by the particle. The factor $\mathcal{L}$ is the so-called *stopping logarithm* or *stopping number*. This factor appears from integrating the Rutherford cross section over all impact parameters. Since the integrated Rutherford cross section is diverging for infinite impact parameters, the limiting value of b_{max} has to be chosen. Therefore the stopping logarithm is defined classically by

$$\mathcal{L} = \ln \frac{b_{\mathrm{max}}}{b_{\mathrm{min}}}, \tag{2.2}$$

---

[1]The "AMeV" abbreviation is to be read here and thereafter as "MeV per nucleon".

where $b_{\max}$ and $b_{\min}$ are the maximum and minimum impact parameters, respectively.

Qualitatively, the behavior of the stopping power as a function of ion energy is as follows. Starting from very low energies the stopping power is rapidly increasing with the increase in projectile velocity. When the velocity of the ion approaches the average orbital velocities of the target electrons, the momentum transfer is most efficient and the stopping power curve has a maximum at about 1–10 AMeV (see Fig. 2.1). This velocity can be compared with the Tomas-Fermi estimate for the mean electron orbital velocity $v_{\mathrm{TF}} = Z_t^{2/3} v_0$, where $v_0 = e^2/4\pi\epsilon_0\hbar = \alpha \cdot c$ is the Bohr velocity, $\alpha \approx 1/137$ is the usual fine-structure constant and c is the speed of light in vacuum. At higher energies ($v > v_{\mathrm{TF}}$) the electronic stopping power is decreasing again as $\mathcal{S} \propto v^{-2\mu}$, where $\mu \approx 0.6 - 0.8$. At the ultra-relativistic limit of the projectile velocities ($E_0 \geqslant 100\,\mathrm{AGeV}$) the stopping power becomes energy independent due to the relativistic "finite nuclear size" effect which efficiently reduces the stopping number for ultra-relativistic energies as discussed below. Typical $\mathcal{S}(E)$ function is plotted in Fig. 2.1 for a wide energy range in logarithmic scale. The stopping power calculated for the intermediate energy region ($E_0 < 500\,\mathrm{AMeV}$) can also be seen in Fig. A.1, p. 92.
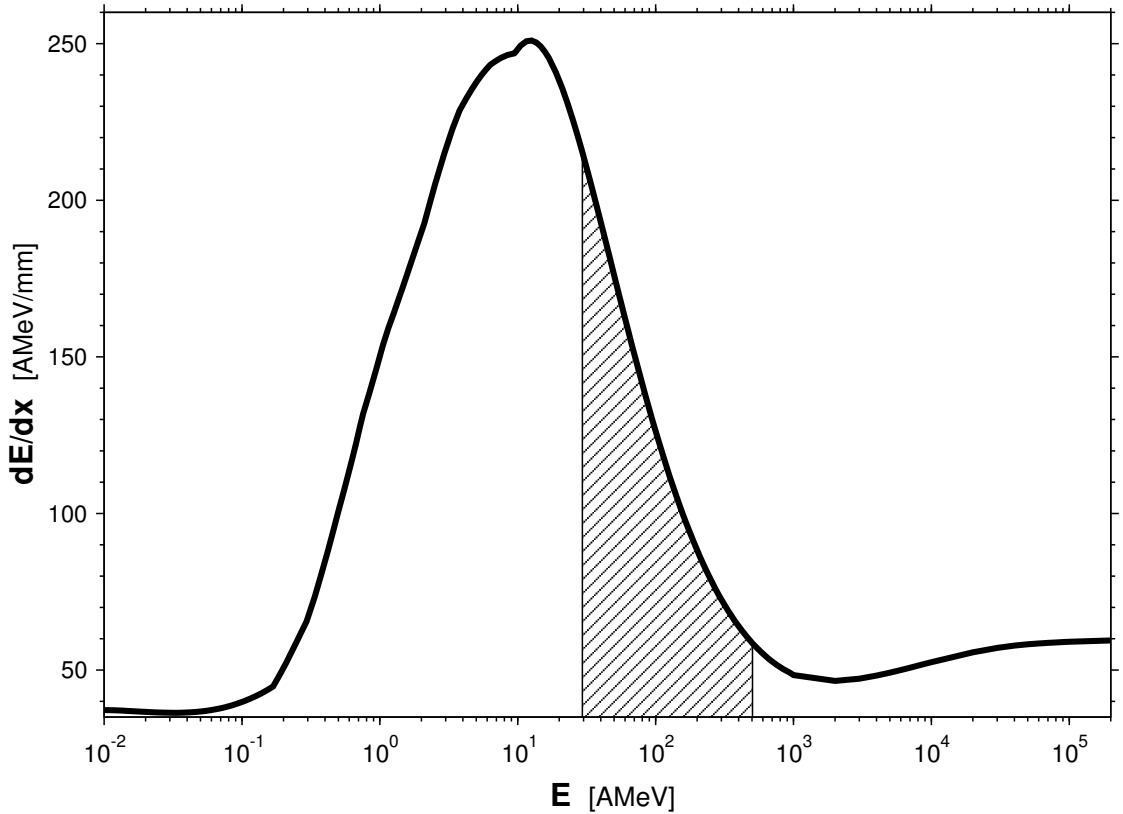
Figure 2.1: Stopping power of lead to ²³⁸U ions over a wide energy range calculated with SRIM and CRANGE codes (see sec. 2.1.1.3, p. 15). The *intermediate energy region* ($30 < E_0 < 500\,\mathrm{AMeV}$) is marked.

The penetration depth of an ion with initial energy E_0 in a medium until it is completely stopped is called the *range.* The range is related to the stopping power of the medium as

$$\mathcal{R}(E_0) = \int_0^{E_0} \mathcal{S}^{-1}\, dE. \tag{2.3}$$

If the stopping power $\mathcal{S}(E)$ given by Eq. (2.1) is known, a simple integration should yield the range as a function of the initial ion energy, E_0. For sufficiently large energies the range-energy dependence can be approximated by a simple power relation $\mathcal{R} \propto E^{\mu+1}$ (see, e. g. Fig. A.3, p. 94).

Specific energy loss of an ion as a function of its penetration depth in the target, $\mathcal{S}(x)$ or the *energy deposition profile* can also be calculated by integrating Eq. (2.1), provided the stopping power is known: $\mathcal{S}(x) = \mathcal{S}(E(x))$, where the energy of the ion E at the depth x can be obtained from $x = \int_E^{E_0} S^{-1} dE'$. The dependence $S(x)$ is called *Bragg-curve*. The specific energy loss $\mathcal{S}(x)$ is increasing with the penetration depth until $x \approx \mathcal{R}(E_0)$, where it has a characteristic sharp maximum, called the *Bragg-peak* and where an ion deposits the rest of its energy and is stopped.

The devil, they say, is in the details [Wea02]. In this case the details are the stopping number $\mathcal{L}$ and the charge state of the projectile $\bar{Z}_p$. Taking into account various physical effects relevant in different regions of projectile velocity lead to numerous corrections to the value of the stopping number. It is therefore impossible to obtain a "universal" analytic expression for the stopping number valid for an arbitrary projectile velocity.

If the initial energy of a heavy ion is below 1 AGeV, the charge exchange between the projectile ion and the target media becomes important. These effects are most pronounced for the heaviest ions: a uranium ion with the energy of several hundred AMeV still carries a few electrons while penetrating through matter. The equilibrium charge state of a heavy ion beam during the slowing down in a media will be changing from $\bar{Z}_p = Z_p$ at sufficiently high initial energies down to $\bar{Z}_p \approx 0$ near to the stopping maximum. Since the stopping power, $\mathcal{S}$ scales with Z^2, the charge-changing processes affect the stopping power significantly.

2.1.1.1   Stopping logarithm

Following the work of Lindhard [Lin96] the stopping number is defined as

$$\mathcal{L} = \mathcal{L}_{\text{Bethe}} + \Delta\mathcal{L}, \qquad (2.4)$$

where the result by Bethe, $\mathcal{L}_{\text{Bethe}}$ is used as a "standard formula" and $\Delta\mathcal{L} = \sum \delta\mathcal{L}$ is the sum of various corrections to the stopping number. The expression for the $\mathcal{L}_{\text{Bethe}}$ as well as the qualitative description of the corrections will be given below.

For the discussion about the stopping number and its corrections it is useful to define the quantity

$$\eta \equiv \frac{Z_p \alpha}{\beta} = \frac{Z_p v_0}{v} \equiv \frac{1}{2}\kappa, \qquad (2.5)$$

called the *Sommerfeld parameter* [Sch97], whereas the same quantity $\kappa = 2\eta$ is also called *Bohr parameter* [Lin96]. The Sommerfeld parameter characterizes regions of applicability for different approaches to calculate the stopping number and is often used as a "small number" in relativistic corrections for the stopping logarithm. If $\eta \ll 1$, the quantum perturbation theory can be applied, whereas $\eta \gg 1$ permits a classical treatment.

For the case of heavy ions and moderate ion energies one cannot assume $\eta \ll 1$. For example, for uranium ($Z_p = 92$), Sommerfeld parameter $\eta > 1$ when $\beta < 0.67$ or, equally, when $E_0 < 320\,\text{AMeV}$. Thus any expression which assumes η to be small will be hopeless for describing the energy loss of heavy ions in this energy region.

Another meaning for the Sommerfeld parameter is that ions for which $\eta > 1/2$ will also carry electrons, involving processes of capture and loss. Therefore for large values of η the charge exchange processes have to be taken into account to calculate a correct value of $\bar{Z}_p$.

In this work the stopping of heavy ions ranging from $^{40}\textbf{Ar}$ to $^{238}\textbf{U}$ ($18 \leqslant Z_p \leqslant 92$) in the intermediate region of initial kinetic energies, $E_0 \sim 30 - 500\,\text{AMeV}$ is important. This corresponds to $0.25 < \beta < 0.75$ and $0.17 < \eta < 2.7$.

The first study on the stopping process of ions in matter has been carried out by N. Bohr. In his pioneering work [Boh13], Bohr obtained valuable expressions for the electronic stopping power and straggling as well as mean ranges and fluctuations. His calculations have been made entirely on the basis of classical mechanics including relativistic corrections, since the quantum mechanics was not yet developed at those times. From the point of view of the modern theory, the Bohr's result is valid when $0.5 < \eta \ll Z_p^{2/3}$.

Bethe's result ($\mathcal{L}_{\textbf{Bethe}}$). On the basis of Bohr's concepts, H. Bethe solved the problem quantum mechanically in first-order Born approximation, whereby the entire system, projectile ion – target atom is considered within quantum theory [Bet30]. In Bethe's approach the collisions are characterized by momentum transfer rather than by impact parameter, as in Bohr's theory. His result for the stopping number, later extended to relativistic energies [Bet32, Fan63, Jac75] can be written as

$$\mathcal{L}_{\textbf{Bethe}} = \ln\left(\frac{2m_e\,c^2\,\beta^2\gamma^2}{I}\right) - \beta^2. \tag{2.6}$$

Here $\gamma = (1 - \beta^2)^{-1/2}$ is the Lorentz factor and I is the effective ionization potential of the target material. Although there are theoretical means to determine I, the experimentalists usually regard it as an empirical parameter.

The expression Eq. (2.6) is obtained using relativistic quantum perturbation theory. Strictly speaking, it is valid only when $\eta \ll 1$. In addition to that, $\mathcal{L}_{\textbf{Bethe}}$ does not depend on the charge number Z_p of the projectile, implying that $\mathcal{S} \propto Z_p^2$, as a consequence of using the first-order Born approximation only. Therefore it was soon noted, that corrections to the Bethe formula (Eq. (2.6)) are necessary [Blo33] to explain experimental values precisely. Some of these corrections are discussed below.

Bloch correction ($\delta\mathcal{L}_{\textbf{Bloch}}$). F. Bloch investigated the similarities and differences between classical Bohr's ($\eta \gg 1$) and quantum-mechanical Bethe's ($\eta \ll 1$) approaches [Blo33]. He showed that independent of the projectile charge, a first-order perturbation treatment is sufficient for the distant collisions since odd terms in Z_p cancel and higher-order contributions of even terms are negligible. However, he noticed that for small impact parameter (close collisions) the exact scattering amplitudes for a Coulomb field must be used rather than those of the Born approximation. This leads to the co-called *Bloch's correction*[2]:

$$\delta\mathcal{L}_{\textbf{Bloch}} = \psi(1) - \text{Re}\,\psi(1 + i\eta), \tag{2.7}$$

where $\psi(z) \equiv \frac{d}{dz}\ln\Gamma(z)$, the logarithmic derivative of the complex gamma-function, $\psi(1) \approx -0.5772157$ is the negative Euler's constant. When the Sommerfeld parameter is small, the Bloch correction can be approximated to $\delta\mathcal{L}_{\textbf{Bloch}} \simeq -1.202\,\eta^2$ ($\eta \ll 1$).

---

[2]The details can be found in [Ahl80]

Since Bloch correction accounts for a saturation of energy transfer in close collisions, $\delta\mathcal{L}_{\text{Bloch}}$ is negative. The formula Eq. (2.7) is obtained for the non-relativistic case. The discussion by Bloch [Blo33] bridges the gap between the classical and quantum-mechanical treatments while his result reduces to Bohr and Bethe formulas at the limits $\eta \gg 1$ and $\eta \ll 1$, respectively.

Mott correction ($\delta\mathcal{L}_{\text{Mott}}$). Corrections to the stopping power of the order higher than Z_p^2 at high energies first became apparent a few decades ago [Jac72, Lin76]. During recent years there were a number of experimental indications that Z_p-dependence of stopping power and total range of relativistic heavy nuclei with $Z_p > 50$ appreciably deviate from the simple Z_p^2-scaling (see [Bog99, Zhu00] and references therein). For example, in the recent work by Bogdanov and Zhurkin [Zhu00] the total ranges of different heavy ions (from ^{40}**Ar** to ^{238}**U**) at the energy $E_0 \sim 1\,AGeV$ have been precisely measured in nuclear emulsions. It has been demonstrated that neglecting the higher-order Z_p corrections leads to a systematic deviation (up to 10 %) between the measured and calculated values of ion ranges.

The origin of this correction is the failure of the first Born approximation in the description of the close collisions for relativistic velocities of the projectile. In the treatments by Bohr, Bethe and Bloch, the Rutherford differential scattering cross section[3] has been used, i. e. the cross section of free electrons scattering off nuclei, neglecting initial electron binding energy in the case of large energy transfer. However, for large nuclear charges and sufficiently high velocities one requires the elastic scattering cross section for a relativistic electron off a point nucleus located at the origin. Such calculations within the framework of the Dirac theory of relativistic electron without any restriction on the atomic number of a nucleus was first given by N.F. Mott [Mot29, Mot32]. The exact (Mott) cross section differs significantly from the scattering cross section in Born approximation for large scattering angles, when Z_p and β are large.

An analytic expression for the $\delta\mathcal{L}_{\text{Mott}}$ correction to the stopping logarithm derived using a parametrization of the Mott cross section is given by Ahlen [Ahl80]. As one can expect, the Mott correction $\delta\mathcal{L}_{\text{Mott}}$ vanishes as $Z_p \to 0$ or $\beta \to 0$ and its sign depends on the sign of the projectile charge. If η is assumed to be a small parameter, in the first order, the Mott correction $\delta\mathcal{L}_{\text{Mott}} \propto \eta\beta^2$ but also contains higher-orders with respect to Z_p and β (up to Z_p^7). It is recommended [Ahl80] that the Mott correction is used only when $\eta < 0.73$.

Relativistic Bloch (Ahlen) correction ($\delta\mathcal{L}_{\text{Ahlen}}$). It has been experimentally demonstrated [Ahl83] that the Bloch correction is inadequate for relativistic heavy ions, i. e. in regimes of both high charge Z_p and high velocity β. An additional relativistic correction to the Bloch correction is necessary, especially when η cannot be assumed small, which is the case for heavy ions, even at relativistic velocities. This was first calculated by Ahlen [Ahl82]. A useful expression for the $\delta\mathcal{L}_{\text{Ahlen}}$ correction in given in [Wea02].

---

[3]The Rutherford differential scattering cross section [Rut11] which describes the scattering of a free charged particle in the Coulomb potential, remains, amazingly, the same whether obtained by classical theory, first Born quantum approximation or exact quantum-mechanical theory. As it was shown by Lindhard and Søresen [Lin96], in all cases where the location in space of the scattering process is immaterial, one can use the simple Rutherford formula $d\sigma = \frac{Z_p^2 e^4}{2m_e v^4} \frac{d\Omega}{\sin^4 \frac{\theta}{2}}$.

Following the review by Weaver [Wea02], the Bloch, Mott and Ahlen corrections are called the *BMA group* because their common thread of development and the necessity for all three to be included together for precision calculations:

$$\delta\mathcal{L}_{\mathrm{BMA}} \equiv \delta\mathcal{L}_{\mathrm{Bloch}} + \delta\mathcal{L}_{\mathrm{Mott}} + \delta\mathcal{L}_{\mathrm{Ahlen}}. \tag{2.8}$$

Lindhard-Søresen correction ($\delta\mathcal{L}_{\mathrm{LS}}$). Recently, Lindhard and Søresen have introduced an outstanding work on the electronic stopping power [Lin96]. They have performed rigorous treatment of the problem using their transport cross section method. Practically all the previously obtained results on the stopping, including that by Bohr, Bethe, Bloch, Ahlen and others have been re-derived and re-analyzed on base of a unified approach. As a result of this study they have calculated the deviation of the relativistic stopping for heavy ions from first-order quantum perturbation theory in a simple manner, formulating a correction, $\delta\mathcal{L}_{\mathrm{LS}}$ to the Bethe formula. Another noticeable consequence of this work was that the slowing down of highly relativistic heavy ions is affected by the nuclear charge distribution of the projectiles. This lead to a new important correction to the stopping number, $\delta\mathcal{L}_{\mathrm{FNS}}$ which is discussed later.

The Lindhard-Søresen correction, $\delta\mathcal{L}_{\mathrm{LS}}$, *replaces* the BMA group, $\delta\mathcal{L}_{\mathrm{BMA}}$. It has been shown, that the low-energy limit of the LS correction is *exactly* the Bloch correction. Furthermore, by using exact solution of the Dirac equation, the LS correction automatically incorporates Mott scattering and is relativistically correct. The formulas for $\delta\mathcal{L}_{\mathrm{LS}}$ are given in the original paper [Lin96] as well as in the paper by Weaver [Wea02] in a simplified form that can be used for calculations. The comparison of the recent experimental results on stopping of relativistic heavy ions with the calculations using the LS-theory (see, e. g., [Sch97, Zhu00, Wei00a] and others) shows an excellent agreement for the intermediate energy region as well. Therefore it is recommended [Sch01b] that the Lindhard and Søresen formulas shall be used for the stopping calculations for relativistic heavy ions.

Density effect ($\delta\mathcal{L}_{\mathrm{dens}}$). In dense media, the field which perturbs electrons far from the projectile track is modified by the dielectric polarization of the atoms between the distant electron and the projectile. The energy transfer in distant collisions is therefore less effective. This effect is called the *density effect.* Unlike many high-energy corrections, the density effect can be at least qualitatively derived in classical electrodynamics [Jac75]. The magnitude of the density effect was originally calculated by Fermi [Fer40] and extended by Sternheimer and Peierls [Ste71]. At high energies ($\gamma \geqslant 100$), the density effect correction has the form

$$\delta\mathcal{L}_{\mathrm{dens}} = -\frac{\delta}{2} = -\ln(\beta\gamma) + \ln\frac{I}{\hbar\omega_p} + \frac{1}{2}. \tag{2.9}$$

The density effect reduces the relativistic rise of the stopping power from $\propto \ln\gamma^2$ to $\propto \ln\gamma$ and substitutes the plasma frequency of the medium, ω_p, which depends on the target density, for the mean ionization potential (see Eq. (2.6)). At lower energies the expression for the $\delta\mathcal{L}_{\mathrm{dens}}$ is more complicated but a parametrization formula can be obtained [Ste71]. For the intermediate energy region ($\beta < 0.75$) the density effect correction is small.

Barkas correction ($\delta\mathcal{L}_{\mathrm{Barkas}}$). The Barkas effect was first noticed as a difference in energy loss between positive and negative pions [Bar63], indicating that the energy

loss contained odd powers of Z_p. The reason is the dynamical screening which leads to a reduced effective collision velocity [Lin76]. The dominating term of the Barkas correction behaves as Z_p^3 and the correction is important in both classical and quantum descriptions [Lin96]. However, the relative contribution of $\delta\mathcal{L}_{\text{Barkas}}$ to the stopping number decreases as $1/\beta^3$ and thus the Barkas effect is important only at low velocities [Sch97]. It is practically negligible for the intermediate and high energy regions ($E_0 \geqslant 20\,AMeV$).

Shell correction ($\delta\mathcal{L}_{\text{shell}}$).   Since the Bethe formula Eq. (2.6) was derived using the first-order Born approximation, it is valid only for $\eta \ll 1$. At very low projectile velocities $\mathcal{L}_{\text{Bethe}}$ becomes negative. Furthermore, the validity of Bethe formula relies on the assumption that the speed of the incident particle is much greater than that of the bound target electrons [Fan63]. This however is not the case when either the projectile velocity is low enough or when the inner shell electrons have relativistic velocities in heavy target atoms. The latter restriction can be avoided by calculating the stopping power correctly even within the framework of the first Born approximation [Ahl80]. The shell correction is then usually expressed in the form $\delta\mathcal{L}_{\text{shell}} = -C/Z_t$ where C is a complicated function of various parameters. In the first order $C \propto 1/\beta^2$ and is always independent of Z_p. Since most other correction terms scale as positive power of Z_p, it is probably reasonable to assume that the shell correction is less important as the other low-energy corrections (such as the Barkas term) at low projectile velocities [Wea02]. For the intermediate and high energy regions the shell correction can safely be ignored [Sch97].

Finite nuclear size correction ($\delta\mathcal{L}_{\text{FNS}}$) and ultrarelativistic limit.   Another important consequence from Lindhard and Søresen theory [Lin96] is a correction due to the finite size of the projectile nuclei. When the de Broglie wavelength of an electron in the rest frame of the projectile ion ($\lambda = h/\gamma m_e c$) becomes comparable to the nuclear size $R \approx 1.18 A^{1/3}$ fm (i. e., when $\gamma A^{1/3} \simeq 160$), calculations of electron scattering by the Coulomb potential of a point charge $Z_p e$ are not accurate. Instead, one has to consider nuclei with finite radii and to perform precise quantum mechanical calculations for Dirac electrons scattered by a spherically symmetric potential. As it has been shown by Lindhard and Søresen, taking into account this effect leads to a cutoff of momentum transfers at about h/R. This gives a significant reduction in stopping number and for heavy ions the $\delta\mathcal{L}_{\text{FNS}}$ correction has to be considered when the Lorentz factor, $\gamma > 10$.

In the ultrarelativistic limit, the $\delta\mathcal{L}_{\text{FNS}}$ correction cancels the correction due to the density effect, $\delta\mathcal{L}_{\text{dens}}$ (Eq. (2.9)) and the entire stopping logarithm becomes

$$\mathcal{L} = \mathcal{L}_{\text{Bethe}} + \Delta\mathcal{L} \xrightarrow[\beta \to 1]{} \ln 1.64 \frac{c}{R\omega_p}. \tag{2.10}$$

In this limit $\mathcal{L}$ does not depend on energy and depends only very weakly on target and projectile parameters, having values $\mathcal{L} \approx 14$ in condensed matter [Lin96]. The physical interpretation of Eq. (2.10) is that the impact parameters range from a minimum $b_{\text{min}} \sim R$ to a maximum $b_{\text{max}} \sim c/\omega_p$. The prediction of an energy-independent energy loss in the ultrarelativistic regime has been confirmed by using the 160 AGeV **Pb** ions ($\gamma = 168$) at the CERN SPS accelerator [Dat96].

Other effects.   Besides the above corrections, there are other minor effects that influence the energy loss of a projectile. For example, a projectile ion can lose

energy emitting bremsstrahlung radiation in the effective field of the target nuclei [Hei54]. The stopping due to the bremsstrahlung scales as $Z_p^4 \gamma$, although ion bremsstrahlung is suppressed relative to electron bremsstrahlung by factor $(m_e/m_i)^2$.

Similar to the above mentioned finite nuclear size correction, $\delta\mathcal{L}_{\mathrm{FNS}}$ which is important for ultrarelativistic projectile velocities, in the intermediate energy range, the de Broglie wavelength of the scattered target electron, as measured in the projectile rest frame, may become comparable to the size of projectile atom. This means that the electron will probe the true charge distribution of the projectile and scattering will be different from that due to a point charge. Taking into account this effect for close collisions of not fully stripped projectiles gives an additional correction to the stopping number [Wei02, Sør02]. However, for example for H-like uranium ions with energies up to 1 AGeV, this correction to the stopping logarithm would not exceed 0.5 % [Wei02]. At higher energies the projectile ions are fully stripped and this effect is canceled.

Other effects that may be considered are pair production ("sparking the vacuum") which is basically a small correction to projectile bremsstrahlung, a quantum electrodynamical correction due to bremsstrahlung of scattered electrons during electron-projectile collisions and a kinematic correction accounting for the finite mass of the nucleus in a collision. All these effects are important only for ultrarelativistic highly charged ions and can be fully neglected in the intermediate energy region addressed in the present study.

Finally, an important issue in the slowing down of a heavy ion beam in matter that was not discussed here is *energy loss straggling.* The energy loss straggling of a projectile ion in matter originates from the statistical nature of the collisions with target electrons, i. e. the fluctuation of the number of collisions and of the energy transfer in each collision. In addition to that, for partially ionized projectiles stochastic fluctuations of the ionic charge states due to electron capture and electron loss processes lead to a so-called charge-exchange straggling. In has been experimentally demonstrated [Wei00b] that the latter straggling mechanism dominates during the slowing down of heavy ions in the intermediate (100-1000 AMeV) energy range, giving a contribution of up to 7 times larger than the pure collisional straggling. Extended discussion about experimental as well as theoretical studies on the energy loss straggling of relativistic heavy ion beams in matter can be found in Refs. [Sch96d, Gei98, Wei00a, Wei00b, Wei02].

2.1.1.2 Projectile charge state

As it has been discussed previously, besides the stopping number, $\mathcal{L}$, the other problem in calculating the stopping power (Eq. (2.1)) is the charge state of the projectile, $\bar{Z}_p$. When the Sommerfeld parameter $\eta \gtrsim 1/2$, the projectile ions will also carry electrons with processes of capture and loss, so that $\bar{Z}_p < Z_p$. It is therefore important to know the value of $\bar{Z}_p$ and to include the projectile charge screening in calculations of the stopping of heavy ions in the intermediate and low energy regions.

An ion penetrating through matter with a certain initial charge state interacts with the target atoms and electrons. Several processes may occur: electron capture, ionization, excitation or decay. After the projectile ion travels a certain distance in the medium, a dynamical charge state equilibrium will be achieved. This is because the electron loss and capture are balanced on the average and the mean

charge state changes (decreases) only with the change in ion velocity due to energy loss of the projectile. To describe these processes, all the cross sections for the relevant electron configurations of the projectile are required. With these cross sections, the rate equations can be solved and hence the evolution of the charge state distribution is obtained.

However, it is very difficult to calculate all the required (energy-dependent) charge exchange cross sections. For example, electron capture can occur via three different mechanisms: radiative electron capture, non-radiative capture and resonant transfer and excitation [Wei00a]. These charge-changing processes have drastically different projectile, target and energy dependencies [Sch98a]. Although there are theoretical models and computer codes available to calculate the charge-exchange cross sections (such as ETACHA code [Roz96]) and to solve also the rate equations (CHARGE and GLOBAL codes [Sch98a]) for a limited number of electron configurations of a projectile, mostly semi-empirical formulas and parameterizations for $\bar{Z}_p$ are used in practice.

Following Northcliffe [Nor63, Nor70], a quantity called *effective charge*, Z_p^{eff} is usually defined in order to fit the experimental data on energy loss and range measurements for heavy ions. The effective charge is defined as a ratio of the stopping power of a medium for heavy ions to the stopping power for protons or, similar, for α-particles, at the same projectile velocity

$$Z_p^{\text{eff}} \overset{\text{def}}{=} \left[\frac{\mathcal{S}(Z_p, Z_t, v)}{\mathcal{S}_{\text{H}}(Z_t, v)} \right]^{1/2} . \tag{2.11}$$

The effective charge definition is useful since there is a large amount of experimental data on proton and helium stopping which is not affected by the charge-exchange effects.

There were many discussions on what one should use for $\bar{Z}_p$ in formula Eq. (2.1) [Ahl80]. Should one use the mean (rms) charge Z_p^{rms} (as e. g., measured with static electromagnetic fields), the effective charge Z_p^{eff} as defined by Eq. (2.11), or even can one assume that $Z_p^{\text{eff}} = Z_p^{\text{rms}}$? The last one seems to be the most natural first guess. However, there is a long-known "density effect", whereby charge states Z_p^{rms} as measured with solid are larger than those in equivalent gases. This demonstrates a difference between Z_p^{eff} and Z_p^{rms} for solid targets. It is not clear whether or not the discrepancy exists in the material itself or it is a transition effect, such as a prompt emission of Auger electrons upon departure of the ion from the solid [Bet70]. On the other hand, Z_p^{eff} does not depend significantly on whether stopping material is gas or solid and Z_p^{eff} is very close to Z_p^{rms} as measured with gas targets. These arguments were used by Bohr to assume that $Z_p^{\text{eff}} = Z_p^{\text{rms}}$ [Boh41]. Recently, Sigmund has noted [Sig01] that projectile and target atomic number dependencies of Z_p^{eff} differ distinctly from those of the Z_p^{rms} and that there is no theoretical basis for the effective-charge concept at all. Nonetheless, there are a number of semi-empirical formulas for $\bar{Z}_p$ that successfully describe the experimental data on heavy ion stopping and can be used in Eq. (2.1).

The empirical formula of Pierce and Blann [Pie68]

$$\bar{Z}_p = Z_p \left[1 - \exp\left(-\frac{0.95 \, v}{Z_p^{2/3} v_0} \right) \right] , \tag{2.12}$$

although does not depend on the target material, nevertheless can give a good approximation for heavy projectiles at least in the range between 100 and 1000

AMeV [Wei00a]. Note, that this formula is in fact a modified Tomas-Fermi relation, implying the Bohr's criterion that projectile electrons are stripped off if their orbital velocity ($v_{\mathrm{TF}} = Z_p^{2/3} v_0$) is smaller than the projectile velocity v.

Anthony and Landford have experimentally shown that $\bar{Z}_p$ depends on the target material [Ant82] and derived the empirical formula

$$\bar{Z}_p = Z_p \left[1 - A(Z_t) \exp \left(- \frac{B(Z_t)\, v}{Z_p^{2/3}\, v_0} \right) \right] , \qquad (2.13)$$

with the functions $A(Z_t)$ and $B(Z_t)$ given in [Ant82]. Both the above formulas will approach a constant value when $v \to c$, although the difference between $\bar{Z}_p$ and Z_p is below 0.1% even for large charges.

More recently, using a fit to a large dataset of energy loss and range data in the intermediate ($2.5 < E < 500\,\mathrm{AMeV}$) energy region, Hubert, Bimbot and Gauvin [Hub89, Hub90] have proposed the parametrization

$$\bar{Z}_p = Z_p \left[1 - X_1 \exp \left(-X_2 E^{X_3} Z_p^{-X_4} \right) \right] , \qquad (2.14)$$

where E is kinetic energy in AMeV and parameters $X_1(Z_p, Z_t)$, $X_2(Z_t)$, $X_3(Z_t)$ and $X_4(Z_t)$ are given in [Hub90] to describe all the available experimental data in a satisfactory manner.

In spite of its simplicity, Eq. (2.12) or its modifications are often used in stopping power and range calculations leading to a reasonable accuracy, especially in the intermediate energy region. An advantage of this formula is that it is a general description of the projectile charge based on Tomas-Fermi model and it does not depend on the effective charge formulation. If a better calculation precision for particular ion-target system is needed, more accurate empirical formulas, such as Eq. (2.14) can be used ensuring that $\bar{Z}_p$ agrees with the experimental results. Finally, for the intermediate energy region ($> 30\,\mathrm{AMeV}$), the charge state distributions can be calculated by solving the rate equations using the codes like CHARGE and GLOBAL.

2.1.1.3 Calculation of cold stopping

The stopping power of a cold medium for heavy ions in the intermediate ($30 < E < 500\,\mathrm{AMeV}$) energy region can be calculated by Eq. (2.1). As it has been discussed previously, for this energy region it is sufficient to use in this formula the expression for the stopping number

$$\mathcal{L} = \mathcal{L}_{\mathrm{Bethe}} + \delta \mathcal{L}_{\mathrm{LS}} \qquad (2.15)$$

and one of the empirical formulas for $\bar{Z}_p$, like Eq. (2.12), Eq. (2.13) or Eq. (2.14). In the high energy region ($> \mathrm{AGeV}$), $\delta \mathcal{L}_{\mathrm{FNS}}$ and $\delta \mathcal{L}_{\mathrm{dens}}$ corrections to the stopping number, the projectile radiation and other ultrarelativistic effects have to be included. On the other hand, for low projectile velocities (below and around the stopping maximum) and heavy target material, the effects described by $\delta \mathcal{L}_{\mathrm{Barkas}}$ and $\delta \mathcal{L}_{\mathrm{shell}}$ corrections become important. There are a number of other theories, corrections and empirical formulations for the low energy region that are not described here.

For practical calculations of the cold stopping for heavy ions one of the available computer codes can be used. Some of the widely used codes and models are briefly described below:

SRIM The SRIM code [Zie96] by Ziegler et al. is probably the most universal and well-established code for stopping and range calculations that is used worldwide. Ziegler's stopping model [Zie96] is similar to that described above in this section for the intermediate energy region, although a number of advanced models for low (AkeV) energy region are employed in the code to provide a good accuracy for low ion velocities. This makes using the SRIM popular especially in applied sciences and industry where precise knowledge about the ions ranges and details of the stopping near the Bragg peak are important. Moreover, the SRIM model contains a set of empirical coefficients whose values are continuously modified in order to fit all the reliable experimental data on stopping and ranges that is available up to date. At the moment, more than 2000 different experimental papers are collected by the authors and used to adjust the SRIM model. In addition, a Monte-Carlo code by the same authors, called TRIM is able to calculate most of the details in the slowing down of low-energy ions. SRIM and TRIM are freely available in the Internet except for the source codes.

ATIMA The ATIMA code [ATI] is developed at GSI-Darmstadt to benchmark different stopping and charge-exchange theories against a large set of experimental data on slowing down of relativistic heavy ions, obtained mostly at the fragment separator installation (FRS) at the GSI [Sch01b]. This code is widely used at the GSI for preparation and calibration of nuclear physics experiments performed at the FRS. In the low-energy region the code is based on the Ziegler model, whereas Lindhard and Søresen (LS) theory is used for the high energy region. A formula, similar to Eq. (2.12) is included to approximate the mean charge state of the projectiles during slowing down. In addition to that, the code contains procedures from the CHARGE code [Sch98a], allowing to calculate the evolution of charge state distribution for bare (up to three electrons) heavy ions. The stopping power and ranges of heavy ions in the intermediate energy region calculated by ATIMA are in good agreement with SRIM calculations, except for the low energies around 10–30 AMeV, which is simply an interpolation region between low- and high-energy stopping models in the ATIMA code.

Berkeley CRANGE The stopping code called CRANGE has been recently developed by Weaver and co-workers [Wea02] at the University of California, Berkeley, and is freely available including the complete source codes. Originally, the code has been developed for applications in cosmic-ray astrophysics but can be used for other purposes as well. The theoretical model of the code is as described above in this section. The code allows to include/exclude independently various corrections to the stopping number and can be easily adopted for particular problem, since the sources written in C language are available. Therefore, the CRANGE code is a useful tool to study different aspects of slowing down of heavy ions in matter.

CasP In the CasP (*"convolution approximation for swift particles"*) code [Sch99] "unitary convolution approximation", developed by Grande and Schiwietz is used. They proposed a simple way to calculate the impact-parameter dependence of energy loss of bare ions. This perturbative convolution approximation is based on first order perturbation theory, which is only valid for fast projectiles with

low charges. But using Bloch stopping power result and a simple scaling, they could overcome the restriction to low charge states. It is also possible with the code to treat non-equilibrium energy loss phenomena. However, the code needs further development to become a useful tool for practical calculations of heavy ion stopping in the intermediate energy region. The CasP code is freeware and is available in the Internet.

CKLT model Maynard et al. [May01b, May01a] expressed the stopping power of swift heavy ions within the convergent kinetic Lindhard theory, based on a modified Bloch correction term, devoted to correctly describe the close collision contribution to the energy loss process. An advantage of this theory is that a single formula can express the stopping power both in cold and plasma targets. The model also introduces high-order correction terms due to non-Coulomb interaction potential of the projectiles, screened by its bound electrons. The CKLT model is an alternative description of the stopping of swift heavy ions in the intermediate and moderately low energy regions. There are several papers (e. g., [Bla02]) showing an agreement between experimental results on stopping power measured in the non-equilibrium charge state regime and this theory.

MSTAR The MSTAR code [Pau01] is based on the stopping power data for α-particles contained in ICRU-49 NIST report [ICR93]. Using practically the effective charge concept, the authors have analyzed a large amount of experimental data on stopping of heavy ions and have derived a three-parameter empirical approximation for the stopping power relative to the well-investigated α-particle stopping. The empirical formula is applied for the stopping powers of all elements except for hydrogen to ions from **Li** to **Ar** and reproduces the experimental data in the intermediate energy region with sufficient accuracy. The program is freely available together with related programs ESTAR, PSTAR and ASTAR that contain NIST data tables for stopping of electrons, protons and α-particles, respectively.

RANGE In the RANGE code [Zhu00] the linear Boltzmann transport equation is solved using a special iteration technique. It is therefore possible to obtain realistic values of the first four moments over a spatial range distribution in a wide energy region. The stopping model of the code is based on the Ziegler's approach [Zie96] and the code allows for independent inclusion or exclusion of a number of corrections to the stopping number, such as the Lindhard and Søresen corrections and Mott correction. The results of the calculations of the total ranges of heavy ions (from **Ar** to **U**) with initial energies about 1 AGeV in nuclear photoemulsion, performed using this code, have demonstrated good agreement with recent experiments [Bog99, Zhu00]. It was shown that higher-order with respect to Z_p corrections ($\delta\mathcal{L}_{\text{LS}}$ or $\delta\mathcal{L}_{\text{Mott}}$) have to be included in the calculations in order to explain measured ion ranges at these energies.

The results the stopping power calculations using modern computer codes (like SRIM, ATIMA and others) even for the heaviest ions such as uranium, in the intermediate energy region from about 30 AMeV to 500 AMeV are in good agreement with each other and with available experimental data, especially for such popular and well-studied target materials as plastic scintillators and emulsions. However, it is to be noted that this is not the case for other energy regions, such as at low

projectile velocities (below stopping maximum) as well as at the ultrarelativistic velocities, as it was discussed above.

It is to be concluded that the deviations in the stopping power and ranges among different calculations and experiments *in this energy region* is usually not more than $\pm 2\%$ [Sch01b]. In the present work the SRIM code is used for calculations of the stopping power and range-energy relation. The stopping power of organic scintillators to the heavy ions and their ranges in the energy region of about 40–300 AMeV was of the most importance for the this study (see sec. 4.2).

2.1.2 Plasma effects

Stopping power of plasma is quite different compared to the cold matter. For example, an enhanced stopping power of a plasma which can be up to a factor of 40 higher than in the respective cold material has been measured [Jac95]. The main physical effects responsible for this fact are described below.

Free electron contribution. In a plasma, free electrons contribute to the slowing down of a projectile ion. An additional term therefore must be added to the stopping logarithm to describe interactions with free electrons. Qualitatively, in such a term the mean ionization potential of target atoms, I which is used to describe the contribution from bound electrons, is replaced by the free electron plasma frequency, $\hbar\omega_{\text{free}}$, $\omega_{\text{free}}^2 = e^2 n_e^{\text{free}}/\epsilon_0 m_e$. The projectile energy is more efficiently transfered to free plasma electrons than to the bound electrons of the cold material. Hence the stopping power of the plasma is increased. At equilibrium conditions, the velocity distribution function of free electrons is Maxwellian and the relative quantity with which the projectile velocity should be compared is the electron thermal velocity, $v_{\text{th}} = \sqrt{k_{\text{B}}T/m_e}$, instead of the orbital velocity of bound electrons, v_{TF} in cold matter. Thus, the applicability criteria of various theoretical approaches to describe stopping in plasmas are also different.

Projectile charge state. The charge states of heavy ions in an ionized stopping material can be considerably higher than those while slowing down of an ion beam in an equivalent cold matter. This is due to reduced electron recombination, especially in a fully ionized plasma. This also leads to an increased stopping power of a plasma compared to the cold matter. Moreover, highly non-equilibrium projectile charge states can be found in strongly ionized targets due to lowered electron capture rates and faster stopping.

Modified stopping power due to bound electrons. In a partially ionized target material, the stopping power due to bound electrons of target ions differs from that of bound electrons in cold matter. The mean ionization energy of a target ion in a plasma is larger and therefore the contribution to the stopping power by these bound electrons is reduced compared to that for neutral atoms in a cold target. In a partially ionized plasma, the contributions to the stopping power by differently charged target ions also have to be calculated separately, taking into account the differences in electron configurations.

Strong inter-particle interactions. In dense plasmas, the potential energy of charged particles due to their mutual Coulomb interactions ($Z_t^2 e^2/4\pi\epsilon_0 d$) can be

equal to, or even larger than the thermal energy ($k_{\mathrm{B}}T$). Thus the plasma starts to exhibit long- and short-range order due to the correlating effects of the atoms/ions. The target atoms and electrons are no longer well described by their isolated behavior. Such a plasma is called *nonideal* or *strongly coupled* plasma. A quantity expressing the non-ideality of a plasma, Γ, called *nonideality* or *coupling parameter*, can be defined by the expression

$$\Gamma = \frac{Z_t^2 e^2}{4\pi\epsilon_0 d}/k_{\mathrm{B}}T, \qquad (2.16)$$

where $d = (3Z_p/4\pi n_e)^{1/3}$ is the inter-particle spacing. The isoline $\Gamma = 1$ separates ideal and nonideal regimes.

All the above mentioned physical effects that modify the stopping power of ionized matter have to be revised in case of the presence of strong inter-particle interactions in a plasma. One can therefore expect a nonlinear behavior of stopping with respect to the target density and temperature. In general, the stopping power of a strongly coupled plasma is lower than that of ideal plasmas at the same density.

In addition to that, in dense nonideal plasmas, when the inter-particle interaction energy becomes of the same order as the ionization and dissociation energies of the target ions and atoms ($n_e^{\mathrm{tot}} \gtrsim 10^{23}\,cm^{-3}$), the effective binding energies vanish, the bound states break up. One thus observes the transition from a partially ionized to a fully ionized plasma due to pressure ionization. This effect is called *Mott plasma phase transition* [Kra86]. The Mott plasma transition also affects the density dependence of the heavy ion stopping in nonideal plasmas, introducing a sharp increase in stopping power at a certain threshold plasma density [Ger02].

During the past decade, many experiments on interaction between ion beams and externally generated plasmas have been performed using mainly gas discharges [Hof88, Hof90, Die92, Hof94, Jac95, Gol01] and laser-ablated plasmas [Cou94, Stö96, Wet97, Rot00], reaching the electron densities $n_e \sim 10^{19} - 10^{21}\,cm^{-3}$ and target temperatures up to 60 eV. The effect of a drastically enhanced stopping power for plasmas has been experimentally confirmed. However, there is a lack of experimental data on this problem, especially for the stopping power of dense nonideal plasmas.

Much theoretical work has also been done in recent years to model the interaction between beam ions and plasma particles in ideal as well as in nonideal plasmas. For ideal plasmas, most of the approaches result in a modified Bethe formula that is generalized for multiply charged plasma ions (see, e. g., [Nar78, Meh81, Bas84, Pet91]). For fast ion beams and weakly coupled plasmas, this formula is in good agreement with experimental data [Stö96, Wet97, Gol98], however, deviations arise for higher particle densities [Rot00]. Later, theoretical studies based on density functional theory [Zar95], Vlasov-Poisson equations [D'A92, BF96], Boltzmann kinetic equations beyond the Born approximation [Bor96, Sch98b, Ger99, Ger02] and computer simulations [Zwi99] have been carried out. In these investigations, special attention was given to strong beam ion-plasma electron correlations and bound electron contribution in nonideal plasmas. The results of these theories are still to be tested experimentally.

2.2   Heating by intense heavy ion beams

In the previous section the physical processes occurring during the slowing down of heavy ion beams in cold or ionized targets have been discussed. It was shown that when heavy ions penetrate through matter, they lose their energy mainly due to the interactions with target electrons and the charge state of the projectiles changes as well. In all the previous discussions it was implicitly assumed that there is no influence of the incident beam on the target.

However, the energy that the beam ions lose resides in the target. In case of an intense beam and especially, an intense beam focused to a small (a millimeter) spot in a target, the amount of energy deposited by the beam in the target volume can modify matter properties of the irradiated samples significantly. Macroscopic amounts of the target material can be heated to high $(10^3-10^5\,K)$ temperatures leading to a *high energy density* (HED) state. Matter in this state can have solid and super-solid densities and pressures in the range of megabars. The characteristic target properties therefore change dramatically: thermophysical and hydrodynamical effects such as phase transitions, penetration of shock and compression waves become important. Matter under such extreme conditions is of special interest to many branches of pure and applied sciences including astrophysics, planetary sciences, inertial fusion energy research and physics of dense nonideal plasmas.

A relevant quantity to characterize the heating of matter by an intense heavy ion beam is the *specific deposited energy, $\mathcal{E}$*. This quantity gives the amount of energy deposited by the beam per unit mass of the target material, i. e. expresses the capability of a heavy ion beam to heat the matter. The specific deposited energy can be estimated using the following formula

$$\mathcal{E} = \frac{N}{\pi r_b^2}\frac{\mathcal{S}(E)}{\rho}\,, \qquad [\mathcal{E}] = \mathrm{kJ/g}, \tag{2.17}$$

where N is the number of ions in the beam, r_b is the beam spot radius and $\mathcal{S}(E)$ is the stopping power of the material with density ρ to the ions of energy E. This formula gives exact value of the specific energy deposition only for the case of instantaneous heating and a uniform transverse intensity distribution of the beam. In other cases $\mathcal{E} = \mathcal{E}(\mathbf{x}, t)$ and Eq. (2.17) should be used only for rough estimations.

Since the stopping power is roughly proportional to the target (electron) density, $\mathcal{S} \propto \rho$, the specific deposited energy depends only weakly on the target density and $\mathcal{E} \propto N$, $\mathcal{E} \propto 1/r_b^2$. Therefore, $\mathcal{E}$ predominantly expresses the property of the beam but not that of the target. On the other hand, $\mathcal{E}$ is just the value of the internal (thermal) energy of the target material induced by the beam heating. Together with density, ρ the internal energy defines the thermodynamical state of matter. The values of other thermodynamic quantities, such as temperature and pressure can be obtained if the *equation of state* (EOS) properties of the target material are known (see sec. 5.2). For example, if a specific energy of 1 kJ/g is deposited in a target at solid density, temperatures of about 0.6 eV, 1.17 eV and 0.1 eV are induced in lead, aluminum and neon targets, respectively (see Tab. 5.2, p. 79).

2.2.1   Experimental research

Experimental activities on HED matter induced by heavy ion beams have been exclusively concentrated at Gesellschaft für Schwerionenforschung (GSI), Darmstadt

due to its unique accelerator facilities. The first experiments on volume target heating started already at the end of 1980s using the MAXILAC-RFQ accelerator at the GSI. In these experiments [Jac89, Jac90] hydrodynamic response of a xenon gas target irradiated by a $\mathbf{Kr}^+$, 45 AkeV long-pulse ($\sim$ ms) beam focused to a $1\,mm^2$ spot was observed for the first time. The low-density (pressure of about 0.6 bar) gas target was heated to a 0.75 eV temperature while the estimated maximum specific energy deposition was about 1.5 kJ/g.

After the commissioning of the heavy ion synchrotron SIS-18 in 1990 and setting into operation the "High Temperature" (HHT) experimental area in 1991 (see sec. 3.1), highly energetic (hundreds of AMeV) ion beams became available for plasma physics experiments, allowing to study heavy-ion beam generated plasmas in solid materials. Since that time the intensity of the energetic heavy ion beams has been steadily increasing. In 1994, a $\mathbf{Ne}^{10+}$, 300 AMeV beam of $2 \cdot 10^{10}$ particles that was delivered in a pulse of about $1\,\mu s$, allowed to make experiments on the heavy-ion-beam induced hydrodynamic motion in rare-gas solids [Dor96]. However, the maximum specific energy deposited in these experiments was $\mathcal{E} \approx 0.06\,kJ/g$. With this amount of energy it was hardly possible to overcome the binding energy of the target material.

The energy density induced in the target by an ion beam is inversely proportional to the square of the beam radius (Eq. (2.17)). Therefore the availability of an appropriate focusing system is crucial for the experiments. Since 1994 a special final focusing system, the plasma lens [Ste93], was being developed for high-energy-density experiments. Using the plasma lens, intense heavy ion beams can be focused to a spot of $400\,\mu m$ (FWHM) at the target position, thereby increasing the deposited specific energy by a factor of four compared to a standard quadrupole focusing system [Ste96]. Further development of the plasma lens performance allowed to realize also complicated beam configurations at the target, such as shaping a beam to a hollow cylindrical form [Neu00]. This can give significant advantages while compressing matter in cylindrical implosion geometries, for example, to study metallization of hydrogen with heavy ion beams [Tah98, Tah00a, Tah01a].

Within the next two years, in 1996 a high intensity (about $2 \cdot 10^{10}$) was reached already with $^{40}\mathbf{Ar}^{18+}$ projectiles and the plasma lens has been set into operation, meeting altogether the requirements for hydrodynamic phenomena in metal targets [Fun98, Stö98]. Thus, a specific energy deposition of about 1 kJ/g has been achieved in the Bragg-peak region, irradiating initially solid lead targets.

In order to achieve the highest energy density in matter, all the beam energy must be deposited before the target material expands significantly. Recently, employing a new extraction mode, the pulse length has been reduced from $1\,\mu s$ to $250\,ns$ [Fun98, Stö98]. This has allowed to explore new regimes of hydrodynamic response at high pressures and shock waves induced in the target material.

The backbone of any experiment is the diagnostics. For this reason the study of heavy-ion beam induced HED matter at GSI was concentrated on the development of novel beam and target diagnostic techniques as well as on improvement of existing ones. Here a selected number of diagnostic methods which have been developed and employed in experiments during the past years is mentioned.

Hydrodynamic motion of the heavy-ion-beam heated target material has been observed by shadowgraphy with various high-speed multi-framing and streak cameras [Dor96, Fun98, Stö98, Dew01]. The penetration of weak multiple shock and compression waves in transparent targets has been registered using schlieren

and interferometric techniques [Con01, Con02]. Direct, time-resolved pressure measurements have been performed using polyvinildenftoride (PVDF) piezo-electric pressure gauges embedded in the targets [Fun99a, Fun99b, Hof00, Stö98]. Modification of the electrical conductivity of metallic targets under heavy-ion beam irradiation has also been studied [Udr01, Udr02].

First experimental studies on light emission in visible and VUV spectral ranges from rare-gas solid as well as gaseous targets excited by heavy ion beams have also been done [Wie88, Krö91, Jac95, Dor96, Sal98, Con02]. Besides the interests for atomic physics, such spectroscopic measurements will allow a precise determination of the temperature induced in the target [Wie00].

2.2.2 Theoretical activities

The main theoretical activities in this field during the past years have been the development of computer simulation models to design and interpret beam-matter interaction experiments at GSI.

A sophisticated two-dimensional hydrodynamic computer code, BIG-2 [Vor97, For96] has been exclusively modified to include various relevant physical processes. For example, a heavy ion beam energy deposition package, taking into account the beam geometry has been developed and incorporated into the code and an electron thermal conductivity model has been coupled to the hydrodynamics. The code has also been extended to allow calculations using various options for the EOS of different target materials. The extended version of the code can now handle complicated and realistic beam-target configurations.

Using the above code, extensive calculations have been carried out to simulate recent experiments [Fun98, Fun99a, Hof00, Neu01, Var01, Con02, Var02b]. Reasonably good agreement has been found between the experimental data and the calculations [Var01, Var02b]. These calculations have been very useful in understanding the experimental results.

In addition to that, the problems of theoretical importance in the heavy-ion beam induced HED matter have been studied (see, e. g., [Tah99, Tah00b, Tah01b]). The information provided by these studies has been very helpful in proposing a number of novel experiments for future accelerator facilities at the GSI. One such proposed experiment is an investigation of the hydrogen metallization problem [Tah98, Tah00a, Tah01a]. Another important subject that has been thoroughly analyzed is to find possibilities for experimental studies of the EOS properties of high-energy-density matter [Tah00a, Hof02].

A correct EOS model for the target material is crucial for the accuracy and validity of the simulation results (see sec. 5.2.2). It is well known that the most widely used EOS data tables from Los Alamos laboratory (SESAME) [Ker83] have a limited accuracy in certain regions of pressure, density and temperature parameter space, especially in the low temperature and high density regime. This regime is of particular relevance to heavy ion beam matter interaction experiments discussed in this thesis. Over the past few years more advanced EOS models for the simulations have been developed [Bus93, For97, Gry98, For98, Khi98, Gry99, For01].

2.3 Needs and challenges for energy loss dynamics measurements

In the previous section it was shown that an intense focused heavy ion beam, while interacting with a target can significantly modify the properties of the target matter. Heating of the target by an ion beam leads to a fast hydrodynamic and thermodynamic response of the target material, such as launching of intense shock and compression waves and phase transitions. The spatial distribution of the target density is changing during and after the irradiation and the energy loss of the ion beam will change accordingly. Therefore, measuring the energy loss of the beam emerging from the back surface of the target during the irradiation would provide important information about the physical state of the interior of the target, which cannot be obtained by other means [Var98b]. This diagnostics method, where the energy loss of the beam heating a target is measured with time resolution is called *energy loss dynamics* or *ELD* measurements.

The first question that one would ask is if the hydrodynamic processes induced by an ion beam are fast enough that already during the short time of irradiation[4] the changes in target density can lead to a measurable modification of the ion beam energy loss. In order to answer this question, preliminary two-dimensional hydrodynamic simulations of the interaction phenomena have been performed [Var98b, Var98a, Var98c], using various target geometries and different parameters of the beam. These simulations have shown that even with the presently available ion beams, one can expect the energy loss of the beam ions changing from 100%, when the beam is initally stopped in a solid target down to a few percent, when the heated target material expands, within the interaction time. Moreover, by using special target geometries such as a target that has a low density region or a hole around the axis, one can expect non-monotonic behavior of the energy loss time dependence due to cylindrical implosion/expansion processes. Therefore, ELD measurements would provide important information about the hydrodynamic phenomena in heavy ion beam induced HED matter. However, to perform the ELD measurements one needs a special instrument, namely, a spectrometer with energy and time resolution. As discussed below, development of such an instrument is a challenging task.

2.3.1 Special requirements for a magnetic spectrometer

When it is needed to resolve energies of a highly energetic beam of charged particles, the first idea is usually to design a magnetic spectrometer. The trajectories of charged particles in a uniform magnetic field are separated by the momentum of a particle or, more precisely, by its *magnetic rigidity,*

$$\chi_m = \frac{mv}{Ze} = B \cdot \rho \approx 0.144 \frac{M}{Z} \sqrt{E \left(1 + \frac{E}{1863} \right)}, \tag{2.18}$$

where $p = mv$ is the momentum of the particle, Ze is its charge, ρ is the radius of the particle trajectory in a uniform magnetic field B, and E is the kinetic energy of the particle; $[\chi_m] = \mathrm{Tm}$, $[E] = \mathrm{AMeV}$ and $[M] = \mathrm{m.\,u.}$ If the mass of the particle M is known then the energy and charge state can be resolved using an analyzing magnetic field. Note, that in order to resolve the heavy ion energies of several

---

[4]Ion beam pulse duration is about several hundreds of nanoseconds, see sec. 3.1

hundred AMeV (magnetic rigidities of about 1–10 Tm) strong magnetic fields about several Tesla are required, whereas use of an electrostatic field in this energy range is absolutely inefficient.

The requirements for a magnetic spectrometer which is needed for the ELD measurements are very special and unusual compared to most of the "traditional" magnetic spectrometers. Below the main distinctive features of such an instrument are discussed.

- **Huge dynamic range.** All the heavy-ion beam induced HED matter experiments are the "single-shot" experiments, where the initial conditions cannot always be reproduced exactly and the repetition rate is low because the target is being destroyed after each shot. Therefore, it is important to collect as much data as possible during one shot. On the other hand, as it has been mentioned above, one can expect the energy of the ions escaping the target to be changing from zero to almost full initial energy (several hundreds AMeV) within the interaction time. This implies that the *dynamic range* or *energy acceptance* of the ELD spectrometer must be very large, not less than at least 60–70%. The dynamic ranges of the traditional high resolution spectrometers, on the other hand are usually about a few percent. The requirement of a large dynamic range makes it very difficult to achieve high resolving power. Futhermore, one should use focusing elements (quadrupole magnetic lenses) in the spectrometer design with great care, because the large energy acceptance enforces the contribution from chromatic aberrations of these elements significantly. Note that due to the above arguments it is not possible to collect the data in "event counting" mode, as it is used in nuclear and particle physics experiments.

- **High energy of the ions.** For ELD measurements one has to analyze the ions with energies of about tens and hundreds AMeV, i. e. with the magnetic rigidities of the ions of up to 10 Tm. Thus, a large "$B \cdot \rho$", "(magnetic field) $\times$ (field volume)" product is needed in order to achieve sufficient resolving power. In fact, an analyzing magnetic field with flux density of the order of several Tesla has to be realized in the spectrometer.

- **Time resolution** $\Delta \tau \sim 5 - 50 \, \text{ns}$ **is needed.** In contrast to most spectrometers, for ELD measurements one has to detect *time-resolved* energy spectra of the ions escaping from a target. The lower limit for the required time resolution is defined by the relaxation time of the target electrons excited by interactions with a beam ion, i. e., the time which is needed for the conversion of energy lost by the beam into thermal energy of the target matter, which is being later transfered to kinetic energy of the hydrodynamic motion. The electronic relaxation times can be up to several nanoseconds. The upper limit for $\Delta \tau$ is given by the ion pulse duration ($\lesssim 1 \, \mu s$) and characteristic times of the hydrodynamic processes that also depend on the beam and target parameters. Typically, a time resolution of $\Delta \tau \sim 10 - 30 \, \text{ns}$ is sufficient for the present experiments. Fortunately, this requirement can be fulfilled by using an appropriate detector, such as a combination of fast scintillating material and fast electronic streak-camera.

- **Spatial extension of the setup is limited.** The space available at the HHT experimental area (sec. 3.1.2) for the spectrometer setup is limited. One can-

not therefore use large dipole magnets and/or long vacuum drift distances. The spectrometer which is to be installed behind the target chamber should not be more than one to two meters in length. Indeed, one cannot build at the HHT area a large spectrometer, consisting of a number of bulky dipole and quadrupole magnets such as for example, the FRS magnetic spectrometer at the GSI. The constraint on the spectrometer dimensions is in contradiction to the above requirement of a large magnetic field volume and it therefore limits the resolving power.

- **Energy resolution $\mathfrak{r}_E \lesssim 1\,\%$ is required.** For most of the HED matter experiments, energy resolution $\mathfrak{r}_E$ of the ELD measurements below or about one percent (the resolving power $\mathfrak{R}_E = 1/\mathfrak{r}_E \geqslant 10^2$) would be sufficient. At first, this is due to a relatively large energy spread of the incident ion beam which can be up to one percent while using a compressed ion bunch (see sec. 3.1.1). Secondly, the energy of the ions escaping a target is gradualy changing during the irradiation time. Although at every time moment the energy spectrum of the escaping ions can be rather narrow, the change in the mean ion energy during the time $_\Delta\tau \approx 10 - 20\,\mathrm{ns}$ can also be about one or two percent. Therefore, taking into account the time resolution of the measurements, an energy resolution of about 1 % should be satisfactory. This is to be compared with traditional high resolution magnetic spectrometers, with typical resolving powers of about $10^4 - 10^6$. However, given the above described requirements and especially the very large dynamic range, it is difficult to achieve even this moderate (about a few percent) resolution in an ELD spectrometer.

- **Spatial acceptance can be relatively small.** In contrast to most of the other spectrometers, a large acceptance[5] is not needed for the ELD measurements. The results of the ELD measurements can be much easier understood and interpreted when the ELD dependence is recorded only "on axis", i. e. for the ions penetrating through a target in a small vicinity of the beam axis. A collimator installed before the spectrometer should select a small axial part of the ions escaping a target. Therefore, an acceptance $_\Delta x \cdot {}_\Delta\alpha \leqslant 0.5\,\mathrm{mm} \cdot \mathrm{mrad}$ is required. Here $_\Delta x$ and $_\Delta\alpha$ are spatial and angular spread of the beam entering a spectrometer through the collimator, respectively.

The achievable resolving power should benefit from the fact that only a small acceptance is required. The resolving power as defined in first order (neglecting higher-order aberrations) is given by the following expression [Wol87]:

$$\mathfrak{R}_E = \frac{\mathfrak{D}_E}{\mathcal{M} \cdot {}_\Delta x + \mathcal{A} \cdot {}_\Delta\alpha}\,, \tag{2.19}$$

where $\mathfrak{D}_E = \dfrac{\partial x_{\mathrm{detector}}}{\partial \delta_E}$, $E = E_0(1 + \delta_E)$ is the energy dispersion of the spectrometer whereas $\mathcal{M} = \dfrac{\partial x_{\mathrm{detector}}}{\partial x_{\mathrm{collimator}}}$ and $\mathcal{A} = \dfrac{\partial x_{\mathrm{detector}}}{\partial \alpha_{\mathrm{collimator}}}$ are the spatial and angular magnification factors, respectively. Therefore the resolving power is inversely proportional to the acceptance, $_\Delta x \cdot {}_\Delta\alpha$. On the other hand, a small acceptance or a small number of particles that enter the spectrometer put an additional demand on the sensitivity of the detector, especially taking into account that the time resolution is required as well.

---

[5]Transverse phase space volume occupied by the particles that can be analyzed by a spectrometer.

- **Pulsed operation is possible.** Since the ELD measurements should be performed in single-shot experiments, the analyzing magnetic field must exist only for times longer compared to the ion beam pulse duration, which is $\sim 1\,\mu s$. The use of DC iron-dominated or superconducting magnets is not obligatory. Therefore pulsed devices can be employed in the construction of the ELD magnetic spectrometer.

2.3.2 Pulsed high current magnetic lenses

Recent developments on a new generation of fast pulsed high-current magnetic lenses [Spi93, Win94, Win96, Var98b, Var98a, Leh98, Var99, Var00b, Li00, Var02a] have demonstrated that these devices can be an attractive alternative to conventional steel-dominated or superconducting magnets. Since the magnetic flux density in such magnets is not limited by the saturation of ferromagnetic material, high flux densities (several Tesla) and high field gradients (10^2–10^3 T/m) can be achieved. In contrast to superconducting coils, the construction of pulsed high-current magnetic lenses is very compact and inexpensive.

Therefore, it has been proposed to use pulsed high-current lenses in the construction of an ELD magnetic spectrometer [Var98b, Var98a]. Besides the ELD spectrometer, the other proposed applications for these magnets are, for example, a final focusing system for high rigidity heavy ion beams [Spi93, Win94, Win96], a short focal length condenser system for projectile fragment separator (FRS) at GSI [Li00] and fast correction elements for polarized proton beam acceleration at COSY synchrotron (Jülich) [Leh98].

2.3.2.1 Operating principle, different constructions and experiments

A spatial distribution of the magnetic flux density which is quite similar to the ideal multipole fields can be generated by an adequate arrangement of conductors. The operating principle of a pulsed quadrupole magnet is shown in Fig. 2.2. The magnitude of the field is proportional to the current in the conductor system and is not limited by saturation effects. The conductor geometry and the magnetic field distribution of such a lens are similar to a superconducting magnet without an iron yoke. Due to the pulsed operation mode, low resistance and inductance, no significant heating or damage of the conductors occurs even when a high voltage (peak currents up to 50 kA) is applied to the system.

The quality and the magnitude of the magnetic field in a pulsed lens can be optimized using an appropriate strip-line conductor system. For example, a lens can be constructed using thin copper foils insulated by mylar or kapton, wrapped around a plastic or ceramic beam-guide pipe [Var98a, Var99]. The conductor arrangement can be etched in the copper like a printed circuit (see, e. g., Figs. 2.3(a) and 2.5(left)).

The resolving power of a magnetic spectrometer depends on the maximum value of the magnetic field realized in the magnets. Therefore, it is important to study the possibility to enhance the magnetic field in pulsed lenses with equal field volume and equal power of the pulse generators. The magnetic field in a multi-layer foil is proportional to the number of layers if the same electrical current flows in the strip-lines. However, the inductance and the resistance of a conductor arrangement grow with the number of layers. Thus the peak current in the "pulse generator — strip-line lens" RCL-circuit drops. Hence, to predict the behavior of the magnetic field
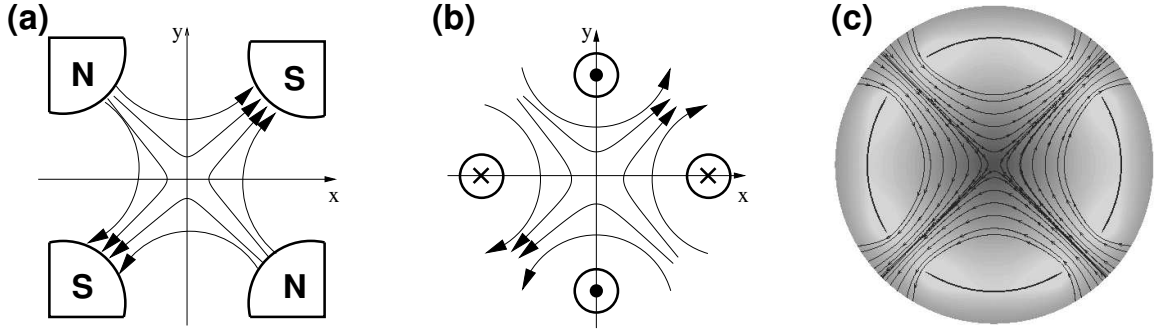
Figure 2.2: Operating principle of pulsed high-current magnetic lenses. (a) — a schematic view of an ideal quadrupole; (b) — a pulsed quadrupole set up by four wires with a current in axial direction; (c) — pulsed strip-line quadrupole (magnetic field distribution calculated by the VARDIOS code).

strength in multi-layer lenses it is important to know the inductance of a multi-layer foil which is difficult to calculate precisely.
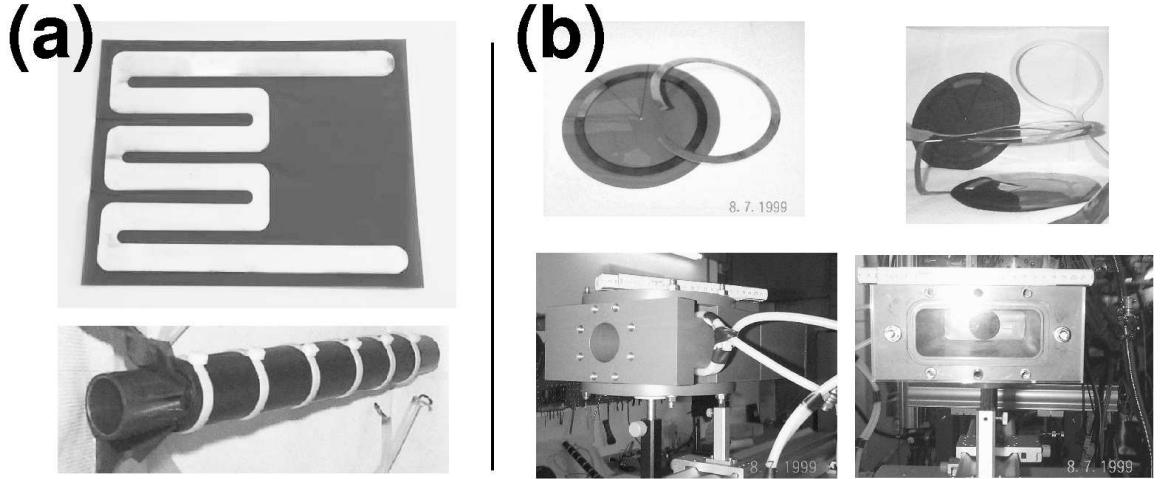

Figure 2.3: Pulsed high-current magnetic dipole lenses used in experiments. **(a)**: three-layer pulsed cylindrical "$\cos 2\theta$" dipole; aperture: 40 mm, length: 250 mm. **(b)**: "Helmholtz-coils" pulsed dipole; effective gap width: 50 mm, length: 140 mm. See also Tab. 2.1 for the relevant parameters of these lenses.

In order to investigate the dependence of the magnetic field on the number of layers, numerous experiments with multi-layer pulsed cylindrical dipole lenses (see Fig. 2.3(a)) have been performed in which the magnetic field inside the lens has been measured using a small inductive probe [Var98a]. The performed experiments proved that employment of multi-layer arrangements can amplify the magnetic field and, moreover, can suppress the higher-order parasitic multipole components [Var99]. For example, for the cylindrical pulsed strip-line dipole the enhancement in magnetic flux density is about a factor of 2.1 for the three-layer foil (Fig. 2.3(a)) and is expected to be about factor of 2.5 for a five-layer foil. Since for pulsed quadrupoles the pole value of the field is two times higher for the same number of layers, a five-layer pulsed quadrupole lens with an effective field length of 25 cm will provide a peak magnetic field of about 4 T with the field gradient of about 200 T/m at a rather moderate energy stored in the pulsed power generator which is presently available at the HHT.
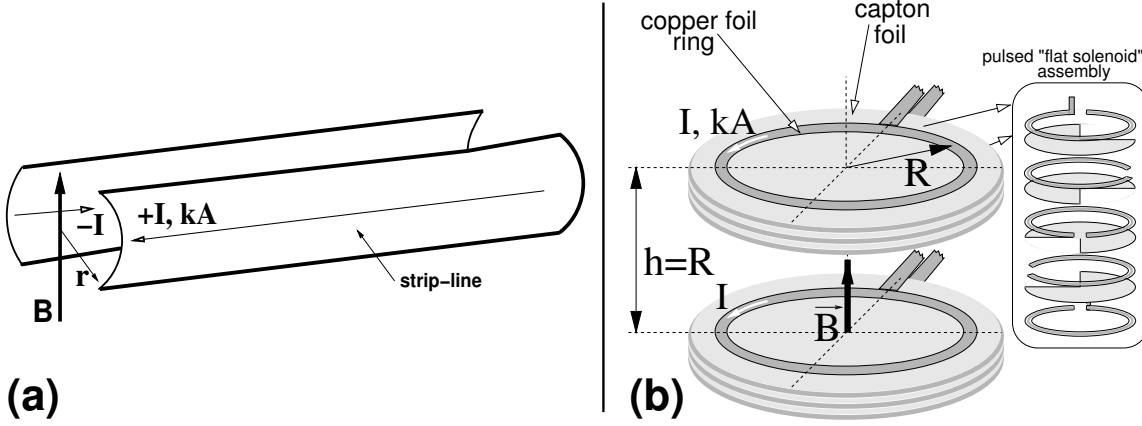
Figure 2.4: Principal scheme of pulsed high-current dipole magnets. **(a)**: pulsed strip-line "$\cos 2\theta$" dipole, **(b)**: "Helmholtz-coils" pulsed dipole.

Besides the studies on cylindrical "$\cos 2\theta$" strip-line pulsed magnets, recently a new type of a high current pulsed iron-free dipole magnet in a "Helmholtz-coils" configuration has been developed [Var00b] (see Fig. 2.4). Compared to the strip-line dipoles, this new pulsed dipole type has a number of advantages. For example, no conductors are located in the plane of deflection and thus the maximum deflection angle is not limited. The volume of uniform magnetic field is enhanced and the support and alignment are less complicated.

The field strength in the "Helmholtz-coils" pulsed dipole can also be increased by means of a multilayer conductor arrangement, implementing a special ring stacking technique. A number of copper-foil rings with kapton-foil insulation disks in between are placed on top of each other. Both, the copper rings and the kapton disks have sector cuts. The rings and disks are arranged around the axis in such a way, that the stack becomes comparable to a flat (thin) multi-turn solenoid (Figs. 2.4, 2.3(b)). By this stacking technique "Helmholtz-coils" dipoles can be easily set up with arbitrary number of layers using the same support. To improve the field quality the location and geometry of the coils can also be optimized.

Table 2.1: High-current pulsed dipole magnetic lenses.

	"$\cos 2\theta$" *strip-line dipole*	*"Helmholtz-coils" dipole*
Magnetic field, T	0.3 – 1.6	0.2 – 1
Field volume, cm^3	150	400
Eff. field length, mm	250	140
Eff. gap width, mm	27	50
Peak current, kA	8 – 45	2 – 30
Field rise time, μs	5 – 12	6 – 35
Setup dimensions, mm	40×250	$200 \times 100 \times 200$

In order to check the properties of this new pulsed dipole experimentally a prototype has been set up (Fig. 2.3(b)). The prototype consists of a small plastic (PVC) case in which multi-turn (copper rings) or single-turn (insulated wire) coils can be installed and fixed precisely. A secondary short (200 mm length) vacuum chamber, used as a drift chamber, is equipped with a scintillator window. The magnetic field produced inside the dipole was measured by a small inductive probe. The elec-

trical parameters such as inductance and resistance of the coils are derived from the discharge current signals. The measured distribution and magnitude of the magnetic flux were in agreement with performed simulations. Besides the off-line experiments, the new pulsed dipole was tested with accelerated heavy ion beams at the HHT experimental area at the GSI. For different number of layers and for various parameters of the electrical circuit the ion-optical properties of this dipole were investigated [Var00b]. The relevant parameters of the "$\cos 2\theta$" strip-line as well as of the "Helmholtz-coils" high-current pulsed dipoles that have been measured in these experiments are given in Table 2.1.

2.3.2.2 Simulation of ion-optical properties: VARDIOS code

For a precise description of the ion optical properties of systems containing pulsed high-current magnets a new computer code, called VARDIOS[6] has been developed [Var98a, Var02a]. The code is based on the novel *differential algebra* (DA) technique [Ber98]. Using this method, VARDIOS is able to calculate the transfer matrix of a system up to an arbitrary order with the machine precision of the matrix elements. While the transfer map is obtained by Runge-Kutta integration of the equation of motion, all the computations are performed in terms of DA-vectors instead of real numbers.
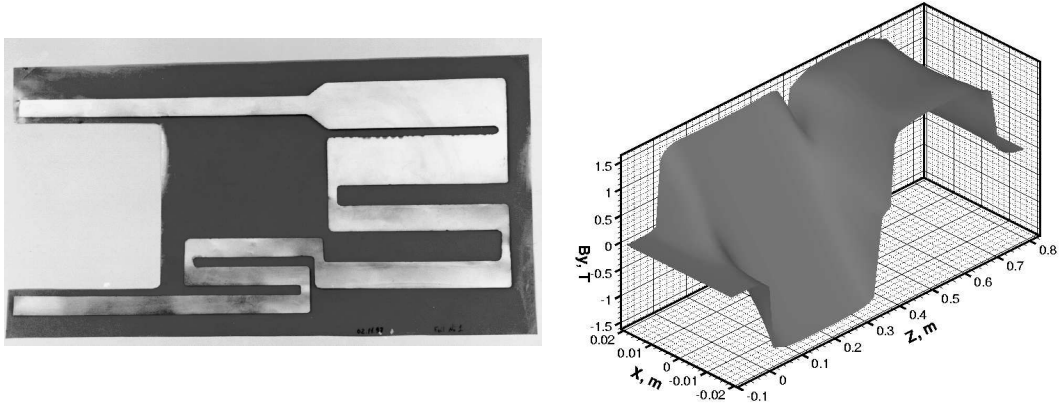

Figure 2.5: Left: Copper/kapton foil of a combined-function pulsed strip-line magnet (single-layer quadrupole followed by a double-layer dipole, the pulsed spectrometer prototype [Var98a]). Right: Main component of the magnetic field inside the magnet (the same foil) calculated by the VARDIOS code.

The 3D magnetic flux density distribution of a particular system (see Fig. 2.5) is also calculated in terms of DA-vectors at each step during the integration. Thus the influence of a non-ideal magnetic field distribution inside a lens as well as all the fringe field effects are taken into account correctly. The entire computation procedure is completely independent of the calculation order as the maximum order of the transfer maps is limited only by the power of a computer system.

The ion optical coordinate system proposed by H. Wollnik [Wol87, Ber87] is used in the code. Computed transfer matrices therefore can easily be compared with results obtained by the codes GIOS, GICO and COSY INFINITY. The entire code is written in the C++ language and contains a highly-optimized DA-computation and function library.

---

[6]VARious Differential-algebra Ion Optical Systems

A particle tracking routine is also included in the code. Elliptical and parallelogram-like initial phase-space areas with different density distributions can be considered. The VARDIOS code has a plain high-level input language, similar to those of the GIOS and GICO codes.

While performing computer simulations of the ion-optical properties of various pulsed magnetic lenses, a significant difference in the transfer matrix elements of this lenses compared to conventional magnets has been observed even in the first order [Var02a]. Higher-order aberrations of pulsed lenses may differ from those of conventional magnets by a factor of 50 and more. Another noticeable effect is a strong influence of the axial (B_z) component of the fringing fields, which is usually suppressed in conventional iron-dominated magnets by a specially shaped yoke (thus, is always neglected), whereas for a pulsed magnet it can play an important role.

It has been demonstrated [Var02a] that the VARDIOS code is able to calculate transfer maps of systems containing pulsed magnets up to arbitrary order. Realistic 3D magnetic field distributions and all the fringing field effects are taken into account correctly. The results of the computer simulations have shown, that the existing transfer matrix based ion optical codes, where the ideal multipole field distributions and fringe fields typical for iron-dominated magnets are assumed, cannot be used for a precise description of pulsed high-current magnets. The transfer matrix elements of pulsed lenses differ significantly from those of conventional magnets.

After the general overview on the slowing down of heavy ion beams in matter and high-energy-density (HED) matter research with intense heavy ion beams that has been given in the beginning of this chapter, in the last section the benefits of the ELD diagnostics in HED experiments have been discussed and the requirements for a magnetic spectrometer needed for the ELD measurements have been described. The performed experimental and theoretical studies on the new generation of high-current pulsed magnetic lenses have also been reviewed. These compact and inexpensive magnets can be an attractive alternative to conventional steel-dominated or superconducting magnets, as to be used in the construction of an ELD spectrometer as well as for other applications. However, as a result of the performed investigations it is to be concluded, that *it is a challenge to obtain a 5 % energy resolution with any magnetic spectrometer*, given by the special requirements (sec. 2.3.1). In order to overcome the above difficulties for the ELD diagnostics, a new non-magnetic spectrometer based on an original principle has been developed. This instrument, called the *scintillating Bragg-peak* (SBP) spectrometer (chap. 4) has been successfuly used in real experiments on heavy-ion beam induced HED matter (chap. 5).

3 Experimental setup and methods

In this chapter the GSI accelerator facilities, HHT ("high temperature") experimental area, ion beam and target diagnostic methods as well as target preparation issues relevant to the energy-loss dynamics experiments are discussed.

3.1 GSI accelerator facilities and HHT experimental area

The accelerator facilities at GSI offer a unique possibility worldwide for experiments on heavy-ion beam induced high-energy-density in matter. Intense beams of highly energetic heavy ions that are delivered by the heavy ion synchrotron (SIS-18) are used at the HHT ("High Temperature") experimental area to heat large volumes of matter at solid density to extreme conditions of temperature and pressure. The accelerator related issues of the GSI facilities important to the experiments at the HHT area are described below.
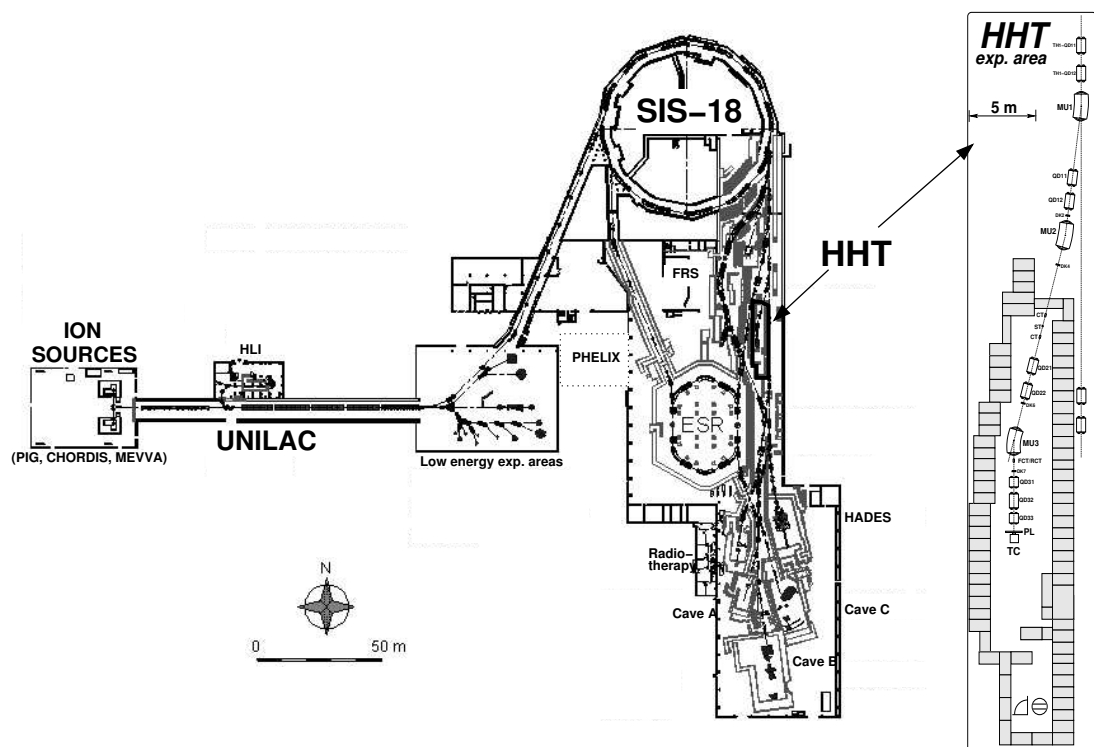

Figure 3.1: GSI accelerator facilities and layout of HHT experimental area.

3.1.1 Intense heavy ion beams at SIS-18

The beams of heavy ions are first produced and pre-accelerated at the ion source area (see Fig. 3.1). Two different high-current ion sources can be used simultaneously. There are a number of ion source types, e. g. PIG (*PennInG ion source*), MEVVA (*MEtal Vapour Vacuum Arc*), MUCIS (*MUlti Cusp Ion Source*) and others which are available. For the HHT experiments a source which provides the maximum current of a given ion species is preferable. The particles produced by an appropriate ion source are then accelerated in a linear accelerator UNILAC (*UNIversal Linear ACcelerator*). The UNILAC has two acceleration stages with different RFQ-accelerating structures optimized for the acceleration of high-current heavy ion beams. UNILAC can deliver intense beams of heavy ions of the energy from 1.4 AMeV to 20 AMeV. After acceleration, these beams can either be extracted for experiments at the "low energy" experimental hall or can be guided into the transfer channel to SIS-18 for further acceleration (Fig. 3.1). There is a stripper installed inside the transfer channel which allows to increase the charge state of ions before injection into the synchrotron.

After acceleration in the UNILAC linear accelerator, the heavy ion beam is injected into the synchrotron SIS-18. The injection energy is about 11.4 AMeV. In the heavy ion synchrotron SIS-18 which has a circumference of 216 m, maximum bending power of 18 Tm and RF acceleration 0.8–5.6 MHz at 16 kV, intense beams of heavy ions can be accelerated up to 2 AGeV energy (1 AGeV for uranium ions). To increase the beam intensity in the ring, a *multiturn* injection scheme is used, where the ions are injected over several revolution periods and fill the entire transverse phase space acceptance of the ring.

Since 1998 an electron cooler is in operation at SIS-18. Using the electron cooler it is now possible to increase the intensity of the ion beam in the ring by several times. For this purpose a *multi-multiturn* injection scheme is employed. The transverse emittance of the ion beam is reduced due to interaction with a co-axial low-emittance electron beam in the electron cooler. This takes place between successive multiturn injections from the UNILAC. Electron cooling increases the phase space density of the beam and therefore the number of particles that can be accumulated at a given acceptance of the synchrotron. For instance, with 20–25 injections using multi-multiturn scheme it is possible to accumulate about $4 \cdot 10^9$ of $^{238}\text{U}^{73+}$ ions in the SIS-18 that can then be accelerated and delivered for experiments. Currently the SIS-18 synchrotron is able to deliver beams of more than $2 \cdot 10^{10}$ ions of ^{86}Kr, $6 \cdot 10^{10}$ ^{40}Ar ions and more than 10^{11} ions of lighter species. The current work on optimization of the accelerator performance ensures that the intensity of the beams of the heaviest (uranium) ions will be significantly increased in the nearest future.

Typically, in the experiments at the HHT, the heavy ion beams with energies of 200–400 AMeV are used. The acceleration in SIS-18 is performed at the fourth harmonics of the accelerating RF-field and the beam therefore consists of four *bunches* during the acceleration. A special debunching/rebunching scheme has been developed at the GSI: after the acceleration stage the RF-voltage is reduced to the minimum and therefore the beam is redistributed uniformly over the whole length of the ring. In this way a *coasting* beam is formed. The RF-voltage is then raised again at the first harmonics compressing the coasting beam into a single bunch. A better compression can be obtained using a special *fast bunch compres-*

sion method [Spi99]. In this case after the adiabatic compression the RF-voltage is quickly increased to its maximum value. This leads to a rotation of the beam in longitudinal phase space and much shorter bunches can be generated. With the RF system that is presently available at the SIS-18 (maximum RF-voltage of 16 kV) it is possible to reduce the duration of the ion beams down to 250 ns (FWHM) using the fast bunch rotation technique [Spi99]. A new bunch compressor cavity which is currently being constructed will allow one to obtain the beam pulses shorter than 100 ns.

After the acceleration in the SIS-18 synchrotron and rebunching, the beam is extracted and guided to the high energy experimental areas. For the experiments at the HHT the *fast extraction* mode is required. In this mode the beam is bent from its synchrotron orbit by a fast magnetic *kicker* ($\tau < 90\,ns$) to an extraction channel in the septum magnet. All particles are extracted within one revolution period.

3.1.2   HHT experimental area

High energy, high intensity heavy ion beams extracted from the synchrotron are transported to the HHT experimental area in a special *beamline* (Fig. 3.1 , right). The total length of this beamline from SIS-18 to the target chamber is about 75 m and the maximum bending power of its magnets is 10 Tm. The last 30 m long part of the beamline is used only for the HHT experimental area and consists of three bending dipole magnets, two quadrupole doublets and one quadrupole triplet. Various beam diagnostic instruments and vacuum control devices (not shown in Fig. 3.1) are also built into the beamline.

A view of the HHT target area is presented in Fig. 3.2. A special final focusing device, the *Plasma Lens* (PL) [Ste96] is installed before a vacuum target chamber. The ion beam is penetrating in the PL along the axis of a high-current (430 kA) low-pressure (argon, 1–10 mbar) gas discharge. The azimuthal B_θ component of magnetic field (6 T) of this discharge, with its magnitude almost proportional to the radius, enforces an axial symmetric (i. e. simultaneous, both in X and Y planes) focusing of the ion beam.

Using the plasma lens, intense heavy ion beams can be focused to a $400-800\,\mu m$ FWHM spot, depending on the beam emittance. Such a strong focusing is possible due to a large focusing angle (short focal distance) provided by a high magnetic field gradient in the PL. A careful alignment of all the ion optical elements in the beamline is required to avoid beam losses and to produce a beam of optimum geometry (10-20 mm wide, parallel beam) at the entrance of the PL for best focusing.

Because of the plasma lens, the target chamber cannot be directly connected to the high-vacuum beamline. The beamline is closed by a thin ($20-40\,\mu m$) kapton window behind the last quadrupole magnet. The discharge volume of the PL is enclosed between entrance (thin kapton and titanium foils) and exit (carbon and kapton) vacuum windows. The exit window of the PL is located at a distance of about 15–25 mm from the interaction point inside the target chamber. The focal distance and focal spot size are adjusted to the target by changing the PL discharge parameters.

A rectangular-shaped vacuum target chamber is equipped with a cryogenic system for the production of solid cryo-targets (sec. 3.3), a precision robot-like target manipulator and several vacuum windows and feedthroughs for diagnostics. The chamber can be pumped down to $10^{-6}\,$Torr pressure. Various advanced instru-
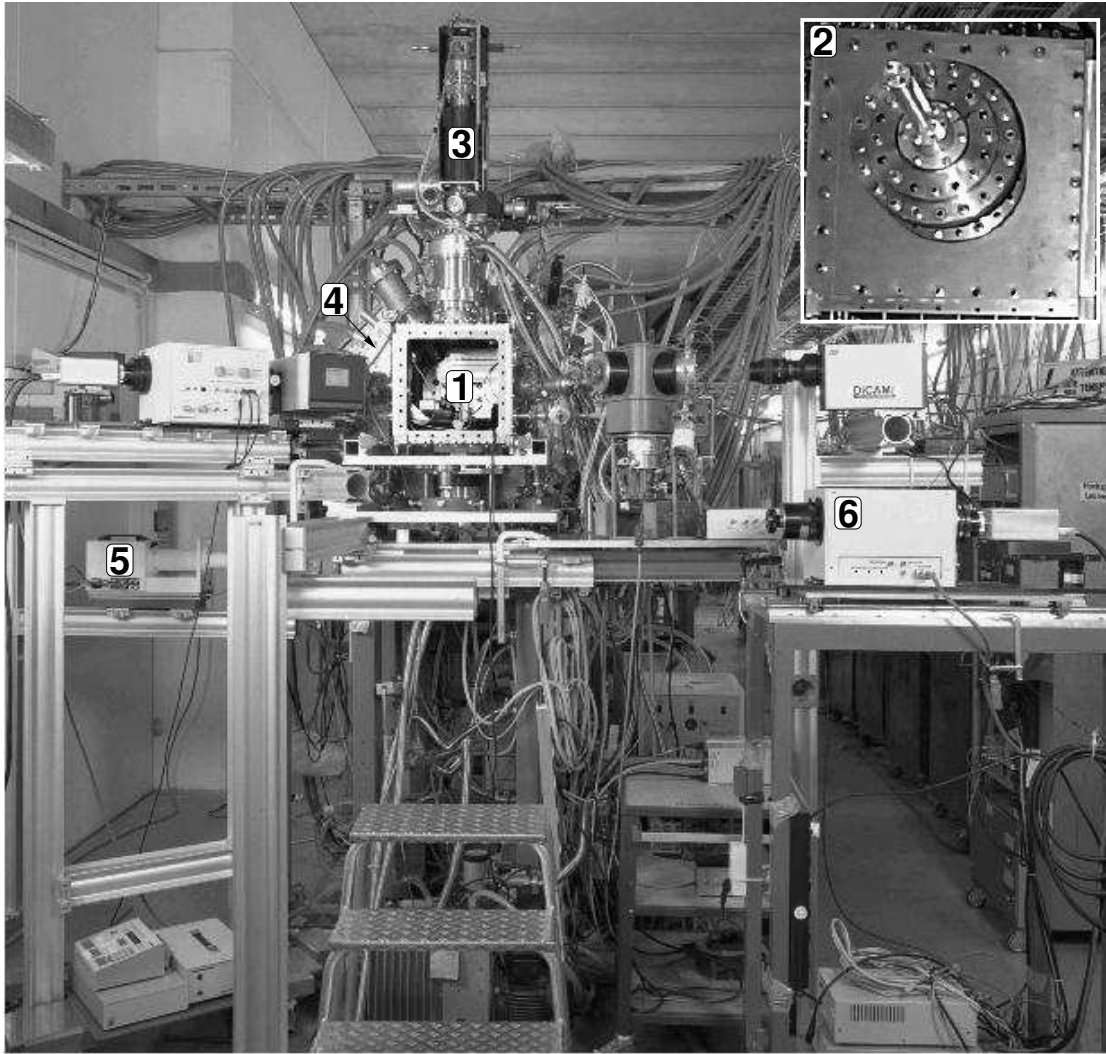
Figure 3.2: HHT target area (upstream view). 1 — target chamber (back wall removed), 2 — SBP energy-loss spectrometer and beam dump mounted on the back wall of the target chamber, 3 — manipulator of the growing chamber, 4 — plasma lens, 5 — framing camera and 6 — streak camera of the SBP spectrometer.

ments including high-resolution cooled CCD cameras, an electronic fast framing camera, visible and VUV spectrometers and streak cameras are available for beam and target optical diagnostics.

3.2 Ion beam characteristics and diagnostics

For the experiments on high-energy density in matter it is important to measure and control the following characteristics of the ion beam:

- beam intensity (i. e. the total number of particles in the beam);

- temporal shape of the ion beam pulse;

- location of the focal spot and the beam envelop;

- focal spot size and transverse distribution of the beam intensity at the target position;

- energy of the projectiles at the target.

With the fast extraction mode the longest possible beam pulse duration is about $1.5\,\mu s$, limited by the discharge time of the pulse-forming network of the extraction kicker. However for the beam energies of about 300 AMeV, the limiting factor is the revolution time of a coasting beam in the ring, which is $1.1 - 1.4\,\mu s$. At the moment, the shortest available pulses have a duration (FWHM) of $250\,ns$. It is expected that the pulse duration can further be reduced to below $100\,ns$ when the new bunch compressor cavity is set into operation at SIS-18.

The intensity of the beam and its temporal profile are measured by a number of different beam current transformers installed in the HHT beamline. These are the *Fast Current Transformer* (FCT), the *Integrating Current Transformer* (ICT) and the *Resonant Current Transformer* (RCT, HEBT CT). The FCT transformer [Ber91a] is used for precision measurements of the time shape of the beam pulse. It allows the measurements of the beam profile with better than 5 ns time resolution. The ICT transformer [Ber91b] has a slower response (30 ns time resolution) and is more convenient for the beam intensity measurements. The signals from these devices can be recorded by an oscilloscope at every beam shot. The RCT current transformer [Sch96b, Ree01] was developed at GSI and has recently been installed at the HHT beamline as well. This device does not provide time resolution but it was especially designed for precision measurements of the total number of particles over a very wide (from 10^5 to 10^{12}) range of the beam intensities. The RCT setup contains a fast transformer of a different type that can also be used to monitor the time profile of the beam [Sch96b]. The readout of the RCT is integrated into the standard GSI accelerator control software and the intensity of every experimental shot is logged [Sch01a]. This is also done for radiation safety reasons: the transmission from the SIS-18 to the experimental area can be monitored in this way for every beam pulse and saved on a disk together with the total amount of particles delivered to an experimental area.

There is no beam current transformer installed near the Plasma Lens due to a high level of electromagnetic noise produced by this device. However it has been proven [Fun99a] that the transmission through the PL is almost 100% if the beam is carefuly aligned at the PL entrance window. The position and spatial distribution of the beam at the entrance of the PL is monitored by a quartz (M382, HERAEUS QUARZGLAS) or aluminum oxide scintillator. A thin scintillator with about $30 \times 30\,mm$ area is mounted at a $45°$ angle to the beam axis and can be moved to the beam position by an electro-pneumatic manipulator. The light emission from the scintillator is recorded by a fast CCD camera (FlashCam, PCO) connected to a computer. In this way the position of the beam axis as well as the transverse shape of the beam at the entrance of the PL can be diagnosed. The beam-guiding elements in the beamline are adjusted to obtain the desired spatial parameters of the beam before an experiment.

Diagnostics of the beam intensity distribution near the focal spot is more difficult. The energy density of an intense ($10^9 - 10^{11}$ particles/pulse) beam focused to a sub-millimeter spot is so high that usual scintillating materials saturate. Moreover, the energy deposited by the focused beam even in a very thin scintillator can damage ("burn") the scintillator. Using a scintillator material that is highly resistive to heat and radiation damage (such as quartz M382 scintillator), it is possible monitor the position of the beam axis. However, reliable information about the beam intensity distribution at the focal spot cannot be obtained by such measurements. In

order to measure the beam envelop and the focal spot size near the target position, a gas fluorescence has been recorded. For this purpose the target chamber was filled with nitrogen at about 500–900 mbar pressure during the beam alignment procedure. The nitrogen molecules are excited by the accelerated beam ions and the fluorescence from ionized or neutral molecules at the wavelengths 350–470 nm is dominant [Pet01]. High pressure of the monitoring gas is chosen to increase the light emission signal.
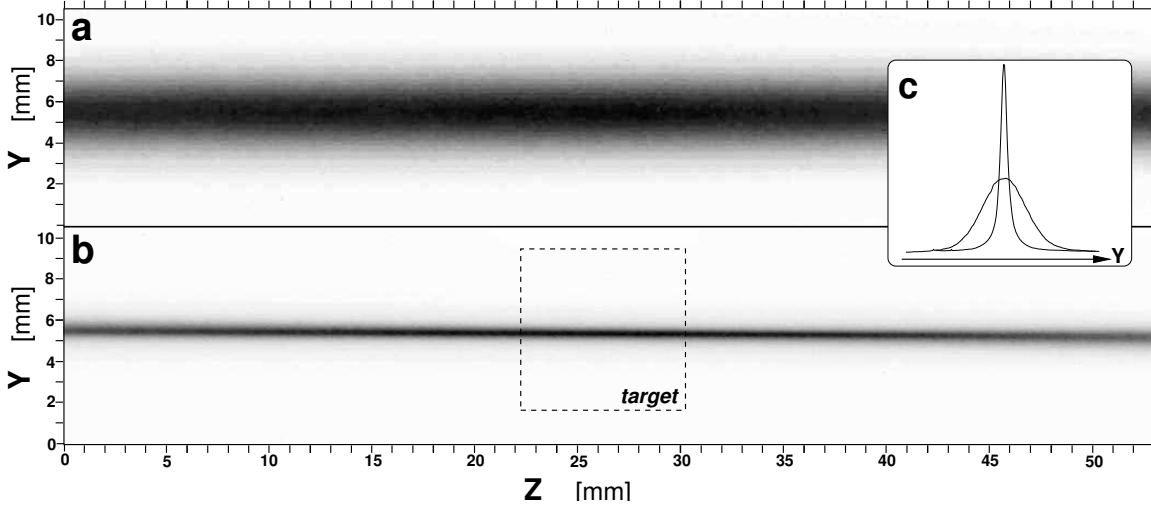

Figure 3.3: Gas fluorescence images of the ^{238}U, 253 AMeV beam near the target position. **a** — unfocused parallel beam (plasma lens is switched off), **b** — beam focused by PL (FWHM$\approx 470\mu m$), the target location and dimensions are indicated, **c** — beam intensity distributions near the focal spot.

The emitted light is recorded by a high-resolution cooled CCD camera (DICAM PRO, PCO). The fluorescence images give the information about the beam envelop and beam intensity distribution in Z–Y plane near the target position (Fig. 3.3). With a small mirror which is moved by the target manipulator behind the beam axis at $45°$ angle it is also possible to record beam intensity distribution in Z–X plane on the same image. The radial distribution $I(r)$ of the beam intensity can be unfolded from the recorded projections $I(y)$ by solving the Abel's inversion problem, e. g., using a fast and reliable algorithm of fitting by series of Gauss functions [Ign02]. However, since in all our experiments the beam intensity profiles could be well fitted by a Gauss function, the Abel's inversion had not to be applied.

By recording the gas fluorescence images, one can measure the focal spot size and the radial distribution of the beam intensity at the target location. In addition to that, the position of the beam axis and transverse shape of the beam are monitored with a quartz scintillator array which can be moved to the interaction point by a target manipulator.

Since in the present experimental setup the ion beam has to pass through a set of foils, the entrance and the exit windows of the Plasma Lens, the initial energy of the projectiles at the target is not the same as the energy of the ions delivered by the SIS-18, which is known to a good accuracy ($10^{-3} - 10^{-4}$). However, for detailed simulation of the beam–target interaction phenomena the initial energy of the beam *at the target* is needed. It may be important to take into account energy loss and energy loss straggling in these windows, especially for the heaviest projectiles and relatively low initial energies. The energy loss of an ion beam in these windows can

be either measured (e. g. by the SBP energy loss spectrometer) or calculated. The relevant issues are discussed in sec. 4.2.2 on p. 52.

3.3 Cryogenic rare gas solid targets

In the experiments described in this thesis rare gas solids (RGS) were employed as targets. These are cryogenic crystals of rare gases **Ne**, **Ar**, **Kr** and **Xe**. The RGS targets have a number of attractive properties compared to other targets:

Efficient preparation. Since in our experiments a target is destroyed by the intense heavy ion beam, a new target has to be prepared for every following experimental shot. This can easily be done with RGS targets. A new cryogenic crystal can be grown within 5–15 minutes depending on the type of the used gas. The whole target preparation procedure is fully remote-controlled and therefore no access to the target area is needed during the experiments.

Optical transparency. The RGS targets are optically transparent from infrared to the vacuum ultraviolet (VUV) spectral region, allowing direct optical access to the beam-target interaction volume. This is an indispensable property for applying various optical diagnostic techniques. The optical diagnostics that can be used simultaneously to the ELD measurements include active methods like shadowgraphy or laser interferometry to investigate hydrodynamic response of the target (expansion, propagation of compression waves) as well as spectroscopic measurements of the target self-emission in different spectral ranges that allows to determine the target temperature.

Reproducibility. Keeping the same crystal growing conditions ensures high reproducibility of the target properties. The spatial shape of the crystal is exactly defined by the shape of the growing chamber.

Low binding energy. Low binding energy of the RGS allows to obtain rapid hydrodynamic response of the target material even if an ion beam of only moderate intensity (a specific energy deposition $\mathcal{E} \leq 1\,kJ/g$) is available for experiments.

Easy changing materials. It is easy to change the target material during an experimental series without a need in re-evacuating the target chamber. The list of materials which can be used to prepare a solid-density target includes all the rare gases as well as solid nitrogen, deuterium or hydrogen.

An elaborate cryogenic system is available at the HHT experimental area [Fun98, Fun99a], allowing remotely controlled preparation of RGS targets of different materials and geometries in an evacuated target chamber. The operating scheme of the cryogenic system is shown in Fig. 3.4. The main parts of the system are the cold head and the movable growing chamber. The massive copper cold head is cooled by liquid helium to the minimum temperature of 6 K. On the surface of the cold head, made of oxygen-free copper, a thin layer of indium can be placed to improve the thermal contact and the vacuum sealing between the cold head and the growing chamber. The growing chamber is attached to a precision four-axis manipulator (OMNIAX TRANSLATOR, VACUUM GENERATORS) located on top of the target chamber, which is pumped down to a $10^{-5} - 10^{-6}\,$Torr pressure. Other elements of the system include a wide-range temperature sensor and a gas supply system with an
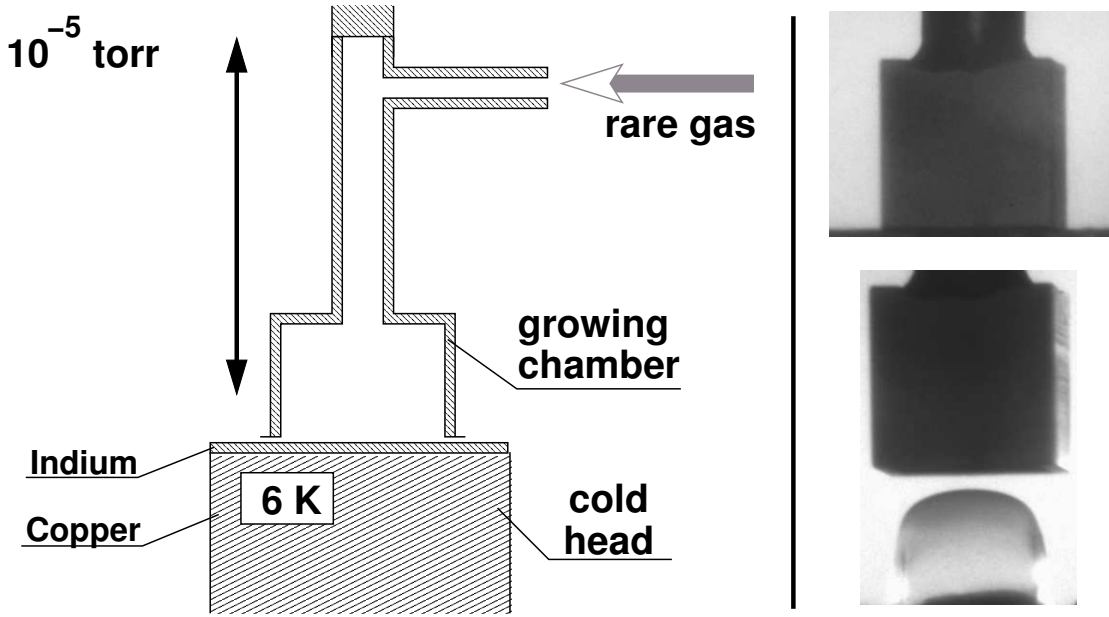
Figure 3.4: Scheme of the cryogenic target preparation system (not to scale). The procedure of growing a cryogenic crystal is demonstrated by the photographs on the right.

automatic feed-back pressure control. A detailed description of the whole cryogenic target preparation system as well as the description of the crystal growing technique and underlying physics are given in [Fun99a].

The procedure of preparing a RGS target is as following. First, the growing chamber is moved down to contact the cold head (see Fig. 3.4, top image). The volume of the chamber is then filled with a gas of interest to a certain pressure through a gas-feeding pipe on top of the chamber. The growing pressure and the growing time is chosen to achieve the best quality of the crystal. For example, for preparation of a solid neon target a pressure of about 90 mbar is preferable and a crystal under such conditions is growing layer by layer directly from the gas phase within about 15 minutes. The growing pressure is kept constant during the growing process. After the crystal is formed the growing chamber is evacuated and lifted upward (Fig. 3.4, bottom image). The shape of the crystal is exactly defined by the shape of the growing chamber. In our experiments the crystals were cubes with a base area of $8 \times 8 \, mm^2$. The faces of the crystals were oriented perpendicular to the beam axis.
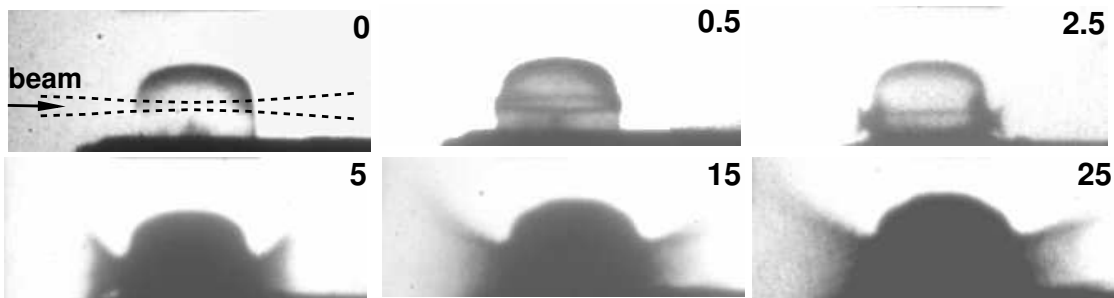

Figure 3.5: Framing-camera images of a RGS target during and after the interaction with an intense heavy ion beam, demonstrating the hydrodynamic response of the target material. The temporal location of an image after the beginning of irradiation is given in microseconds (top-right corner). The ion beam duration was about $1 \, \mu s$.

A qualitative idea of the hydrodynamic response of RGS targets to heavy ion beam heating is given in Fig. 3.5. In this figure images of a solid neon target taken by a fast framing-camera are shown. The target was backlit in visible range. Intense heavy ion beam delivered within about $1\,\mu s$ pulse penetrate through the target and heat a small volume in the center. The energy deposited by the beam leads to an increase in the target temperature in the heated volume. This, in turn, generates a pressure gradient driving a density wave (or a shock wave) outward in radial direction. Simultaneously, the evaporated target material is expanding from the front and back surfaces of the target. When the density wave moves outward, the crystal material is melting or evaporating, the crystal order is destroyed and the crystal loses its transparency in the visible range. At much later times the entire crystal material expands.

It is to be noted that the energy-loss dynamics measurements probe the target during the first $1-2\,\mu s$ when the ion beam is still available. As it has been demonstrated by the present measurements, already on this short time scale the line density along the axis can drop by a factor of three or more. Although it cannot be clearly seen from framing images (Fig. 3.5), this effect is caused by the density wave which is rapidly moving outward in radial direction during the heating phase and that leads to formation of a low-density channel around the axis.

4 Scintillating Bragg-peak spectrometer

The usefulness of the ELD diagnostic technique (time resolved measurements of the energy loss of intense ion beam during the interaction with a target) and its advantages for heavy-ion-beam induced high-energy-density matter experiments have been briefly discussed in sec. 2.3. Special requirements for an instrument which is needed for such measurements as well as the challenges in a design of a magnetic spectrometer for this purpose have been also described.

In this chapter a new device which has been developed and employed for the ELD measurements [Var01, Var02b] is introduced. This time-resolving energy loss spectrometer is based on original principle and is called *scintillating Bragg-peak* (*SBP*) spectrometer.

The operating principle of the SBP spectrometer is based on the effects of the slowing down of an ion beam in the bulk of a fast scintillating material (Fig. 4.1). When ions penetrate the matter, the energy deposition (or energy loss) profile along the penetration depth follows the well-known *Bragg curve* $\mathcal{S}(x)$ with a peak corresponding to the *range* $\mathcal{R}(E)$ of the ions (see sec. 2.1). There is a direct relation between the range of the ions and their energy for a given target material. Therefore the idea behind the SBP spectrometer is to use the information on the penetration depth (range) of the projectiles in order to deduce the particle energy (Fig. 4.1). If the range of the projectiles can be recorded and moreover, if the time evolution of range can be registered, one can obtain time-resolved information about the beam energy distribution. This is the operating principle of the SBP spectrometer in its simple form.

In the SBP spectrometer the projectile ions escaping the target in the vicinity of the beam axis are stopped in the bulk of a fast organic (plastic or liquid) scintillator. The specific luminescence profile along the ion penetration depth in the scintillator is recorded at every time moment by an electronic streak-camera. The energy loss
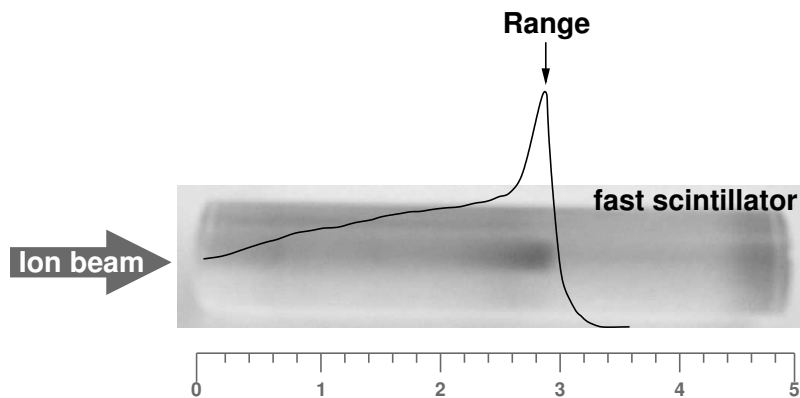
Figure 4.1: SBP spectrometer operating principle.

dynamics of the ion beam is deduced from this data applying special processing and analysis (sec. 4.2).

4.1 Design and construction

The layout of the SBP spectrometer setup is shown in Fig. 4.2. The main parts of the spectrometer are a collimator holder, a scintillator holder with a slit window and a streak unit. The instrument is installed behind a carbon beam-dump which has a 10 mm aperture along the axis. The distance between the target and the scintillator material is about 86 cm, depending on the target location in the chamber. Due to the large focal angle of the ion beam, only a small part (less than 0.2 %) of the incident ion beam that escapes the target in the vicinity of the beam axis enters the scintillator. Most of the beam is stopped in the beam-dump.
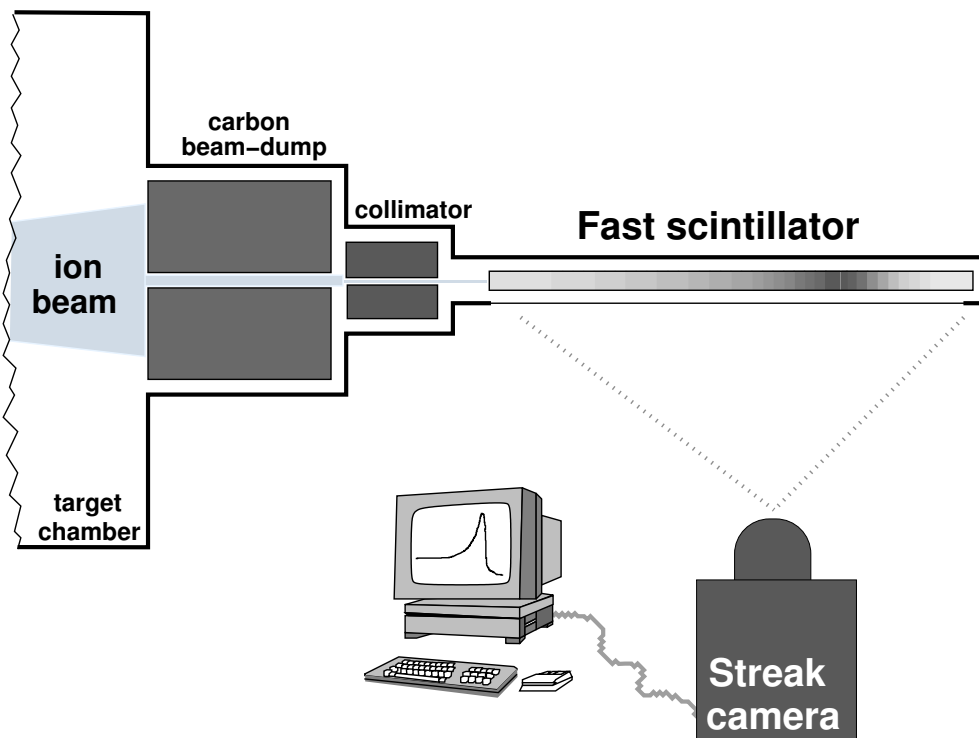
Figure 4.2: Scheme of the scintillating Bragg-peak spectrometer (not to scale).

Modular lead or aluminum collimators with 1 mm aperture and about 50 mm

length are installed in front of the scintillator in order to select only the ions escaping the target with small angles around the beam axis. The ions that pass the collimator are stopped in the scintillating material.
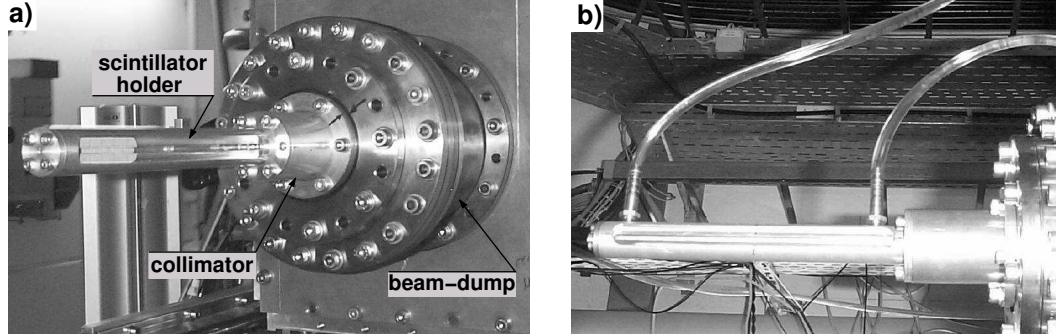
Figure 4.3: SBP spectrometer with plastic **a)** and liquid **b)** scintillators mounted behind the back wall of the target chamber.

There are two different constructions of the scintillator holder available. One where a plastic scintillator block can be installed and the second for a liquid scintillator with a re-circulation system (Fig. 4.3). Both holders have the same mounting flanges and similar design. The variation of ranges in the scintillator for different ion species and different beam energies is rather large, varying from a few millimeters for uranium projectiles of several hundreds AMeV to more than ten centimeters for lighter ions, like carbon or oxygen. Therefore the scintillator length can be varied and a maximum length of 20 cm can be observed through the window in both holders. In case of a plastic scintillator the vacuum part of the setup (i. e., the evacuated target chamber) is closed by the scintillator block itself, with its front face pressing a rubber O-ring behind the collimator unit. In the liquid scintillator construction an additional thin (about $40\,\mu m$) kapton window between the scintillator and the vacuum part of the setup is installed.

Relevant properties of the scintillators which have been used in the ELD experiments are listed in Table 4.1. These organic scintillating materials have been chosen due to the small decay time and low price. Although a plastic scintillator is highly resistant to radiation damage, during the experiments it was replaced after a few dozen of shots. This was necessary to ensure that there is no influence of the scintillator degradation on the measurements. The risk of damaging ("burning") the plastic scintillator is especially high during the beam alignment procedure which is usually done before the measurements. For efficient beam alignment the target area is irradiated with a high repetition rate. In this case either an additional beam-dump should be installed between the target and the spectrometer or the scintillator should be replaced before the physical measurements are done.

In order to avoid the need to access the experimental area and re-evacuating the target chamber during the measurements, a modified spectrometer construction has been designed. In this construction a liquid scintillator is used instead of the plastic one (Fig. 4.3). The liquid scintillator is continuously refreshed in a closed-loop clean circulation system, driven by a small peristaltic pump. The pumping speed is sufficient to exchange the entire irradiated volume ($1-2\,cm^3$) of the scintillator in between the shots. Due to a smaller density of the liquid scintillator and therefore longer ranges of the ions, range resolution for the heaviest ion species and lowest beam energies is also slightly increased. However, the plastic

Table 4.1: Fast organic scintillators used in the SBP spectrometer.

	plastic **BC-408**[1] (PILOT F)[2]	*liquid* **BC-517H**[1] (NE235H)[2]
Chemical base	polyvinyl-toluene	mineral oil
Density, g/cm^3	1.032	0.86
Decay time, ns	2.1	2.0
Refractive index	1.58	1.476
No. H atoms per $cm^3, (\times10^{22})$	5.23	7.06
No. C atoms per $cm^3, (\times10^{22})$	4.74	3.73
Ratio H:C atoms	1.104	1.89
Wavelength of max. emission, nm	425	425
Light output, $\% \, antracene$	64	40

[1] Specifications as given by BICRON®.
[2] Old notation, NE TECHNOLOGY®.

scintillator has higher light output and it is much easier to handle. Consequently, since both the constructions of the spectrometer with plastic and with liquid scintillator have their advantages, both have been employed in the experiments.

The light emitted from the scintillator is observed by a fast electronic streak camera (Hamamatsu C2830, sweep unit M2548) through a slit window in the scintillator holder (Fig. 4.2). The streak camera is installed perpendicular to the scintillator axis. A narrow (a few tens of μm) slit at the entrance of the streak camera cuts a longitudinal profile of the incident light along the scintillator axis. Two-dimensional (specific luminescence profile along the ion penetration depth versus time) scintillation images on the exit screen of the streak camera are recorded by a cooled high-resolution (1024x1024 pixels) CCD camera (Hamamatsu ORCA). The readout from the CCD camera is done with a personal computer.

4.2 Data processing and analysis

4.2.1 Unfolding the energy spectrum.

In the first ELD experiments [Var01], the average range of the beam ions in the scintillator was determined by fitting a piece-wise defined analytical function which describes well the Bragg-curve behavior to the experimental luminescence profiles, $I(x,t)$. One of the fitting parameters of this function was representing the location of the Bragg-peak or a specific point in the steep slope of the curve behind the maximum. The fitting procedure was necessary for a reliable detection of the location of the range, taking into account a high level of noise in the original data. Using a range-energy calibration function for the scintillator which was taken from SRIM calculations, the ELD data was then obtained.

However, such a simplified data analysis procedure is valid only for a mono-energetic beam. If the beam has a finite width of the energy distribution and moreover, if the energy distribution is asymmetric, an additional systematic error is introduced by the data processing. Asymmetric energy distributions of the beam are a typical case in real target experiments. These asymmetries are mainly caused by
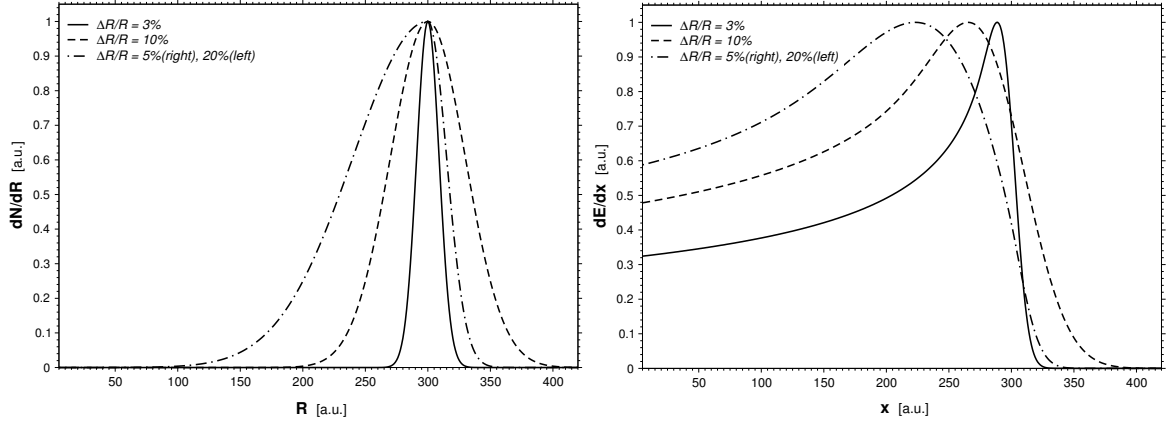
Figure 4.4: Calculated Bragg-curves (right) for different range/energy distributions of the ion beam (left): narrow Gaussian distribution (solid line), wide Gaussian distribution (dashed line) and asymmetric Gaussian distribution (dash-dotted line). All the energy distributions have the same location of the maximum.

a non-perfect collimation. In Figure 4.4 the specific luminescence profiles (Bragg-curves) calculated for different energy distributions of the incident beam are plotted. It is seen that a data processing procedure in which only a location of a certain point on the Bragg-curve is deduced from the experimental data can introduce a large (up to 25% or more) systematic error. Furthermore, the level of this systematic error cannot be evaluated if the energy distribution function is unknown. Therefore a more accurate model shall be used for the experimental data analysis. Such a model is described below.

4.2.1.1 Problem formulation

The specific luminescence profile along the penetration depth x of the ion beam in the scintillator at every moment in time is given by the following expression:

$$
\begin{aligned}
I(x,t) = \frac{dL}{dx}(x,t) &= \int_0^{E_{\max}} \frac{dE}{dx}(E,x) \; \frac{dN}{dE}(E,t) \; dE \\
&= \int_0^{E_{\max}} \mathcal{S}_{\mathrm{sc}}(E,x) \quad \mathcal{F}_{\mathrm{E}}(E,t) \quad dE,
\end{aligned}
\tag{4.1}
$$

where $\mathcal{S}_{\mathrm{sc}}(E,x)$ is the stopping power of the scintillator to an ion with initial energy E, penetrated the distance x, i. e., the "Bragg-curve", the energy loss of an ion along the penetration depth (see sec. 2.1.1) and $\mathcal{F}_{\mathrm{E}}(E,t)$ is the energy spectrum of the beam at time t. The maximum energy of the ion beam energy spectrum, $E_{\max}$ can be replaced by infinity in the most general case. In equation (4.1) some minor effects such as nuclear fragmentation of the incident beam in the scintillating media and non-linear response of the scintillator are neglected. Influence of these factors will be discussed in detail later (sec. 4.3.3 and sec. 4.3.4).

The spectrometer records the specific luminescence $I(x)$ with time resolution. The aim of the data analysis is to deduce the energy spectrum $\mathcal{F}_{\mathrm{E}}(E)$ from the recorded luminescence profiles. The equation to be solved is an integral Fredholm equation of the first kind. Even if the stopping power ($\mathcal{S}_{\mathrm{sc}}(E,x)$ — the *kernel* of the equation) would be known exactly, the solution of Eq. (4.1) for $\mathcal{F}_{\mathrm{E}}(E)$ which is often called *unfolding* or *deconvolution* is a typical example of so-called *mathematically ill-conditioned problem*. This means that any small errors or noise in the "right-hand side" of the equation, $I(x)$ tend to be drastically amplified in the solution.

Such *inverse problems* need special numerical methods and a lot of care during the solution [Tik87].

4.2.1.2 Stopping power of the scintillator

In order to unfold the energy spectrum of the ion beam from Eq. (4.1) one has to know the kernel of the equation, i. e. the stopping power of the scintillator $\mathcal{S}_{\mathrm{sc}}(E, x)$ for a given ion species. Since direct precision measurement of the function $\mathcal{S}_{\mathrm{sc}}(E, x)$ for different ions in a wide energy region is a challenging task, calculated stopping data has been used in the data analysis. In fact, stopping power of such light targets as organic scintillators to heavy ions has been intensively studied in nuclear physics experiments that had already started in early sixties. A large amount of experimental data is available, in particular for such popular materials as scintillators and nuclear emulsions.

The results of the computation of the stopping power with modern computer codes (SRIM [Zie96], ATIMA [ATI] and others) even for the heaviest ions such as uranium, in the *intermediate energy region* from about 30 AMeV to 500 AMeV are in good agreement with each other and with available experimental data (see sec. 2.1.1). The deviations among different calculations and experiments in this intermediate (30–500 AMeV) energy region is usually not more than $\pm 2\%$ [Sch01b].

In the present ELD experiments the energy of the ions was changing from about 300 AMeV down to about 40 AMeV. Therefore for the stopping power and ranges the values calculated by advanced codes like SRIM can be used, taking into account the described (sec. 2.1.1) limitations and accuracy.

Therefore, in the data processing the stopping power $\mathcal{S}_{\mathrm{sc}}(E)$ and the range-energy relation, $\mathcal{R}_{\mathrm{sc}}(E)$ values for the scintillator were calculated by the SRIM code and then approximated by an analytic function. This analytic approximation [Sne99] represents the calculated data to an accuracy of better than 1% in all cases. This accuracy is not worse than the precision of the originally calculated values. The detailed description of the analytic approximation and all the relevant formulae are given in Appendix A, p. 91.

The use of the analytic relations has a number of important advantages compared to the tabulated data. First, given the analytic approximation for $\mathcal{S}(E)$, one has a smooth kernel for Eq. (4.1) which is defined at every point. This function can be readily substituted into a computer code for solving the deconvolution problem, while only empirical coefficients have to be given for particular ion species (see App. A). Second, all the relevant quantities such as energy loss in a given material thickness, energy loss spatial profile (Bragg-curve), $\mathcal{S}(E, x)$ and range-energy relation $\mathcal{R}(E)$ are available in a closed form after the stopping power approximation function $\mathcal{S}(E)$ is fitted to the calculated data.

4.2.1.3 Solution of the inverse problem

The developed solution algorithm for Eq. (4.1) is described below. This procedure is optimized both for the accuracy of the obtained results under the conditions of high noise background of the experimental data as well as for the efficient use of computer resources.

In order to obtain the energy spectrum $\mathcal{F}_{\mathrm{E}}(E)$ at every moment in time, Eq. (4.1)

can be written in the following form:

$$I(x) = \int_x^{\mathcal{R}_{\max}} \mathcal{S}_{\mathrm{sc}}(\mathcal{R}, x) \cdot \mathcal{F}_{\mathcal{R}}(\mathcal{R}) \, d\mathcal{R} \,, \tag{4.2}$$

where the existence of the direct relation $\mathcal{R}(E)$ between particle energy E and its range $\mathcal{R}$ for the given scintillator media has been used to replace the energy distribution function by the range distribution:

$$\mathcal{F}_{\mathrm{E}}(E) = \frac{dN}{dE}(E) \Longleftrightarrow \frac{dN}{d\mathcal{R}}(\mathcal{R}) = \mathcal{F}_{\mathcal{R}}(\mathcal{R}). \tag{4.3}$$

Accordingly, the slowing down profile of an ion in the scintillator, $\mathcal{S}_{\mathrm{sc}}(\mathcal{R}, x)$ in Eq. (4.2) is given in terms of particle range $\mathcal{R}$ instead of energy. This can easily be done when an analytic approximation for stopping is available (Eq. (A.9), p. 92).

In fact, Eq. (4.2) is not exactly equivalent to the original equation (4.1). In Eq. (4.2), by setting the lower limit of the integral to x, a sharp cut-off approximation for the stopping power has been implicitly assumed:

$$\mathcal{S}_{\mathrm{sc}}(\mathcal{R}, x) \equiv 0, \qquad x > \mathcal{R}, \tag{4.4}$$

or, in the energy domain

$$\mathcal{S}_{\mathrm{sc}}(E) \equiv 0, \qquad E < E_{\min}, \tag{4.5}$$

where $\mathcal{S}_{\mathrm{sc}}(E_{\min}) \approx \mathcal{S}_{\mathrm{sc}}^{\max}$. This cut-off approximation means that the influence of the *tail* of the Bragg-curve $\mathcal{S}_{\mathrm{sc}}(E, x)$ behind the stopping maximum is neglected. As a matter of fact this approximation is not as bad as it may look at the first glance.

The Bragg-curve of a single particle, i. e. without straggling or statistical effects such as energy or angular spread in the beam, has a very steep fall after the stopping maximum (the range). The relative weight of the tail in the Bragg-curve can be characterized by the ratio $\mathcal{R}(E_{\min})/\mathcal{R}(E)$. Even in the worst case of uranium projectiles, for which in plastic scintillator $E_{\min} \approx 3.5 \, AMeV$, this ratio is below 5% for $E > 50 \, AMeV$, whereas, for instance, for argon ions this ratio is less than 0.3%. Taking into account that in a numerical treatment of the problem all the functions are always defined as arrays of points and here the number of points is given by the resolution of the experimental scintillation profiles $I(x)$, the tail of the Bragg-curve would occupy only a few points at most. Finally, in the solution this cut-off approximation might lead to a broadening of the unfolded energy spectrum towards high energy end. However, the performed numerical tests have shown that this broadening is negligible.

There are a number of advantages in having the problem formulated in the form of Eq. (4.2). Equation (4.2) is a *Volterra equation of the first kind* in contrast to the original Fredholm equation (4.1). It is known that at least for moderate levels of experimental measurement noise, Volterra equations of the first kind tend to be much "better-conditioned" inverse problems than Fredholm equations. This is because the lower limit of the integral introduces a sharp step that efficiently spoils any smoothing properties of the kernel. This feature is even more pronounced in Eq. (4.2), where the positive diagonal entries of the kernel $\mathcal{S}_{\mathrm{sc}}(\mathcal{R}, \mathcal{R}) = \mathcal{S}_{\mathrm{sc}}^{\max}$ dominate the kernel matrix, making the solution much more stable. Moreover, due to the sharp increase of the kernel matrix entries toward the diagonal (the behavior of a Bragg-curve, $\mathcal{S}_{\mathrm{sc}}(E, x)$) the solution in not sensitive to small variations of the kernel itself.

Furthermore, both variables of the equation, x and $\mathcal{R}$ are now defined in the same domain. This allows one to simplify the solution procedure when all the functions are defined numerically in the same variable space as the original experimental data $I(x)$. The accuracy of the solution procedure also benefits due to this reason since no scaling or calibration is needed until Eq. (4.2) is solved.

In order to solve Eq. (4.2) several specialized numerical methods for inverse ill-posed problems have been tested. Iterative deconvolution methods like van Cittert's method [van31, Xu94] and its most useful modifications by Jansson [Jan70] and Gold [Gol64] are widely used for deconvolution problems in image processing and spectroscopy. However, in the case of the ELD data analysis they required a huge number of iterations (i. e. a lot of computer resources) and have not demonstrated a good reliability. The classical and the most universal and robust linear regularization method by Tikhonov [Tik77] implies a generalization of least-squares estimator for inverse problems with an *a priori* constraint on the smoothness of the solution. This method, although being one of the best for various problems in research and engineering, needs a large linear algebraic system to be solved. The solution of Eq. (4.2) using Tikhonov method requires therefore a lot of computing time. This is a critical issue because Eq. (4.2) has to be solved for every time moment and for a large number of measured images obtained in one experiment. While applying this method for the ELD data analysis problem it has been also found difficult to adjust the value of the regularization (smoothing) parameter for every particular set of data.

It is interesting to note that an effective solution method for the problem, both from the computing speed and the robustness of the solution procedure appeared to be the most trivial and straightforward. Remember that Eq. (4.2) is a Volterra equation whose kernel matrix is lower triangular, with zero entries above the diagonal. It is known that such matrix equations are efficiently solvable by forward substitution. Therefore one can obtain *the exact* solution of Eq. (4.2) without much effort. Indeed this exact solution is not useful because the noise which is present in the measured "right-hand side", $I(x)$ is significantly amplified in the solution due to the ill-conditioned nature of the inverse problem. Nevertheless, for this particular problem a smoothing (noise filtering) applied to the exact solution of Eq. (4.2) gives good results. The solutions obtained is this way resemble the original function $I(x)$ with good accuracy while being stable to the noise in the experimental data.

The most appropriate noise filtering algorithm for the case seems to be the smoothing by discrete orthogonal polynomials, although some other methods like window averaging or median filtering have also been tested. Optimal order of orthogonal polynomials m as well as the number of smoothing cycles N have to be adjusted manually for a set of experimental data, although some theoretical studies on this problem are available as well [Sea88]. It is known that in general case of a polynomial filtering the signal-to-noise ratio improves as $N^{1/2}m^{1/2}$ while the distortions due to the smoothing grow as $N^{1/4}m^{1/2}$. Therefore it is always preferable to increase the number of smoothing cycles N rather than the order of the polynomial m. Typically for the present experimental data the *regularization parameters* $5 < m < 13$ and $10 < N < 100$ have been chosen, depending on the level of noise in the measured signals.
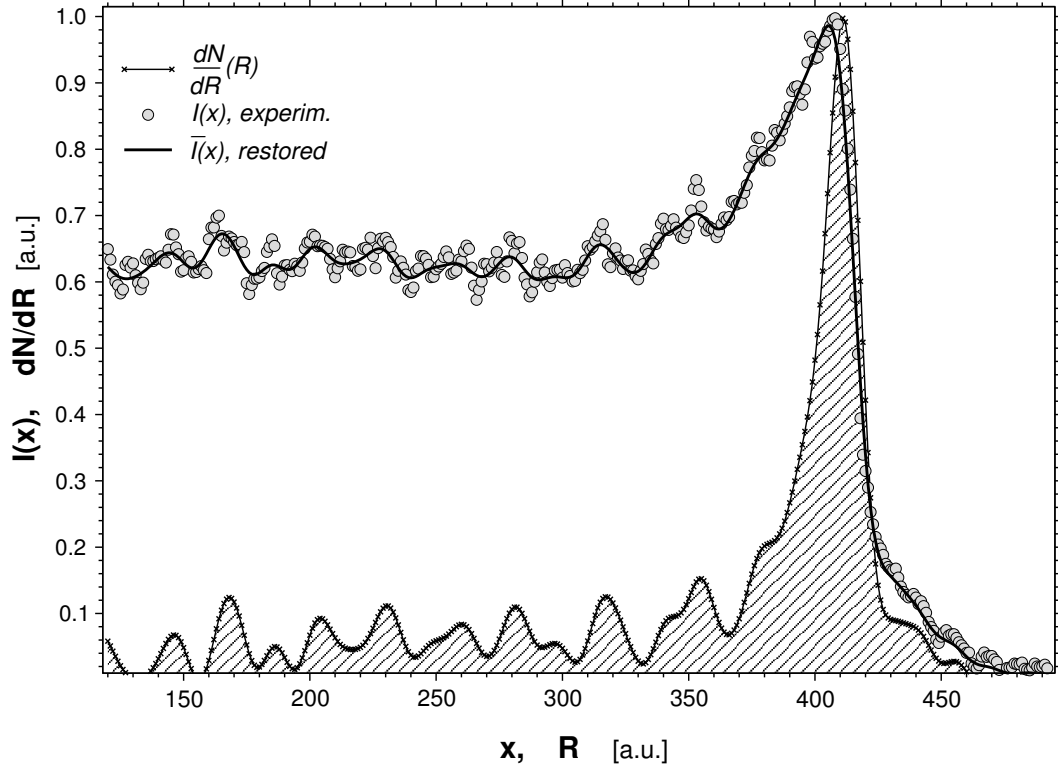
Figure 4.5: Example of the inverse problem solution in SBP data analysis. In the plot an original experimental scintillation profile at a certain time $I(x)$, the unfolded range spectrum $\mathcal{F}_{\mathcal{R}}(\mathcal{R}) = \dfrac{dN}{d\mathcal{R}}(\mathcal{R})$ and restored profile $\bar{I}(x)$ are shown.

4.2.1.4   Computer code and examples

In order to analyze the data from ELD experiments a computer code, called EL-DECON, in which all the above described ideas are employed has been written. The code takes the measured scintillator luminescence data $I(x,t)$ as input. The parameters of the stopping approximation $\mathcal{S}_{\mathrm{sc}}(E)$ (see App. A), regularization parameters (m and N) and others (like algorithm selectors) are given in a separate control file. Using this data the code computes the ion range spectra $\mathcal{F}_{\mathcal{R}}(\mathcal{R},t)$ solving the Eq. (4.2) with measured $I(x)$ for every time step.

An example of unfolding a range spectrum of a beam is shown in Fig. 4.5. The luminescence profile $I(x)$ is a "single line" in a measured streak image $I(x,t)$. The *restored* profile $\bar{I}(x)$ was calculated back using the Eq. (4.2) after the inverse problem has been solved and the range distribution $\mathcal{F}_{\mathcal{R}}(\mathcal{R})$ has been found. It is seen from Fig. 4.5 that in spite of the high level of noise in the experimental data the developed data processing procedure allows to unfold the range distribution in a stable way while resembling the original data with reasonable accuracy.

Due to the noise in the original experimental data the unfolded range spectra $\mathcal{F}_{\mathcal{R}}(\mathcal{R})$ contain numerical background noise typically on the level of 5–15 %, which cannot be fully suppressed. Therefore one cannot rely on the fine details of the unfolded spectra below this level. However, in all present experiments the range (energy) distributions at a given time moment are peaked and rather narrow functions (in the example shown in Fig. 4.5 $\Delta\mathcal{R}/\mathcal{R} \approx 5\%$) and the mean value of the range distribution above the noise level can be found with a good precision and reproducibility at every time moment.
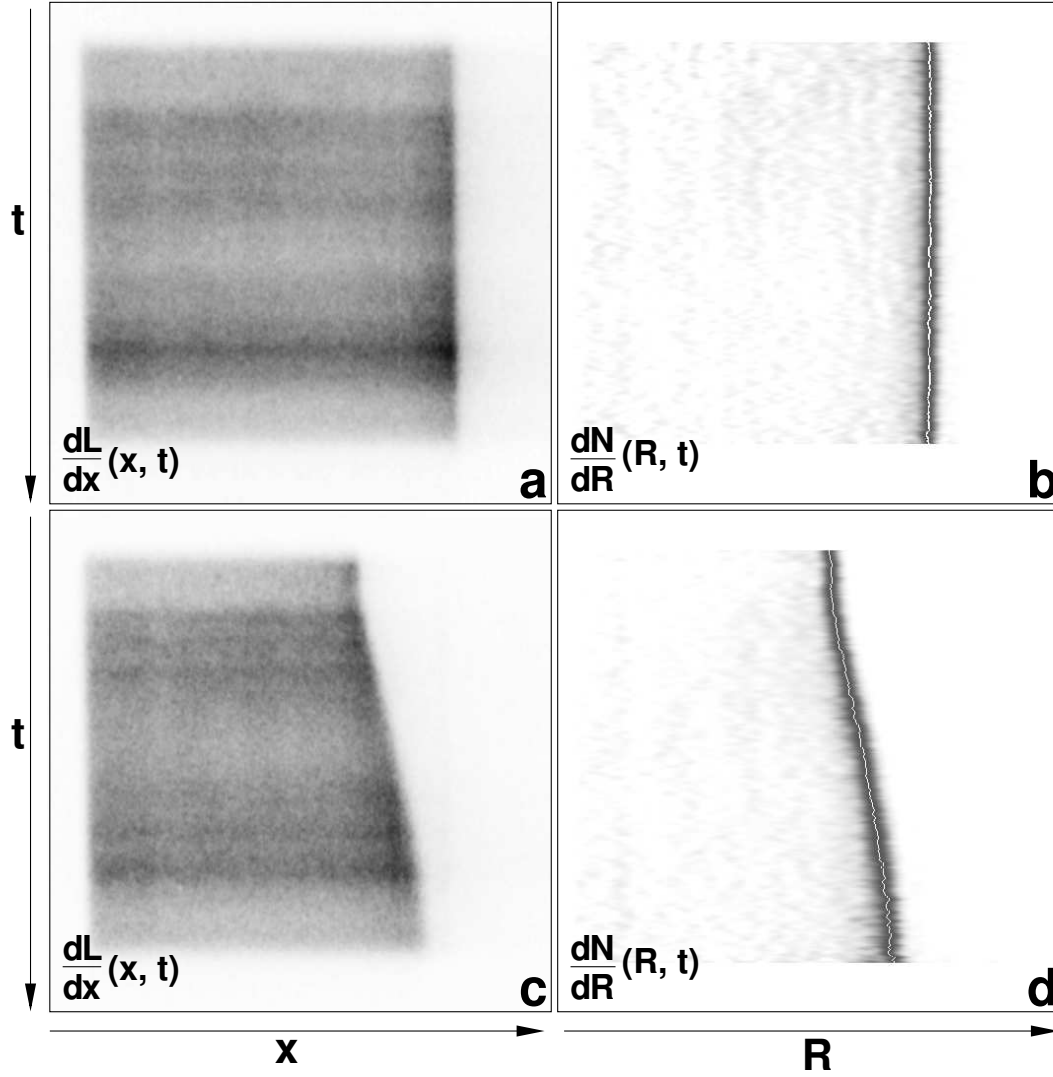
Figure 4.6: Example of ELD data analysis (ELDECON code). The processing of a calibration shot (top: **a**, **b**) for ^{40}**Ar**, 291 AMeV, as well as an ELD of the same beam interacting with solid xenon target (bottom: **c**, **d**) are shown. From the original experimental data $I(x,t) = \dfrac{dL}{dx}(x,t)$ (left: **a**, **c**) time evolution of the range spectra $\mathcal{F}_{\mathcal{R}}(\mathcal{R},t) = \dfrac{dN}{d\mathcal{R}}(\mathcal{R},t)$ (right: **b**, **d**) is unfolded. The variation of the intensity in the luminescence profiles $I(x,t)$ along the time (vertical) axis reflects the variation of the ion beam intensity within the pulse.

An example of a "full-scale" data processing with ELDECON code is shown in Fig. 4.6. In this figure two experimental streak images of the luminescence profiles in a scintillator are shown along with the unfolded range spectra. In this case Eq. (4.2) has been solved for every time moment, i. e. for every horizontal line of a streak image, similar to the profiles shown in Fig. 4.5, in order to obtain the corresponding range distribution. The *calibration shot* (Fig. 4.6, top) is simply a data record taken in the absence of a target. Therefore one cannot expect any time dependence of the beam energy and the range is constant in time (a "straight line" along the time (vertical) axis in the range distribution, see Fig. 4.6, **b**). Such "empty" shots are used for calibration purpose, in order to determine the initial range (energy) of the beam and to verify the measurements and data processing procedures.

In the bottom part of Fig. 4.6 unfolding of a time-dependent experimental data is demonstrated. In this case the ion beam is interacting with a target (xenon

cryogenic crystal). The line density of the target along the beam axis is decreasing due to the hydrodynamic motion induced by the ion beam heating. Accordingly, the energy of the ions escaping the target is increasing during the interaction. As a result the mean range of the beam in the scintillator is increasing as well (Fig. 4.6, **d**), as it has been recorded by the spectrometer. The variation of the intensity in the scintillation images along the time axis is due to the variation of the beam intensity within the pulse. Usually the intensity of the ion beam pulse is not constant, although time profiles of a beam can be close to a flat-top when a *coasting beam* is delivered by the accelerator (see sec. 3.2). The information on the beam intensity variation is important for computer simulation of the ELD phenomena (sec. 5.2.1) but it does not affect the described data processing.

4.2.2 Calibration and statistical post-processing

The solution of the inverse problem of Eq. (4.2), the range spectra $\mathcal{F}_\mathcal{R}(\mathcal{R}, t)$ of the ion beam is obtained from the original experimental data $I(x, t)$ with the ELDECON code as it was described in the previous section. It was also mentioned that due to relatively high level of numerical noise in the background of unfolded spectra one should not rely on the fine details in $\mathcal{F}_\mathcal{R}(\mathcal{R}, t)$. Therefore for further analysis only a reliable and well-reproducible value should be used. Such a value is the mean of the range distribution:

$$\mathcal{R}_\mathrm{m}(t) = < \mathcal{F}_\mathcal{R}(\mathcal{R}, t) > . \tag{4.6}$$

In fact, the value corresponding to the maximum in the unfolded range spectrum is taken as $\mathcal{R}_\mathrm{m}(t)$ in the processing. This is almost exactly the same as the mean value of a narrow peaked spectra and gives more reliable results otherwise. Other values such as width (FWHM) of a range spectrum and the accuracy of solution are also computed.

The next step is to calculate the energy loss dynamics $E(t)$ using the obtained time-dependence of the mean range $\mathcal{R}_\mathrm{m}(t)$. In order to avoid introducing unnecessary errors by scalings or calibrations in the intermediate steps of the data processing, all further calculations are performed in *relative variables*,

$$\tilde{E}(t) = \frac{E_\mathrm{m}(t)}{E_0}, \qquad \tilde{\mathcal{R}}(t) = \frac{\mathcal{R}_\mathrm{m}(t)}{\mathcal{R}_0} , \tag{4.7}$$

where E_0 is the initial mean energy of the ion beam when a target is absent, and R_0 is the corresponding initial range of the beam in the scintillator.

The value of $\mathcal{R}_0$ is known to a good accuracy after processing all the calibration shots, i. e. the data records of the initial beam without a target (see Fig. 4.6, **a**, **b**). During an experiment, the calibration data is recorded before and after every production shot (measurement with a target). This provides good statistics and therefore a good precision (a relative rms-error is typically less than 0.3 %) in determining the value of R_0.

To calculate the energy dynamics $\tilde{E}(t)$ from the time evolution of the ion ranges $\tilde{\mathcal{R}}(t)$ in the scintillator, a range-to-energy calibration function $\mathcal{R}_\mathrm{sc}(E)$ has to be known. This calibration is taken from the SRIM data fitted by an analytic function (App. A). The inaccuracy introduced by the SRIM scintillator stopping data should not exceed approximately 2 % (see discussion on p. 46). The reason for using the relative variables $\tilde{\mathcal{R}}$ and $\tilde{E}$ instead of the absolute values is that the calibration function $\mathcal{R}_\mathrm{sc}(E)$ if presented in a normalized form in terms of the relative

variables (Eq. A.10, p. 92) has only a very weak dependance on E_0. Therefore the accuracy in determining E_0 does not affect the accuracy of $\tilde{E}(t)$.

After the range-energy calibration is applied to data sets and the time calibration of the streak images is made as well, the resulting ELD data $\tilde{E}(t)$ from many different shots are processed statistically. The mean energy loss and its deviation is calculated for a given number of equally distributed time intervals (a histogram) using all the previously processed experimental data. Usually good results are obtained if about 150–200 experimental points per bin are available. The resulting ELD data ($E_{\mathrm{loss}}(t) = (1 - \tilde{E}(t)) \cdot 100\%$) can be seen for example in Fig. 5.2, p. 67.

Finally, the absolute value of the initial energy of the ion beam E_0 has to be found. The initial energy of an ion beam on the target E_0 is not exactly the energy delivered by the accelerator E_{acc} which is known to a very good precision ($10^{-3} - 10^{-4}$). Before entering the target chamber an ion beam passes through several thin windows such as entrance and exit windows of the plasma lens (sec. 3.1). The energy loss ΔE_{W} due to these windows has also to be taken into account. Two different ways have been used to determine the value of E_0.

Since the initial range in the scintillator $\mathcal{R}_0$ is measured to a good accuracy in the calibration shots, its value can be used to find the value of E_0. Using the range-energy relation $\mathcal{R}_{\mathrm{sc}}(E)$ and the absolute value of $\mathcal{R}_0$ one can calculate E_0. Even better accuracy can be obtained if the calibration shots for different initial ion energies E_{acc}^i with the corresponding absolute ranges R_0^i are available. The precision is limited basically by the accuracy to which the function $\mathcal{R}_{\mathrm{sc}}(E)$ of the scintillator is known. Moreover, the value of ΔE_{W} can be calculated. For this purpose the configuration and composition of the windows have to be known along with the stopping data for the window materials. The stopping data is obtained by SRIM and for efficient calculations the analytic approximation is employed (see App. A: Eq. (A.5), p. 91 and Fig. A.2, p. 93). Using both above methods the initial ion energy on the target, E_0 can be determined to a precision of 2–3 %.

4.3   Limitations and accuracy of the measurements

In this section the sources of noise and limitations of accuracy of the data obtained with a SBP spectrometer are discussed. All possible errors in the processed data can be divided into two categories, *statistical errors* and *systematic errors.* The statistical errors are caused by random noise or shot-to-shot fluctuations of the experimental conditions. These errors can usually be reduced by collecting a larger amount of experimental information or by improvements in the setup and data acquisition that increase the signal-to-noise ratio. The systematic errors are caused for instance, by limited accuracy of a mathematical model of the data processing or finite precision of a measurement instrument. These errors do not decrease by increasing the number of measurements and can only be estimated.

4.3.1   Statistical errors and noise

The main source of the statistical errors in ELD measurements is shot-to-shot fluctuations of the ion beam intensity. These fluctuations can be as large as 10–15 % and are caused mainly by instabilities in the ion source operation. A higher beam intensity leads to a more effective heating of a target and consequently to a faster hydrodynamic motion of the target material. In addition to that, slight variations or

jitter in the beam intensity temporal profile as well as possible fluctuations in the target material density add up to the statistical error. However, these errors can be efficiently reduced by accounting a larger number of shots. Therefore in order to obtain a sufficient data in an experiment it is necessary record the information from several dozens of similar beam-target interactions.

The second source of statistical errors is indeed the noise in the recorded streak images. The level of the noise is typically of the order of 5–10% and the main reasons are a thermal noise in the CCD chip, random noise in the MCP of the streak tube, especially when it is set to a high amplification level, random radiation and/or electromagnetic damage of the CCD (floating "dead pixels") and imperfections or dust on the optical elements. Although a "better statistics", i. e. larger amount of data also helps to reduce the influence of this errors, it is important to keep the level of noise to the minimum. This is due to the fact that the noise tends to be amplified during the data processing of individual shots while the amount of useful information that can be taken from unfolded energy spectra at every time moment and its reproducibility depends on the level of noise. Therefore one should always try to increase the signal-to-noise ratio of every individual measurement. Since the sensitivity of a streak camera is relatively low, the efficiency of collecting the luminescence photons is important. A careful electric and radiation screening of the recording instruments (streak unit, CCD camera and data cables) also helps to reduce the level of noise.

Judging from the experience, it is concluded that if a sufficient number of shots is recorded in an experiment and the whole setup is carefully optimized in order to improve the sensitivity and signal-to-noise ratio, the statistical error in the $E(t)$ measurements can be reduced to a level of 1–3 %. This is approximately the level of the systematic error due to the range-energy calibration. Therefore further reduction of the statistical error should only be done after revising the sources of the systematic errors.

4.3.2   Calibration and systematic error

The main source of the systematic errors in the measured and processed data is presently the range-energy calibration, $\mathcal{R}_{\text{sc}}(E)$ dependence of the scintillator. As it has been discussed in sec. 4.2.1.2, p. 46, the stopping power of the scintillator and the range-energy relation in the intermediate energy region (30–500 AMeV) can be calculated by modern stopping codes to a precision of the order of $\pm 2\%$. This is the systematic error level which is assumed for the processed data.

The situation can be improved only if precision measurement of the scintillator stopping power to a particular ion species is performed. If a higher degree of accuracy is needed, one should probably omit the range-to-energy calibration step and measure directly the kernel of Eq. (4.1), i. e. $\mathcal{S}_{\text{sc}}(E_0, x)$, the Bragg-curve of the scintillator to the ion beam at different energies. This has to be done in the same setup where the ELD measurements will be performed and for a large number of the initial beam energies E_0 that in turn have also to be known precisely. Moreover, the level of statistical error must allow for such precision measurements. Presently it is not possible to carry out such accurate measurements of the calibration function at the HHT experimental area and therefore the precision of the ELD data is limited to this systematic error.

4.3.3 Non-linear scintillator response

Non-linear effects in the plastic scintillator response (*quenching*) are known since early fifties [Bir52], when luminescent materials became widely used in counting and particle identification detectors in nuclear physics experiments. The detailed knowledge of the plastic scintillator response dL/dx to energetic heavy ions such as its relation to the stopping power $\mathcal{S}(E)$, atomic number Z and mass number A of nuclei is important for correct calibration of such detectors.

The first study of this problem was conducted by Birks [Bir52]. His semi-empirical model proposed that the incident particle excites a number of molecular structures in the scintillator which is linearly related to its stopping power $\mathcal{S}$, while "damaging" a fraction of them which is also proportional to $\mathcal{S}$. The latter were assumed to act as light-quenching agents with a certain efficiency. In the $\text{low}-\mathcal{S}$ region (for "minimum ionizing particles") the quenching is negligible and dL/dx is proportional to the stopping power.

However, this model is a simplified representation of the complex phenomena. Later experiments showed for example that ions having the same $\mathcal{S}$ but different Z give a different light output response. The result led to the conclusion that dL/dx depends on ionization density and not solely on the deposited energy. More specifically, it depends on the way how this energy is spatially distributed near the ion trajectory. In addition to that, dL/dx also depends on the way in which the deposited energy flows from the vicinity of ion trajectory to the luminous centers, for example, distribution of energy by the secondary electrons produced along the ion track. The complications involved in estimating all these effects are largely responsible for the fact that although a number of theoretical models have been developed (e. g. [Vol66, Mic95, MR99]), experimentalists mostly prefer simple semi-empirical expressions [Bir52, Bec76, Mat99] for calibration of their detectors.

Despite a number of experiments where the response of plastic scintillator to heavy ions has been investigated are available [Web73, Bec76, MR99, Mat99], no systematic experimental study on the problem covering the whole region of intermediate and low energies (0.5–500 AMeV) as well as wide range of ions up to the heaviest ones has been carried out. There is no "standard" formula which would describe correctly the quenching of plastic scintillator for the whole range of $\mathcal{S}$ and for all Z and A. In most of the experiments the calibration of plastic detectors is still done individually.

In order overcome the above difficulties, a possible influence of quenching on the SBP spectrometer data has been studied in general. Two different semi-empirical models of quenching have been implemented in the data processing code ELDE-CON. The influence of non-linear scintillator response on the processed experimental data have been checked by varying quenching parameters of these models over a wide region, from an assumption that this effect is negligible to almost total saturation of the scintillator response with respect to the stopping power.

The quenching effects can be accounted for the data processing by replacing the kernel of Eq. (4.2), the stopping power $\mathcal{S}_{\text{sc}}(\mathcal{R}, x)$ by a "scintillator response" $\mathcal{S}^{\mathcal{Q}}_{\text{sc}}(\mathcal{R}, x)$ which is related to the stopping power via a quenching model, $\mathcal{Q}$

$$\mathcal{S}^{\mathcal{Q}}_{\text{sc}} = \mathcal{Q}(\mathcal{S}_{\text{sc}}, \ Z, A, \dots). \tag{4.8}$$

Since $\mathcal{S}_{\text{sc}}(\mathcal{R}, x)$ in Eq. (4.2) can be normalized to $\mathcal{S}^{\text{max}}_{\text{sc}}$, the quenching function $\mathcal{Q}$ should be defined in the interval $\mathcal{S} \in [0, 1]$.

The first model that has been tested is the original Birks model [Bir52]:

$$\mathcal{Q}_{\mathrm{Bir}} = \mathcal{S}\frac{1+\kappa}{1+\kappa\,\mathcal{S}}\,, \tag{4.9}$$

where κ is the first order *quenching parameter* (later modifications of this formula included also higher-order dependency on $\mathcal{S}$ in the denominator). Another expression has been proposed by Matsufuji [Mat99]:

$$\mathcal{Q}_{\mathrm{Mat}} = \mathcal{S}^{1-\beta}, \tag{4.10}$$

where the quenching parameter β depends on mass and atomic number of ion, $\beta = \beta(AZ^2)$. The authors suggested a value $\beta \approx 0.4 - 0.7$ for heavy ions.

Since the correct values of the quenching parameters κ and β are unknown, they have been treated as free parameters, varying them in the ELDECON code from zero ("no quenching" limit, $\mathcal{S}_{\mathrm{sc}}^{\mathcal{Q}} = \mathcal{S}_{\mathrm{sc}}$) to very high values when the scintillator is assumed to be almost fully saturated (peak-to-plateau ratio in the Bragg-curve is close to unit) for the both models, $\mathcal{Q}_{\mathrm{Bir}}$ and $\mathcal{Q}_{\mathrm{Mat}}$.

At relatively small degrees of quenching no difference in the unfolded spectrum has been observed. Even when the quenching parameters have been increased to high values, higher than those proposed in previous studies [MR99, Mat99], the unfolded energy spectrum remains practically unchanged in the region around the maximum (see Fig. 4.5, p. 49). However, if one assumes that the scintillator response function approaches saturation (which is far from the real situation as it is clearly seen from the experimental data) the numerical noise below the peak region gains unphysical negative components. This is indeed an indication that the model assuming a high degree of quenching does not adequately describe the experimental data and that the real quenching parameter cannot be large. These results are the same for the both quenching models considered above.

A simplified qualitative explanation of the relative insensitivity of the unfolded spectra to the scintillator quenching degree can be as follows. As for a single ion, in the data processing only a rough "geometrical" feature is extracted from the luminescence profile — the range in the scintillator. The range does not depend on quenching while the absolute value of the scintillator response which is mostly affected by these effects, is of no importance for the data evaluation. Since in all the present experimental data the energy spectra are peaked and rather narrow, it is partly related to the whole processing procedure and implies relative insensitivity of the solution to smooth variations of the kernel in Eq. (4.2). The situation could be different in case of a broad energy spectrum. In this case neglecting the quenching effects would lead to a systematic overestimation of the "left wing" of the spectrum. In addition, the high level of noise in the experimental data does not allow to see any fine features before the maximum in unfolded spectra, where the influence of quenching should be most pronounced.

In view of the above discussion it is concluded that in the SBP data processing, while taking into account the level of noise in the experimental data, one can neglect the quenching effects in the scintillator response. In the worst case, the non-linear scintillator response may lead to a slight broadening of the peak of the unfolded energy spectra towards the low-energy end, but it practically does not change its location.

4.3.4 Projectile fragmentation in scintillator

During slowing down of an ion beam in the bulk of the scintillator, besides the energy loss due to elastic (Coulomb) interactions with electrons and nuclei of the target, inelastic processes (nuclear reactions) also take place. Projectile-like fragments are produced in peripheral nuclear collisions where only a few nucleons are abraded from the projectile nucleus (*fragmentation*). These fragments are emitted in a narrow forward cone and have about the same velocity as the projectile and a small momentum spread due to the reaction process itself. For heavy projectiles *fission* can also take place when two nuclei with atomic numbers of approximately one half of the primary are produced along with a few light fragments. This reaction is characterized by a wider momentum spread of the fragments although it's cross section is about an order of magnitude less than that for the fragmentation.

Due to the fragmentation the number of the projectile (primary) ions is continuously decreasing in the depth of a target (*attenuation* of the primary beam). The stopping for fragments scales with Z_f^2 and therefore the energy deposition profile of the beam along the penetration depth (Bragg-curve, $\mathcal{S}(x)$) taking into account nuclear reactions differs from those when only stopping due to the primary particles is considered. Firstly, fragments with smaller atomic numbers which are produced in "charge-changing" reactions have longer ranges and therefore penetrate deeper in the target. This leads to the formation of a "tail" of the Bragg-curve beyond the Bragg maximum of the primary ions. Secondly, since the stopping power for the fragments is somewhat smaller than for the projectile due to a smaller charge, Z_f the attenuation of the primary beam and build-up of lower-Z fragments reduces the value of $\mathcal{S}_{sc}(x)$ before the Bragg maximum as well as the value of $\mathcal{S}_{sc}^{max}$ itself, lowering the "peak-to-plateau" ratio of the Bragg-curve. It is to be noted that the reactions when the atomic number of the projectile is not changed ("isotopic" reactions) do not influence the Bragg-curve because the reaction products penetrate with almost the same velocities as the projectile.

Since the discovery of heavy nuclei in cosmic radiation [Fri48] fragmentation reactions have been intensively studied for many years. Experimental data on partial and total cross sections are available for many projectile-target combinations and for a wide range of beam energies. However, the amount of dedicated studies on the modification of the Bragg-curve due to the fragmentation of the projectiles in a thick target is rather limited. Such studies have been carried out for biomedical applications: for heavy-ion cancer treatment projects in LBL (Berkley, BEVALAC) [Sch71, Mac74, Sch89], GSI (Darmstadt, SIS-18) [Sch93, Sch96a, Sch96c, Krä00] and Chiba (Japan, HIMAC) [Yam92]. In these studies the modification of the energy deposition profiles in thick tissue-equivalent targets (like water, carbon, polyethylene etc.) due to fragmentation of light projectiles (^{10}**B**, ^{12}**C**, ^{16}**O**, ^{18}**F** and ^{20}**Ne**) has been investigated both experimentally and theoretically.

Figure 4.7 from reference [Sch96c] gives a good qualitative description of the Bragg-curve modification due to projectile fragmentation. The total energy deposition profile sums up from the contribution of the projectiles taking into account the attenuation of the primary beam and from the contributions of the fragment built-up along the slowing down path of the projectiles. These fragments contribute also to the region beyond the stopping maximum, forming the "fragmentation tail" of the Bragg-curve. The influence of higher generation fragments is negligible.

In order to take into account the above described effects of the projectile frag-
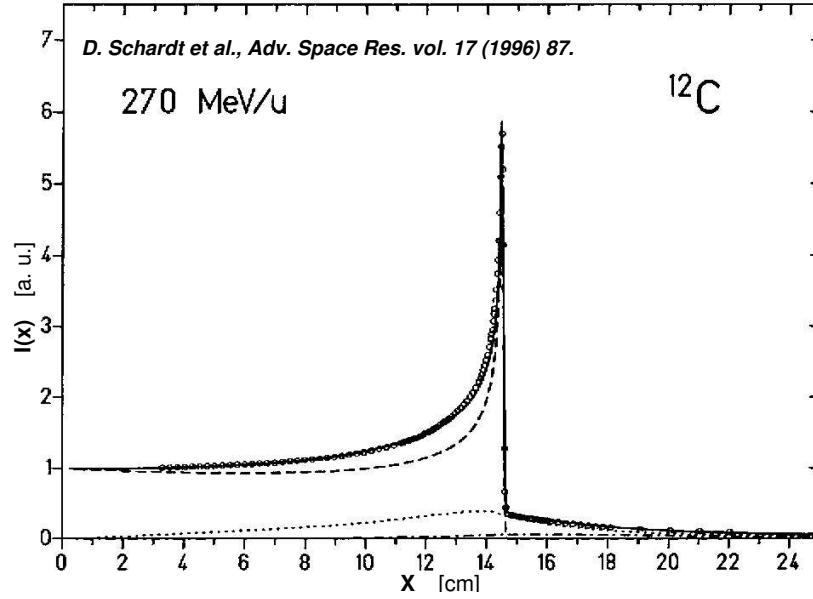
Figure 4.7: Measured Bragg-curve for 270 AMeV ^{12}**C** in water (circles) compared with model calculation [Sch96c]. The solid line is the total calculated Bragg-curve, the dashed, dotted and the dot-dashed lines are the contributions from the primary particles, from fragments and from fragments of secondary and higher generations, respectively.

mentation in the SBP spectrometer data analysis, Eq. (4.1), p. 45 can be written in the following form:

$$I(x,t) = \int_0^{E_{max}} \left(\mathcal{S}_0(E_0, x) \cdot \mathbb{A}(E_0, x) + \left[1 - \mathbb{A}(E_0, x)\right] \cdot \mathfrak{Frag}_0(E_0, x) \right) \mathcal{F}_{E_0}(E_0, t) \, dE_0,$$

(4.11)

where $\mathcal{S}_0$ is the stopping power of the scintillator to the projectile ions (Z_0, A_0) with initial energy E_0, $\mathbb{A}$ — is the total attenuation function of primary beam, $\mathfrak{Frag}_0$ is the contribution to the energy deposition from the fragments and $\mathcal{F}_{E_0}(E_0, t)$ is the energy distribution of the primary beam. Since the contributions from the higher-generation fragments is very small, it is neglected. Comparing Eq. (4.11) and Eq. (4.1) it is seen, that the kernel of the equation has been modified to represent the "scintillator response" taking into account the fragmentation of the beam.

The contribution to the Bragg-curve from the fragments (Z_i, A_i) which are built-up during the slowing down of the primary ions (Z_0, A_0) can be described as

$$\mathfrak{Frag}_0(E_0, x) = \sum_i Y_i(Z_0, A_0, E(x)) \left(\int_{E_i} \mathcal{S}_i(Z_i, E_i, x) \cdot \mathcal{F}_{E_i}(E(x), E_i) \, dE_i \right),$$

(4.12)

where Y_i is the yield of the fragment nucleus (Z_i, A_i) while the primary ion has energy $E(x)$ at the depth x in the scintillator $(E(0) = E_0)$, $\mathcal{S}_i(Z_i, E_i, x)$ is the stopping power of the scintillator to the fragment with atomic number Z_i and initial energy E_i, and $\mathcal{F}_{E_i}(x, E_i)$ is the energy distribution of fragments (Z_i, A_i). The main difficulty in calculating the $\mathfrak{Frag}_0$ function are the energy-dependent yields of fragments Y_i (i. e. the probability that a fragment (Z_i, A_i) will be generated from all possible nuclear reactions), which can be calculated only if all the partial fragmentation cross sections are known. This can be done relatively easily only for light projectiles like ^{12}**C** but it is a complicated task for the case of heavy ions.

The attenuation of the primary beam due to the fragmentation $\mathbb{A}$ is given by the following equation:

$$\mathbb{A}(Z_0, A_0, E_0, x) = \frac{N(x)}{N_0} = \exp\left(-n_{\mathrm{nuc}} \int_0^x \sigma_{\mathrm{tot}}(Z_0, A_0, E(\tilde{x}))\, d\tilde{x}\right), \qquad (4.13)$$

where σ_{tot} is the total (inelastic) nuclear reaction cross section, $E(\tilde{x})$ is the energy of a projectile ion at the depth $\tilde{x}$ in the target taking into account the slowing down process and n_{nuc} is the number density of the target nuclei.
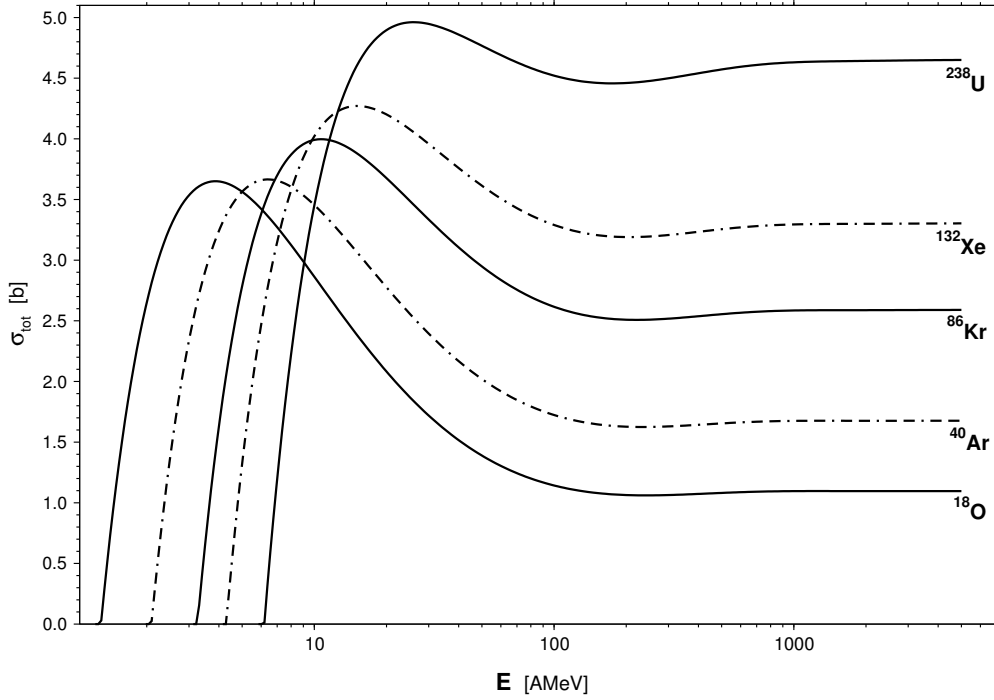

Figure 4.8: Total (inelastic) nuclear reaction cross section for different projectiles in plastic scintillator as a function of projectile's energy, calculated with semi-empirical model of Kox et al. [Kox87, Tow88].

The total reaction cross section $\sigma_{\mathrm{tot}}(Z,A,E)$ can be calculated using, for instance a semi-empirical parametrization by Kox et al. [Kox87, Tow88]. The total cross section in plastic scintillator (Tab. 4.1, p. 44) as a function of projectile energy is plotted in Fig. 4.8 for different projectiles. It is seen that for the energy region above 200–300 AMeV, σ_{tot} approaches a constant value of about 1–5 b for all the ions of interest. At low projectile velocities (energy below 10 AMeV) the reaction cross section is rapidly decreasing until the energy becomes too small to overcome the Coulomb barrier of the projectile-target system. As one can expect from a qualitative relation $\sigma_{\mathrm{tot}} \propto \pi R_{\mathrm{int}}^2$ (R_{int} is the interaction radius) the nuclear reaction cross section σ_{tot} is higher for heavier projectiles.

If the total energy-dependent fragmentation cross section is known, one can calculate the attenuation function of the primary beam in the depth of the scintillator $\mathbb{A}(x)$ using Eq. (4.13). Since in this study the relative modification of the Bragg-curve is important, it is helpful to plot the beam attenuation as a function of *relative depth* $x/\mathcal{R}$, where $\mathcal{R}(Z_0, E_0)$ is the range of a projectile in the target material. Using the Eq. (4.13), in Fig. 4.9 the calculated attenuation of the primary beam is plotted as a function of the relative depth for different projectiles (^{18}O, ^{40}Ar, ^{86}Kr and ^{238}U) with initial energy of 300 AMeV as well as for ^{238}U ions with lower energies (150 AMeV and 70 AMeV).
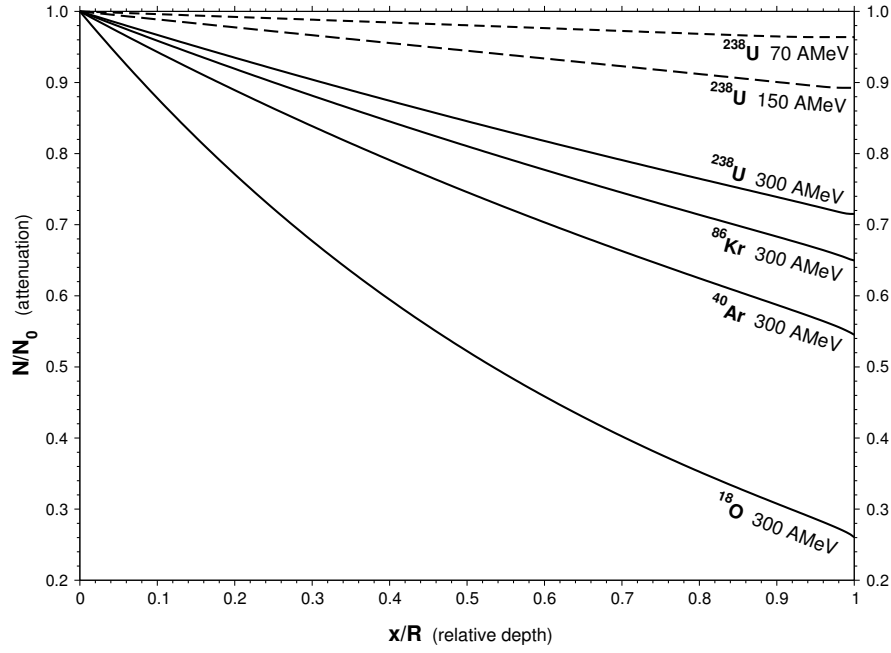
Figure 4.9: Attenuation of the primary beam in plastic scintillator target due to nuclear reactions as a function of relative depth. The curves are plotted for different projectiles with initial energies of 300 AMeV as well as for ^{238}U ions with initial energy of 300, 150 and 70 AMeV.

It is interesting to note that for heavier projectiles, in spite of a larger reaction cross section (see Fig. 4.8), the total attenuation of the beam $\mathbb{A}(\mathcal{R})$ is much smaller than for lighter ones. A beam of ^{18}O, 300 AMeV projectiles at the end of its range in plastic looses about 74 % of the primary ions due to nuclear reactions, while a ^{238}U beam of the same initial energy looses only about 28 % of the primary particles. This is beacause the ranges of heavy ions in matter are very short and scale as $1/Z^2$. Because of the short range (high stopping power), a heavy ion beam does not have "enough time" to meet a sufficient number of the target nucleai before it is completely stopped. For the same reason the attenuation of the beam is lower for smaller initial energies (see Fig. 4.9).

As discussed below, it is difficult to calculate exactly the contribution of the fragments $\mathfrak{Frag}_0$ (Eq. (4.12)) to the stopping profile $\mathcal{S}(x)$ for a heavy ion beam. This problem requires detailed quantitative information for all possible reaction channels such as the partial reaction cross sections. Already for simple projectile-target combinations the known partial cross sections have an error of about 10–30%. An accurate summation in Eq. (4.12) over a large number of all the reaction products also requires great care. However, one can estimate the upper and lower limits of the modification of the Bragg-curve due to the fragmentation for any projectile with a certain initial energy, provided the total reaction cross section σ_{tot} is known.

In the data processing for the SBP spectrometer, the influence of the fragmentation effects on the stopping profile $\mathcal{S}_{\mathrm{sc}}(x)$ (i. e., on the kernel of Eqs. (4.11) and (4.1)) is important before the Bragg maximum, $x \leq \mathcal{R}(E_0)$. Although the tail of the Bragg-curve beyond the stopping maximum of the projectile ions is often visible in the raw experimental data (see Fig. 4.5, p. 49), in the unfolded range distributions it is below the level of numerical noise. The upper limit for $\mathcal{S}_{\mathrm{sc}}(x)$ (the highest peak-to-plateau ratio) is given when all the fragmentation effects are neglected. The lower, "pessimistic" limit can be obtained if the attenuation of the primary beam

$\mathbb{A}(E_0, x)$ is taken into account but the energy deposition by the fragments is excluded ($\mathfrak{Frag} = 0$). These two "limiting" Bragg-curves are calculated and plotted in Fig. 4.10. The real stopping profile where all the fragmentation effects are included must lie between these two curves.
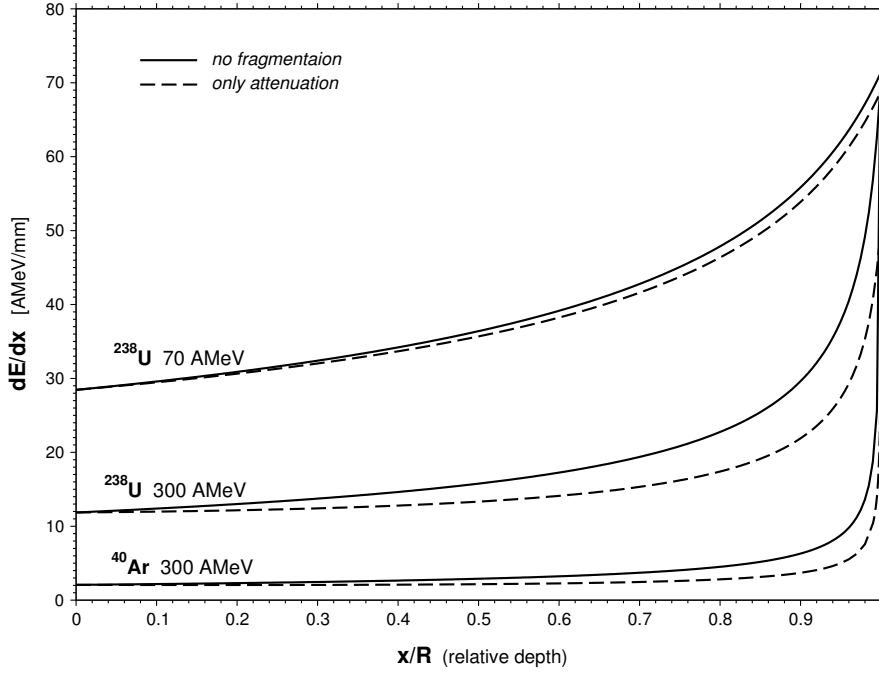

Figure 4.10: Upper and lower limits for the modification of the Bragg curve for the plastic scintillator up to the stopping maximum due to nuclear fragmentation effects. The stopping power profiles $\mathcal{S}_{\mathrm{sc}}(x)$ are plotted as a function of relative depth.

Because in the fragmentation reactions (peripheral inelastic collisions) the highest yields have the lightest fragments like **p** or α, corresponding to small changes of projectile atomic number, a realistic Bragg-curve will be much closer to the solid lines in Fig. 4.10 than to the dashed curves (lower limit) where the contribution of the fragments to the energy deposition profile is fully neglected (see also Fig. 4.7). In general, the modification of the Bragg-curve up to the stopping maximum due to the fragmentation of the projectiles (i. e. lowering the peak-to-plateau ratio) is very similar to the effects which one can expect from the non-linear response of the scintillator such as quenching or saturation of the scintillator response for high stopping powers (see sec. 4.3.3). Therefore, the discussion and the conclusions made in sec. 4.3.3, p. 55 can be applied to this case as well. In addition to that, the fragmentation will lead to a "broadening" of the Bragg-curve around the stopping maximum even for a mono-energetic primary beam and formation of the characteristic "tail" beyond the Bragg-peak.

Summarizing the discussion presented in this section it is seen that neglecting the projectile fragmentation effect in the SBP data analysis will only lead to a slight broadening of the unfolded energy spectra. These effects are more pronounced for light projectiles like ^{12}**C** or ^{16}**O** than for heavier ones (^{86}**Kr**, ^{132}**Xe** or ^{238}**U**) and are smaller for lower initial energies of the primary ions due to shorter range. The formation of the characteristic fragmentation tail beyond the stopping maximum of the Bragg-curve would be the biggest modification of the unfolded energy spectra of the primary beam. However, presently it cannot be reliably resolved in the data processing because of the high noise level the experimental data. Although it is

difficult to calculate exactly the Bragg-curve for heavy projectiles taking all the fragmentation effects into account, one can estimate the upper and lower limits of their influence. A precision calculation of the stopping profile can only be done if all the partial fragmentation cross sections are known.

5 Experiments and analysis of the results

The HHT experimental area as well as target preparation and ion beam diagnostics issues have been discussed in chapter 3 of this work. A detailed description of the developed SBP time-resolving energy loss spectrometer has been given in chapter 4 along with details of the data processing procedures and measurement accuracy limitations. In this chapter the results of recently performed ELD experiments as well as computer simulations of the observed phenomena are presented.

5.1 Description of the experiments and experimental results

5.1.1 General description of the performed ELD experiments

During the present study of the energy loss dynamics (ELD) of intense heavy ion beams interacting with dense matter, several series of experiments have been carried out. In these experiments the ELD data for intense beams of different ion species (^{238}U, ^{86}Kr, ^{40}Ar and ^{18}O), interacting with cryogenic rare-gas solid (RGS) targets (mainly solid **Ne** and **Xe**) have been recorded by the SBP time-resolving spectrometer. These are the first experiments of its kind.

Relevant initial ion beam and target parameters of the performed experiments are summarized in Table 5.1. For convenience, the experimental series are labeled by letters from (a) to (f), as it will be used in further referencing.

The intensity of the heavy ion beam has been measured for every shot as it was discussed in sec. 3.2. The intensity values given in Tab. 5.1 are the values averaged over all the experimental shots. The shot-to-shot fluctuation of the beam intensity was about 10 % or higher in different experiments. The temporal profile of the ion pulse has been measured in each experiment either by the fast beam current transformer (sec. 3.2) and/or has been taken directly from the data recorded by the SBP spectrometer (see sec. 4.2.1.4).

The intense heavy ion beams have been focused in a small spot in the center of a target by the plasma lens (see sec. 3.1.2). The focal spot size has been deter-

Table 5.1: **Initial beam and target parameters of the performed ELD experiments.**

	(a)	**(b)**	**(c)**	**(d)**	**(e)**	**(f)**
Projectile ion	^{238}**U**$^{73+}$	^{238}**U**$^{73+}$	^{238}**U**$^{73+}$	^{86}**Kr**$^{32+}$	^{40}**Ar**$^{11+}$	^{18}**O**$^{8+}$
Beam intensity[1], N_0	$1.2 \cdot 10^9$	$1.5 \cdot 10^8$	$1.8 \cdot 10^8$	$1.2 \cdot 10^{10}$	$5.5 \cdot 10^{10}$	$2 \cdot 10^{10}$
Ion's energy[2], $E_0 \, [AMeV]$	**190** (5)	**253** (3)	**307** (3)	**280** (10)	**291** (2)	**194** (2)
Focal spot size (FWHM)[3], $D_f \, [\mu m]$	590 (60)	470 (25)	490 (25)	825 (120)	740 (150)	790 (140)
Total beam energy, $E_{\mathrm{beam}} \, [J]$	8.7	1.5	2.1	46	102	11
Beam pulse duration[4], $\tau \, [\mu s]$	1.1	1.1	1.0	0.85	1.12	1.2
Spec. energy deposition[5], $\mathcal{E} \, [kJ/g]$	1.6	0.3	0.29	0.53	0.57	<0.1
Maximum temperature[6], $T \, [K]$	1760	215	205	4230	4830	—
Maximum pressure[6], $P \, [kbar]$	11	3.5	3.1	18	13	—
Target material	**Ne**	**Ne**	**Ne**	**Xe**	**Xe**	**Ne,Xe**
(density, $\rho_0 \, [g/cm^3]$)	(1.49)[7]	(1.49)	(1.49)	(3.4)[8]	(3.4)	**D$_2$** (0.202)
Target length, $\ell \, [mm]$	8	8	8	8	8	8
SBP spectr. scintillator type[8]	plastic	plastic	plastic	plastic	liquid	liquid

[1] Averaged total number of particles per pulse.

[2] Initial ion's energy on the target; approximate error value is given in brackets.

[3] Gaussian intensity profile in transverse plane, $D_f \approx 2.355 \cdot \sigma$. Accuracy of the values are given in brackets.

[4] Total duration of the ion beam pulse; time profile of the beam intensity is supplied in addition.

[5] Approximate value of the specific energy deposited in the target, estimated as $\mathcal{E} = 4 < \Delta E_{\mathrm{beam}} > /(\ell \, \pi D_f^2 \cdot \rho)$.

[6] Obtained from the corresponding computer simulations, see sec. 5.2.

[7] Normal density of the solid **Ne** at $T \approx 10 \, K$ [Kle77]; this value is in agreement with the present measurements.

[8] This value is confirmed by these ELD measurements; normal density of solid **Xe** is 3.78 g/cm^3 [Kle77].

[9] SBP spectrometer construction is described in sec.4.1 and scintillator parameters are given in Tab. 4.1, p. 44.

mined either by measuring the light emission of a quartz scintillator array or by the residual gas fluorescence measurements (sec. 3.2). Special effort has been taken in order to obtain the smallest possible focal spot with a round shape in the center of a target by adjusting the settings of the HHT beamline magnets and the plasma lens operating parameters (sec. 3.1). This was done during the beam alignment procedure before each experiment.

The initial ion energy on the target E_0 (see Tab. 5.1) is given taking into account the energy loss of the beam in vacuum and PL windows installed before the target (sec. 3.1 and sec. 3.2). These values are obtained from the calibration shots recorded by the SBP spectrometer as well as from calculations using SRIM stopping data for the windows materials (see sec. 4.2.2).

In all the ELD experiments described in this work cryogenic rare gas solids (RGS) have been employed as targets. The advantages of the RGS targets for present ELD experiments as well as the target preparation and handling issues have been discussed in sec. 3.3. For the experiments with ^{238}**U** projectiles ((a)–(c)) solid **Ne** target material has been chosen while for lighter ions solid **Xe** has been used (see Table 5.1). The density of the cold solid **Ne**, $1.49\,g/cm^3$ at $T \approx 10\,K$ [Kle77] is in good agreement with the present energy loss measurements. The **Xe** cryogenic crystals used in the experiments had the density of $3.4\,g/cm^3$, as it has been determined from the energy loss data in three independent experiments ((d), (e) and (f), Tab. 5.1), although the standard value of the solid **Xe** density (e. g., as given in [Kle77]) is $3.78\,g/cm^3$. This difference arises from the non-optimal growing conditions for **Xe** crystals: the maximum growing pressure allowed by the cryogenic setup was too low for the temperature of cold head (6–10 K) and the crystals have been quickly frozen directly from the gas phase far from the triple point [Fun99a].

5.1.2 Experiments (a) – (c): ^{238}**U** beams interacting with solid Ne targets

In the first of the performed experiments the interaction of an intense ^{238}**U** beam with solid **Ne** target has been studied (Tab. 5.1(a)). Initially, the range of a 190 AMeV uranium ions in solid neon is smaller than the length of the crystal. The beam is thus completely stopped in the target and therefore, for a certain period of time no data could be recorded by the spectrometer (see Fig. 5.1 and Fig. 5.5). However, due to the continuous heating of the target by the beam and the following hydrodynamic radial motion of the target matter, the line density of the target around the axis is continuously decreasing. As a consequence, the beam penetrates further and further into the target. At about 350 ns (not shown in Fig. 5.1) the projectiles escape the target and can be detected.

At later times, since the line density of the target is still decreasing, the energy loss of the incident ion beam is rapidly decreasing as well. While in the beginning of the interaction process the ion beam was completely stopped in the target (energy loss 100 %), at the end of the ion beam pulse the projectile ions loose only about 20% of their initial energy (see Fig. 5.1). This corresponds to a reduction of the target line density around the axis by a factor of 3 or more within a few hundred nanoseconds. The density wave, induced by the heavy ion heating is rapidly moving outwards in radial direction from the heated region inside the target, forming a low density "channel" around the axis. This happends long before any significant expansion of the target matter can be detected by other means, such as optical
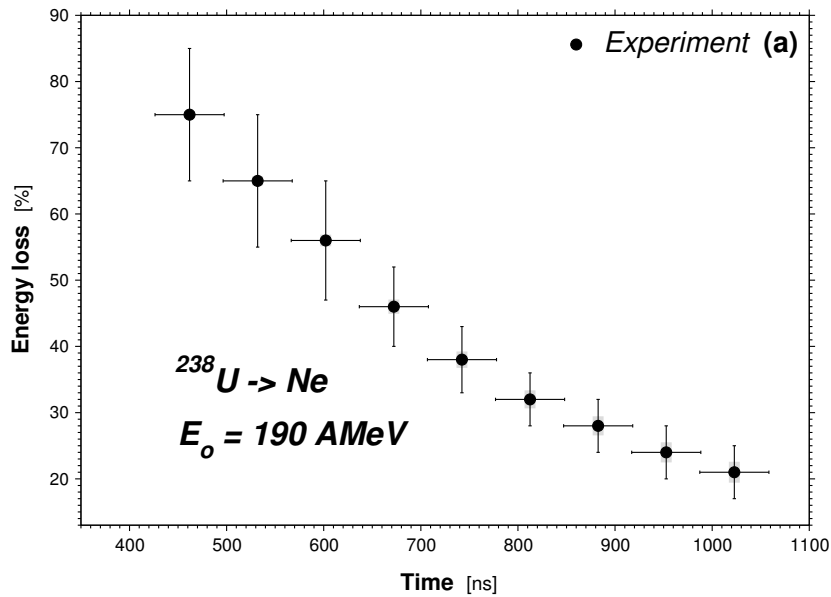
Figure 5.1: Measured ELD of a 190 AMeV ^{238}**U** beam interacting with solid **Ne** target (see Table 5.1(a), p. 64).

diagnostics.

The ELD data processing for the SBP energy loss spectrometer has been described in detail in sec. 4.2. Relatively large error bars of the measured data in the experiment (a) (Fig. 5.1) are mainly due to the shot-to-shot fluctuations of the beam intensity. Higher intensity of the beam leads to a more efficient heating of the target and, in turn, to a faster hydrodynamic response of the target matter. Therefore the ions start escaping the target earlier and the energy loss of the ion beam decreases faster. The steeper the ELD curve is, the larger is the influence of the shot-to-shot beam intensity fluctuations. It is most pronounced for the case when an intense beam is initially stopped in the target.

Since the range of heavy ions in the SBP spectrometer scintillator becomes very small for small energies, the measurement error is larger for smaller ion energies (bigger energy losses). In fact, for ^{238}**U** projectiles the ion energies below about 20 AMeV cannot be precisely measured with the SBP spectrometer.

According to the performed computer simulations of the experiment (a) (sec. 5.2) the maximum specific energy, deposited by the beam in the target was about 1.6 kJ/g. The maximum temperature and pressure induced in the target matter was 1800 K (0.15 eV) and 1.1 GPa, respectively.

In the experiments (b) and (c), Table 5.1, the solid **Ne** cryogenic target has been irradiated by ^{238}**U** beams of higher initial energies, 253 AMeV and 307 AMeV, respectively. In these cases the range of the ions is larger than the target length (8 mm) and the beam is escaping from the rear surface of the target from the beginning (Fig. 5.2), losing about 67 % and 44 % of the initial energy in cases (b) and (c), respectively. However, due to the limited dynamic range of the SBP spectrometer recording device (streak camera) and a high level of background noise, one cannot obtain reliable data at the very beginning and at the very end of the pulse when intensity of the beam is less than approximately 20 % of its maximum value.

It is important to note that the intensity of ^{238}**U** beam in the experiments (b) and (c) was almost an order of magnitude lower than in the above experiment (a). Therefore the specific energy deposition in the target material was also about five
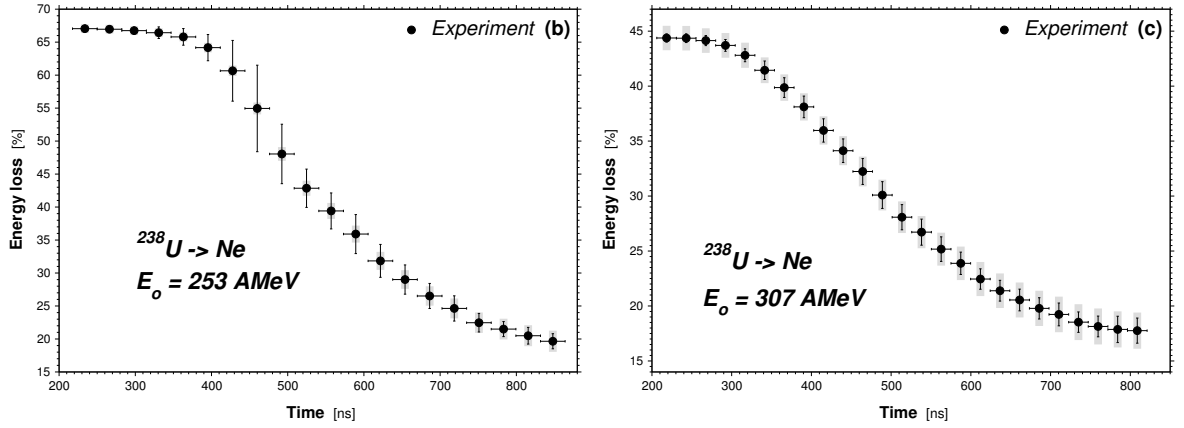
Figure 5.2: Measured ELD of 253 AMeV (left) and 307 AMeV (right) ^{238}U beams interacting with solid **Ne** target. The beam and target initial parameters are given in Table 5.1(b) and Table 5.1(c), p. 64, respectively. Gray bars indicate the systematic error of the measurements.

times smaller than in the first experiment. Nevertheless, the energy loss of the beams and correspondingly, the target line density, has been reduced by factor of 3.4 (case (b)) and 2.5 (case (c)) during the interaction with the target. Another consequence of the lower beam intensity in these experiments is a better focusing. Due to the smaller transverse emittance, the beam spot size in the waist is smaller, less than $500 \, \mu m$ (FWHM). The precision of the measured ELD data in the experiments (b) and (c) is considerably higher compared to the data from experiment (a). There are two main reasons for that.

First, during these two experiment series it was possible to accumulate a better statistics (i. e. to record the data from many shots), measuring the ELD in several dozens of similar beam-target interactions. Therefore every point in Fig. 5.2 assembles about 200 measured data points. This cannot easily be done in every experiment, because the target is destroyed after the interaction and a new target has to be prepared for every following experimental shot.

Second, since the initial energy of the ions is higher and their ranges are larger than the target length, the influence of the shot-to-shot fluctuations of the beam intensity is smaller. This is because the ELD curves of the experiments (b) and (c) are not as steep as in the case (a). In addition to that the fluctuations of the beam intensity itself were also smaller. Moreover, the ions escaping the target with a higher energy have a longer range in the SBP spectrometer scintillator. This increases the accuracy of the measurements, especially in case of the heaviest projectiles. One can also see these effects comparing the cases (b) and (c) in Fig. 5.2: the ELD measurement accuracy in the experiment (b) is somewhat lower than in the experiment (c), corresponding to the higher initial beam energy in the latter case. The beam-target configurations where the beam is not completely stopped in the target are preferable because it allows for a more precise comparison with simulations (see sec. 5.2 below). In such a case the accuracy in determining the initial ion energy on the target can also be verified. In fact, the level of statistical error achieved in the experiments (b) and (c) which is indicated by gray bars in Fig. 5.2 is already of the same order as the estimated systematic error due to the range-energy calibration of the ELD data (see sec.4.2.2 and sec. 4.3.2).

5.1.3 Experiments (d) – (f): ^{86}Kr, ^{40}Ar and ^{18}O beams interacting with solid Xe, Ne and D$_2$ targets

In the following experiments very intense, with more than 10^{10} ions/pulse beams of lighter projectiles, ^{86}**Kr** and ^{40}**Ar** have been used to investigate the ELD of intense heavy ion beams in solid matter (Tab. 5.1(d) and 5.1(e)). Since the energy loss of a projectile in the target scales approximately as Z^2, where Z is the atomic number of the projectile, the energy deposition by ^{86}**Kr** and ^{40}**Ar** beams is much less than that by a uranium beam of the same intensity and initial energy. In order to achieve higher values of the energy deposition one can use target materials with higher density. Therefore solid **Xe** has been chosen as the target material for these experiments, because a solid **Xe** target has a density which is approximately 2.3 times higher than the density of solid **Ne**. In the experiment (d) the beam of 280 AMeV, ^{86}**Kr** was loosing initially about 35 % of its energy in the 8 mm solid **Xe** target, while in the experiment (e) for 291 AMeV, ^{40}**Ar** beam this value is about 16.5 %. However, the total energy of the ^{40}**Ar** beam in the experiment (e) was about 2.2 times larger than that of the ^{86}**Kr** beam due to a higher intensity of the beam (see Tab. 5.1). Therefore in both experiments these intense beams deposited about the same specific energy in solid **Xe** material.
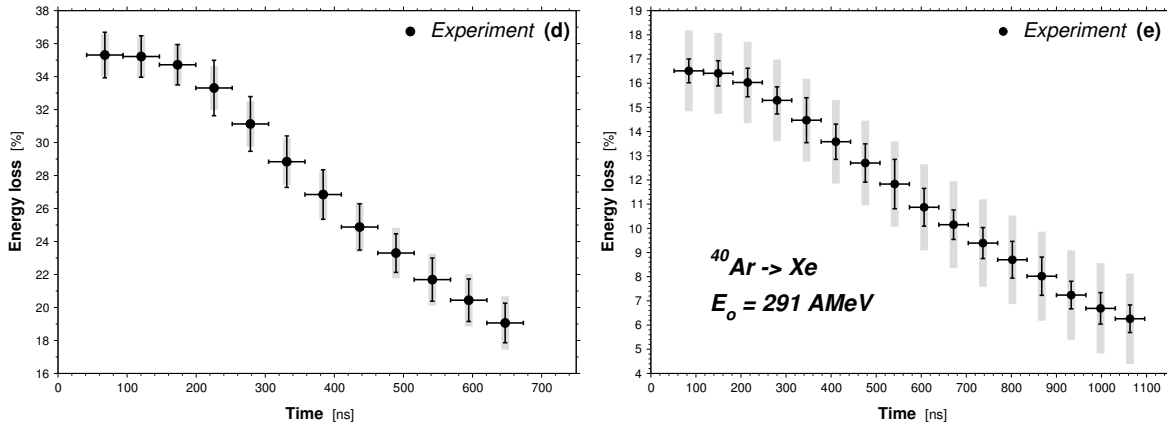

Figure 5.3: Measured ELD of 280 AMeV ^{86}**Kr** (left) and 291 AMeV ^{40}**Ar** (right) ion beams interacting with solid **Xe** targets. The beam and target initial parameters are given in Table 5.1(d) and Table 5.1(e), p. 64, respectively. Gray bars indicate the level of systematic error.

The results of the ELD measurements obtained during the experiments (d) and (e) are presented in Fig. 5.3. In the beginning of the heating process the energy loss of the projectiles stays almost constant, indicating that the target density does not change significantly from the initial solid density value. After about 150 ns, the energy loss of the projectiles starts to decrease rapidly. By end of the heating time the energy loss is more than two times smaller than in the beginning in both experiments. While in the experiment (d) the SBP spectrometer with plastic scintillator has been used, the ELD measurements in the experiment (f) have been done with the liquid scintillator setup (see sec. 4.1). It is seen that both variants of the spectrometer allow one to obtain accurate ELD data.

Finally, the interaction of an intense ^{18}**O** beam with different target materials has been studied (Table 5.1(f)). In spite of the high intensity of the beam (2×10^{10} particles/pulse), the energy loss of 194 AMeV ^{18}**O** ions is small even for solid **Xe**

target due to the small atomic number of the projectiles. Moreover, the total energy of the beam was also about an order of magnitude smaller than in the previous experiment (e) with **Ar** beam (see Tab. 5.1). Therefore one cannot expect a fast hydrodynamic response of the target material to the ion beam heating in this case.
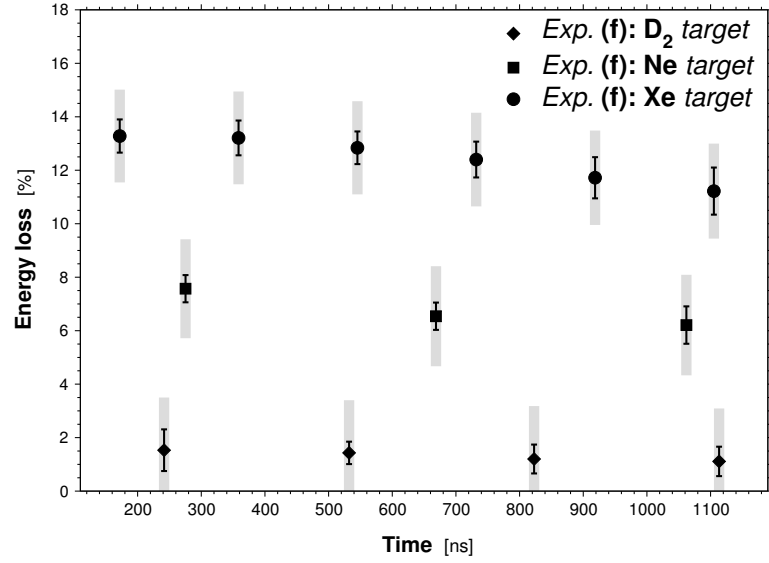

Figure 5.4: Measured ELD of a 194 AMeV ^{18}**O** beam interacting with solid **Xe**, **Ne** and **D$_2$** targets (see Table 5.1(f), p. 64).

The ELD data measured in this experiment are plotted in Fig. 5.4. The energy loss of the same ^{18}**O** beam interacting with solid **Xe**, **Ne** and **D$_2$** targets has been recorded. It is seen that the time dependence of the energy loss is very weak due to a small specific energy deposited by the beam in the targets. Nonetheless, the ELD information for different target materials have been detected by the SBP spectrometer. The energy loss values in the beginning of the heating process are in good agreement with calculations made using the SRIM stopping data for the cold target materials. The small number of the experimental data points for **Ne** and **D$_2$** targets (Fig. 5.4) are due to a limited amount of data collected during these experiments. However, since the ELD curves are rather flat and the statistical error bars are smaller than the estimated values of the systematic error, the resolution of these measurements is also sufficient.

5.2 Numerical modeling of ELD experiments

5.2.1 Full-scale 2D hydrodynamic simulations of the beam-target interaction phenomena

After the first ELD measurements were carried out (see sec. 5.1) it was not clear how to explain such an unexpectedly fast reduction in target density which took place within a few hundred nanoseconds during the irradiation. In order to interpret the experiments, detailed numerical simulations were performed using a sophisticated two-dimensional hydrodynamic code called BIG2 [For96].

The BIG2 code allows to perform simulations of the hydrodynamic phenomena in the ion-beam heated target matter for axial-symmetric or plane geometries. Realistic ion beam energy deposition model, especially developed for this kind of experiments [Shu02], is incorporated into the code. In this model a particular spatial

configuration of the beam, time shape of the beam intensity, beam-target stopping power model which is the cold stopping data calculated by SRIM [Zie96] in this case and momentary distribution of the target density are taken into account and the internal energy of the target matter is accordingly advanced at every time step during the calculations. An elaborate calculation scheme based on solving the hydrodynamic equations in Eulerian formulation on moving grids allows for good resolution of the hydro-motion processes such as propagation of intense shock waves and large pressure gradients and accounts for the conservation laws. The code also computes and saves the ELD data at every time step in order to provide a possibility for direct quantitative comparison with the experimental results.

It is to be noted, that the maximum temperature induced in the target matter in the present experiments was below 0.2 eV in **Ne** targets and below 0.5 eV in **Xe** (see Tab. 5.1, p. 64), which is too low to cause any noticeable ionization in the target material. Therefore, the stopping of the projectile ions is due to bound electrons only. Thus, the physical model of the stopping power (SRIM code) used in the beam-target simulations is valid.

A correct equation-of-state (EOS) model for the target material is crucial to the accuracy and validity of the simulation results. The EOS describes the thermophysical properties of matter providing relations between main thermodynamical variables, such as $p = p(\rho, T)$ and $\epsilon = \epsilon(\rho, T)$ which close the system of the hydrodynamic equations. The EOS governs the character of the hydrodynamic motion of the matter, determining for example, the increase in pressure p and temperature T of the target material due to the increase in its internal energy ϵ or compressibility and sound velocity (characteristic velocity of hydro-motion) in different parameters regions. Since in present beam-target experiments, initially solid target material passes through different states (solid, liquid, gas) due to the heating by the ion beam and expansion of the target, the EOS model used in the hydrodynamic simulations must cover the entire phase diagram, providing all the details about properties of matter in different phase states and phase transition regions.

In present simulations the SESAME EOS data [Ker83] from the Los Alamos Laboratory, USA for RGS **Ne** and **Xe** RGS materials has been used. In addition to that simulations for the experiments (a), (b) and (c) (Tab. 5.1, p. 64) have been performed using the ChTEOS equation-of-state model for **Ne**. This advanced EOS model was developed [Lom02] at the Institute for Problems in Chemical Physics, Chernogolovka, Russia in order to describe the difference between the ELD experiments and simulations with the SESAME data that was found during this study. The influence of the EOS model on the simulation of the ELD data is discussed in the next section.

An example of the hydrodynamic simulations for the ELD experiment (a) is shown in Fig. 5.5. In this figure two-dimensional distributions of target density, temperature and physical phase state of the target matter are plotted at different times during the irradiation. An intense beam of 190 AMeV, ^{238}**U** projectiles is interacting with initially solid **Ne** target. In the beginning the range of ^{238}**U** ions is smaller then the target length. Therefore the beam in completely stopped and deposits its total energy in the target. The temperature of the target material is increasing due to the heating by the beam and therefore a pressure gradient in radial direction is induced. In addition a shock wave moving forward in axial direction is generated behind the Bragg-peak of the stopped ions (see Fig. 5.5). At 100 ns the temperature of **Ne** in the heated region is above the melting point, a part of
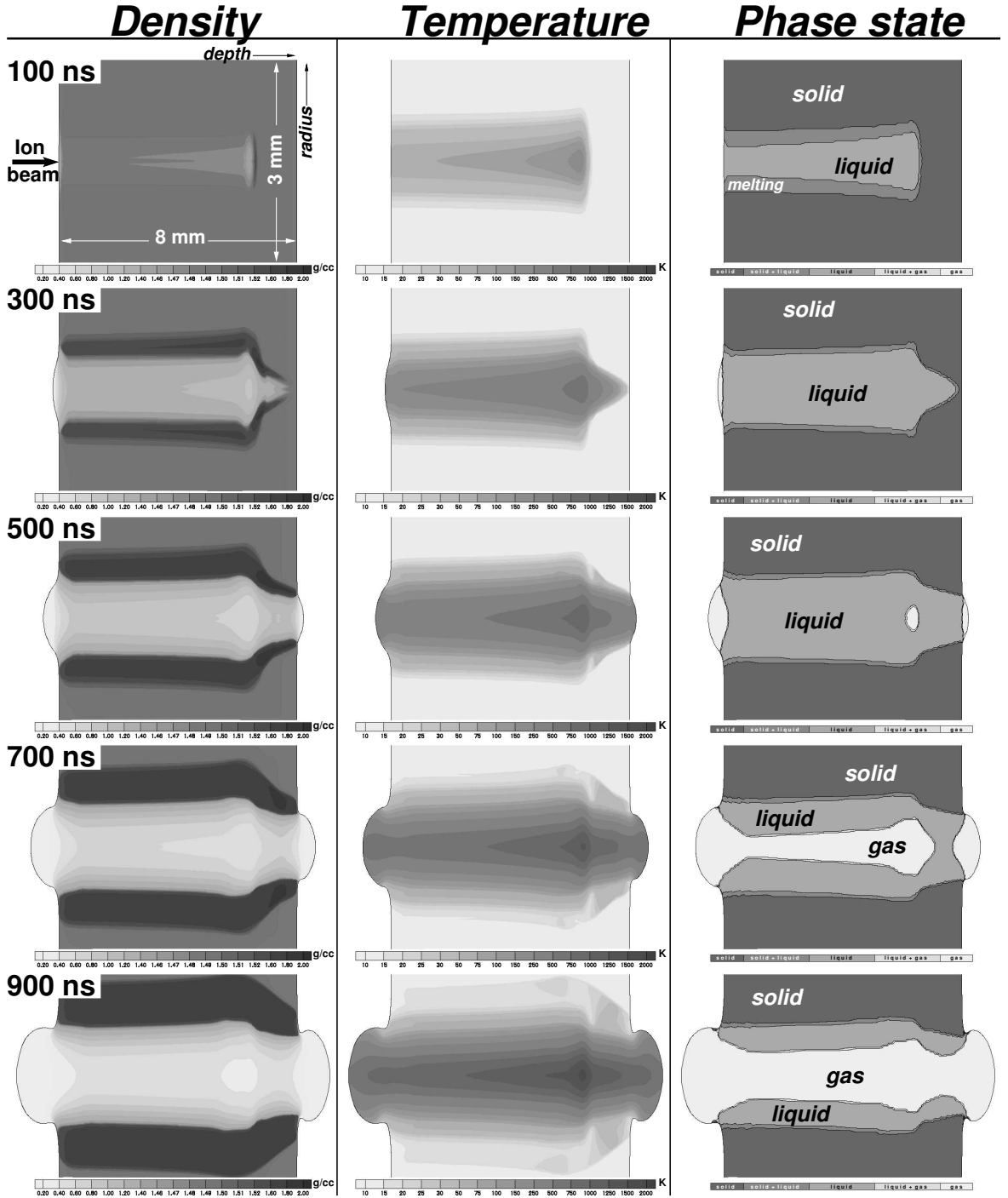
Figure 5.5: Hydrodynamic simulations for the Exp. (a): ^{238}**U** beam interacting with solid **Ne** target (see Table 5.1(a), p. 64). Two-dimensional (radius-depth) distributions of target density, temperature and physical phase state at different time moments during the irradiation are shown. The simulations were performed using the BIG2 code and ChTEOS equation-of-state model.

the target matter is melted and a lower density channel consisting of the liquid material is being formed. At the same time, due to the continuous beam heating an intense density wave of the compressed material penetrates outward in radial direction, driven by the pressure gradient. The melting (two-phase, liquid-solid) front is following the radial density wave. As a result the line target density in the vicinity of the ion beam axis is decreasing and the beam ions can penetrate deeper and deeper into the target. In this way the beam is "boring a hole" in the heated target matter.

Already at about 350 ns from the beginning of the irradiation, the first ions are able to escape from the back surface of the target due to the reduced target density around the axis. However, the temperature of the target material in the interaction region is still increasing and the radial density wave, while moving outward from the axis leaves behind a wider and wider region of melted lower-density liquid matter. At about 500 ns time it is seen (Fig. 5.5) that the temperature and density of the target material are high enough that the second phase transition can take place inside the target. In the area with the highest temperature, near the initial position of the Bragg-peak of the stopped ions, the liquid **Ne** is evaporating and a "gas bubble" is formed inside the liquid material. Due to the further heating and decrease in density the region of evaporated target matter is expanding in axial and radial directions. At about 700–800 ns the evaporated region, developing from inside of the target joins the gas jets of expanding matter, emerging from the front and back surfaces of the target. Finally, at about 900 ns from the beginning of the beam pulse a low-density channel of the gaseous **Ne** is formed around the beam axis. This channel is surrounded by a layer of the liquid material which in turn, is confined by a radially expanding wave of the compressed target matter at super-solid density.
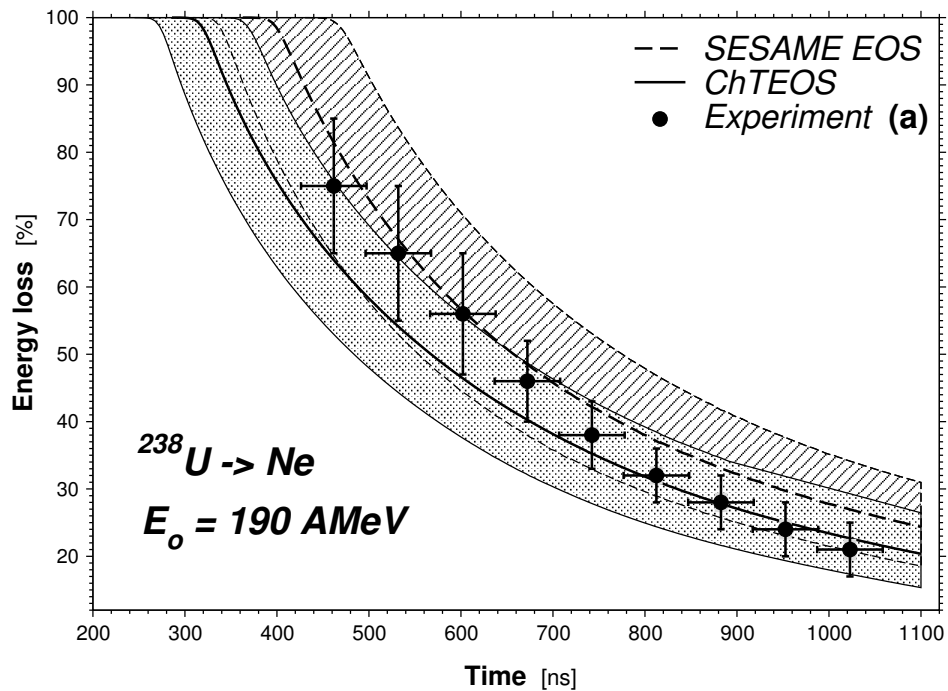

Figure 5.6: Simulations of the ELD experiment: ^{238}**U** beam interacting with solid **Ne** target (see Table 5.1(a), p. 64 and Fig. 5.5, p. 71). Two different EOS models have been used in the simulations: SESAME (dashed lines, dashed area) and ChTEOS (solid lines, dotted area). The description is given in the text.

The evolution of the target line density during the heating by an ion beam is reflected in the energy loss dynamics (ELD) of the projectile ions. During the simulations the ELD data is calculated by the BIG2 code and saved together with the target parameters at every time step. This allows for a direct and quantitative comparison of the simulation results with the performed ELD measurements (see sec. 5.1). A result of such a comparison of the ELD data for the experiment (a) is shown in Fig. 5.6. The initial parameters of the experiment are given in Tab. 5.1(a), p. 64, whereas corresponding two-dimensional images of the calculated target thermophysical properties at different time moments are presented in the Fig. 5.5.

Since at the beginning of the interaction the beam is completely stopped in the target (see the detailed explanations above), no data could be detected by the spectrometer up to about 400 ns. After the ions start to escape from the rear surface of the target, the line density around the beam axis is continuously decreasing and the measured energy of the escaping projectile ions is increasing correspondingly. The energy loss of the ions is therefore decreasing and becoming about 20 % of the initial beam energy at the end of the ion beam pulse.

A large number of simulations for this experiment has been performed, varying the initial parameters such as beam focal spot size and initial beam energy on the target within the measurement accuracy limits as well as employing different EOS models for the target material. The calculated ELD curves for slightly different initial parameters of the experiment form a "confidence corridor" around the average curve for a given equation-of-state model for the target material (Fig. 5.6). The "width" of such corridor depends on the accuracy to which the initial parameters of an experiment are known (beam focusing, initial beam energy and initial target density, Tab. 5.1), rather than on the accuracy of the ELD measurements itself. In Figure 5.6 the corridor with dotted area around the solid line represents the results of the simulations made with ChTEOS equation-of-state model and the dashed corridor is plotted using the SESAME EOS model.

In this particular experiment the ELD data are very sensitive to the accuracy to which the initial parameters are known. This is because the ELD curve is very steep and small fluctuations of the initial beam energy or specific energy deposition shift the time moment when the ions start to escape the target as well as the whole ELD curve significantly. Although the confidence corridors of the calculations made with different EOS models are partly overlapping in this case, the experimental points lie in between the curves calculated using the different EOS. This shows that the results of the sophisticated 2D simulations are in good quantitative agreement (below 10 %) with the experimental data.

Similar hydrodynamic simulations using different EOS models for solid **Ne** have also been carried out for the experiments (b) and (c) (see Tab. 5.1 and Fig. 5.2). An example of such simulations for experiment (b) with the ChTEOS model is presented in Fig. 5.7. In this case the range of the 253 AMeV, ^{238}**U** projectile ions is larger than the target length and the Bragg-peak lays outside the target. Therefore the ion beam deposits its energy almost uniformly along the axis. Due to a much lower beam intensity (the specific energy deposition and maximum temperatures are about five times smaller than in the experiment (a), see Tab. 5.1) the initially solid target material is melted only after about 300–400 ns. However, by this time the target line density on the axis is already decreased by about 10 %. At later times, as in the previously described experiment (a), the radial pressure gradient induced by the ion beam heating drives the compression wave outwards. The melt-
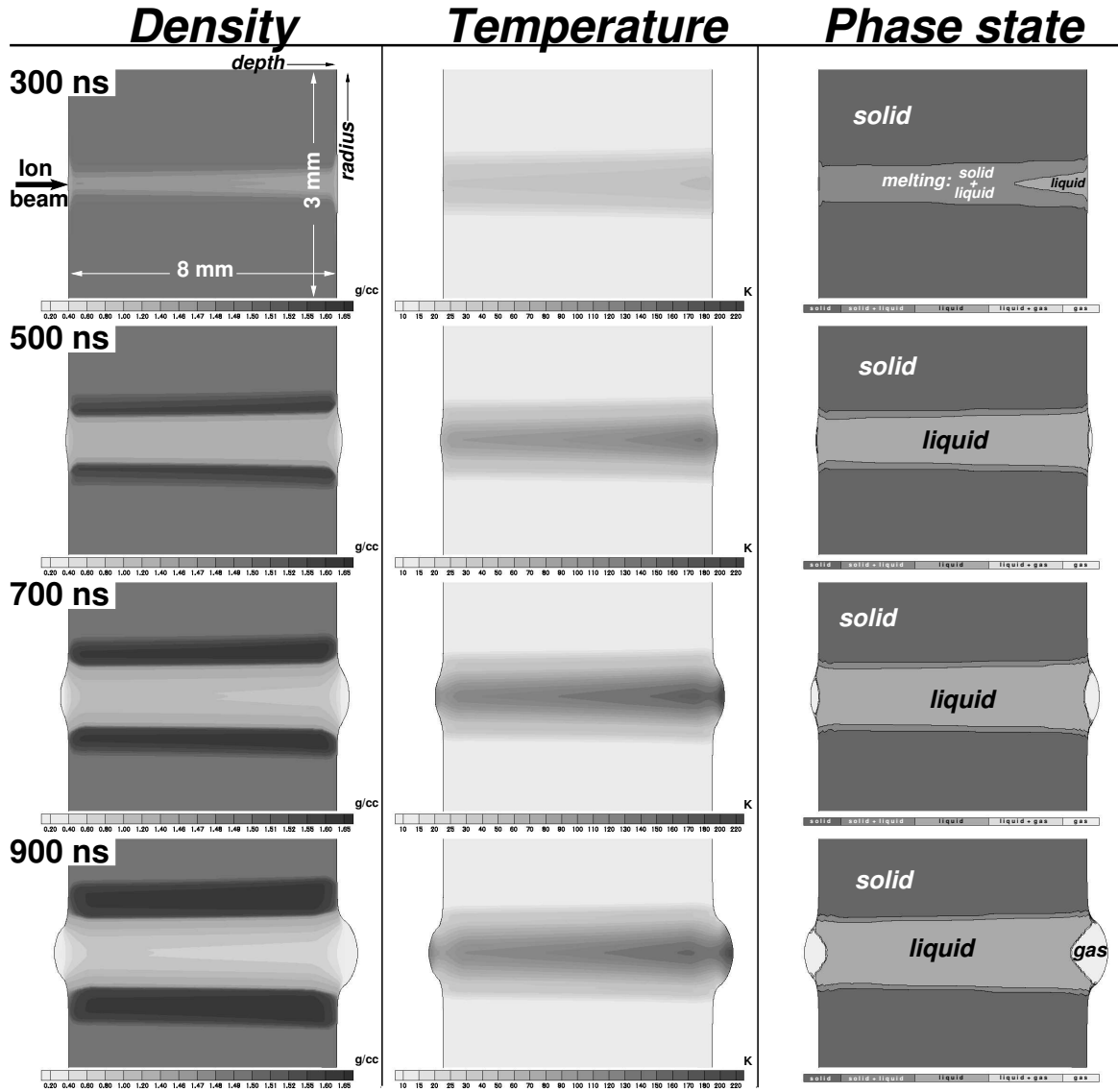
Figure 5.7: Hydrodynamic simulations for the Exp. (b): 253 AMeV, ^{238}**U** beam interacting with solid **Ne** target (see Table 5.1(b), p. 64). Two-dimensional (radius-depth) distributions of target density, temperature and physical phase state are shown at different time moments during the irradiation. The simulations are made using BIG2 hydro-code and ChTEOS equation-of-state model.

ing front follows the radial density wave. As a result a narrow low-density channel filled with liquid **Ne** is formed around the axis. The line density of this, axially uniform channel is continiously decreasing with time and becomes less than 50 % of the initial value at the end of the pulse.
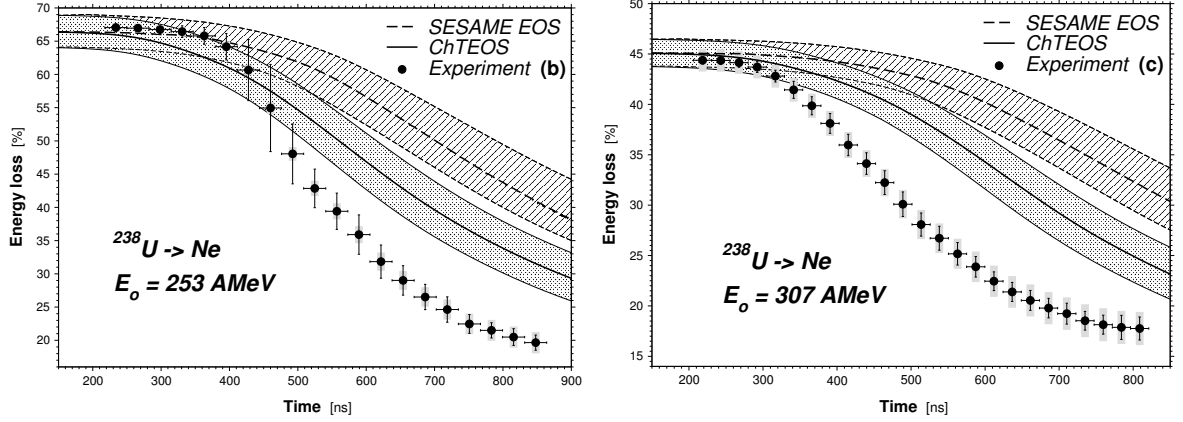

Figure 5.8: Simulations of the ELD experiments (b) and (c): 253 AMeV (left) and 307 AMeV (right) ²³⁸**U** beams interacting with solid **Ne** target. The beam and target initial parameters are given in Table 5.1(b) and Table 5.1(c), p. 64, respectively. See also Fig. 5.7, p. 74. The SESAME (dashed lines, dashed area) and ChTEOS (solid lines, dotted area) EOS models have been used in the simulations.

The results of the ELD simulations for the experiments (b) and (c) are presented in Fig. 5.8 along with the measured data. A large number of calculations has been also performed with two different EOS models, SESAME and ChTEOS and for the different initial parameters such as beam focusing and beam initial energy, varied within the accuracy limits of the experiments (see Tab. 5.1, p. 64). The confidence corridors for the simulations with SESAME and ChTEOS equation-of-state models for **Ne** are indicated by the dashed and dotted areas, respectively. Although there is a significant difference between the simulation results obtained with different EOS models, all the calculated ELD curves deviate from the precision experimental data. The influence of the EOS model on the simulation results in these experiments will be discussed in the following section.

Finally, the simulation results for the performed experiments with **Xe** target are presented in Fig. 5.9. The ELD curves for intense ⁸⁶**Kr** and ⁴⁰**Ar** ion beams interacting with solid **Xe** target are calculated taking into account the accuracy limits of the initial parameters in these experiments. Only the SESAME wide-range EOS data is available for **Xe** material at the moment. In case of the experiment (d) (see Fig. 5.9, left) the width of the confidence corridor is defined mostly by the accuracy to which the initial beam energy on the target is known (see Tab. 5.1). In contrast to this, for the case (e) (Fig. 5.9, right), the inaccuracy of the beam focal spot size measurement enlarges the "error bar" of the calculations (the dashed area in the plot) towards the end of the irradiation time.

In spite of the relatively large width of the simulations confidence corridors in both cases and a visible systematic deviation in the measured ELD dependency compared with the calculated curves, one has to admit that there is a good agreement between the simulations and the experimental data. This is probably due to a better accuracy of the EOS model (SESAME) for **Xe** in the parameters range of the experiments. The maximum temperature of the **Xe** target was considerably higher
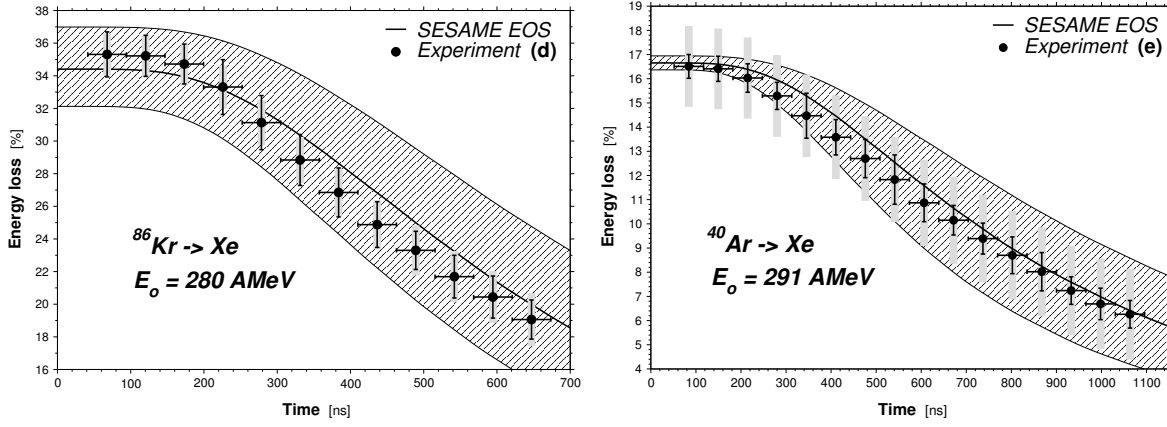
Figure 5.9: Simulations of the ELD experiments (d) and (e): 280 AMeV, ^{86}**Kr** (left) and 291 AMeV ^{40}**Ar** (right) ion beams interacting with solid **Xe** targets. The simulations are performed with BIG2 hydrodynamic code and SESAME EOS data. The beam and target initial parameters are given in Table 5.1(d) and Table 5.1(e), p. 64, respectively.

(above 4000 K) than in the experiments with solid **Ne**. Therefore, the influence of the matter properties (melting and evaporation phase transition regions, etc.) at low temperatures might influence ELD curve compared to the experiments with solid **Ne** targets to a less degree.

5.2.2 Influence of EOS model

The equation of state (EOS) describes fundamental thermophysical properties of matter and therefore, detailed knowledge about the EOS of the target material is crucial for understanding the interaction phenomena between an intense heavy ion beam and a target. In the present beam-target experiments, the initially solid target material passes through different states due to the heating by the ion beam and expansion of the target. For example, the target matter can be melted, forming a hot liquid, evaporated to an expanding rarefied vapor. Propagation of shock or sound waves in the hot target material can induce states with super-solid density and high pressure. If sufficient energy is deposited into the target, more exotic states such as strongly coupled plasma can be generated in the vicinity of the liquid-vapor equilibrium curve and the critical point. Therefore the EOS model used in the hydrodynamic simulations must cover the entire phase diagram, providing all the details about properties of matter in different phase states and phase transition regions.

The SESAME EOS tables [Ker83] are the most widely used EOS data for calculations for many different materials. However, it is known that the SESAME data have a limited accuracy in certain regions of pressure, density and temperature parameter space, especially in low temperature and high density regime. This regime is of particular relevance to the heavy ion beam interaction experiments discussed in this work. A detailed analysis of the SESAME data for RGS materials and in particular — for solid **Ne** has shown that this model does not account correctly for the thermophysical properties of the rare-gas solid (RGS) targets at low-temperature solid and liquid states as well as for the melting and evaporation phase transition regions. The SESAME tables for RGS **Ne** contains only a few data points for temperatures below 500 K. Although the EOS properties of the RGS materials in a wide

parameter range are not fully investigated experimentally like for example, properties of many metals, there is a large amount of experimental data available on the thermophysical parameters of RGS in solid state as well as for the melting phase transition (see [Kle77] and references therein). However, the SESAME tables for RGS are probably based on a simplified model only which is focused on high temperature states such as hot gas and plasma. It does not cover the low temperature regime ($T < 0.2\,eV$) in a satisfactory manner. In addition to that, the values of the thermodynamic derivatives, such as the sound velocity, taken from the SESAME data for RGS materials have a high level of nonphysical noise and often deviate from known experimental data.

In order to enhance the accuracy of the hydrodynamical simulations of the phenomena observed in the beam-target interaction experiments with RGS targets, in particular, to interpret the ELD data that have been measured in the present study, a new advanced EOS model for **Ne** has been developed at the Institute for Problems in Chemical Physics (IPCP), Chernogolovka, Russia [Lom02]. This EOS called ChTEOS (*Chergnogolovka's Temperature Equation Of State*) is a semi-empirical description of the material thermophysical properties, in which a number of coefficients in analytic expressions are used to fit the available experimental and theoretical data. The ChTEOS multi-phase (solid, liquid, gas, plasma) wide-range EOS model asymptotically approaches the results of theories based on "first-principles" while describing the intermediate regions satisfactorily. A detailed description of this model, initially developed for metals and successfully used in simulations, is given in the book [Bus93].

The ChTEOS Mie-Grüneisen-type EOS for **Ne** accounts for the cold lattice contribution and thermal contribution of atoms and electrons to the free energy thermodynamic potential. The thermal atoms contribution is different for solid and liquid states. In the ChTEOS the full Debye model for crystal [Lan76] is employed in order to adequately account for low-temperature states in solid **Ne** while the cold lattice curve ($p_c(V)$ at $T = 0\,K$) agrees with calculations based on Thomas-Fermi model at high levels of compression. The EOS provides a correct description of phase boundaries — melting and evaporation in a wide range of pressures. In addition to that the effects of the first and second ionization are also taken into account to describe the high-pressure high-temperature plasma states. In the ChTEOS tables temperature T and specific volume $V = 1/\rho$ are chosen as independent variables. The experimental $P - V$ compressibility isotherm for solid **Ne** [Hem89], melting and evaporation parameters [Kle77] as well as crystallization pressure at room temperature [Kle77] are used to fit the parameters of the EOS model.

The EOS model for the target material which is used in hydrodynamic simulations influences the results of such simulations significantly. For example, the compressibility of matter given by the EOS governs the characteristic velocities of propagation of hydrodynamic disturbances (sound velocity), determines amplitudes of shock and density waves and the time scale of the processes. The relation between internal energy, temperature and pressure defines the "effectiveness" of the heavy ion beam heating for a given target material, i. e. how much of the energy deposited by the beam will be finally converted to the kinetic energy of hydrodynamic motion and defines the temperature and pressure in the target matter. As an example, in Tab. 5.2 the thermodynamic parameters calculated for different materials at normal (solid) density are shown, assuming that a specific energy of $\mathcal{E} = 1\,kJ/g$ is induced in matter. It is also very important to take into account a
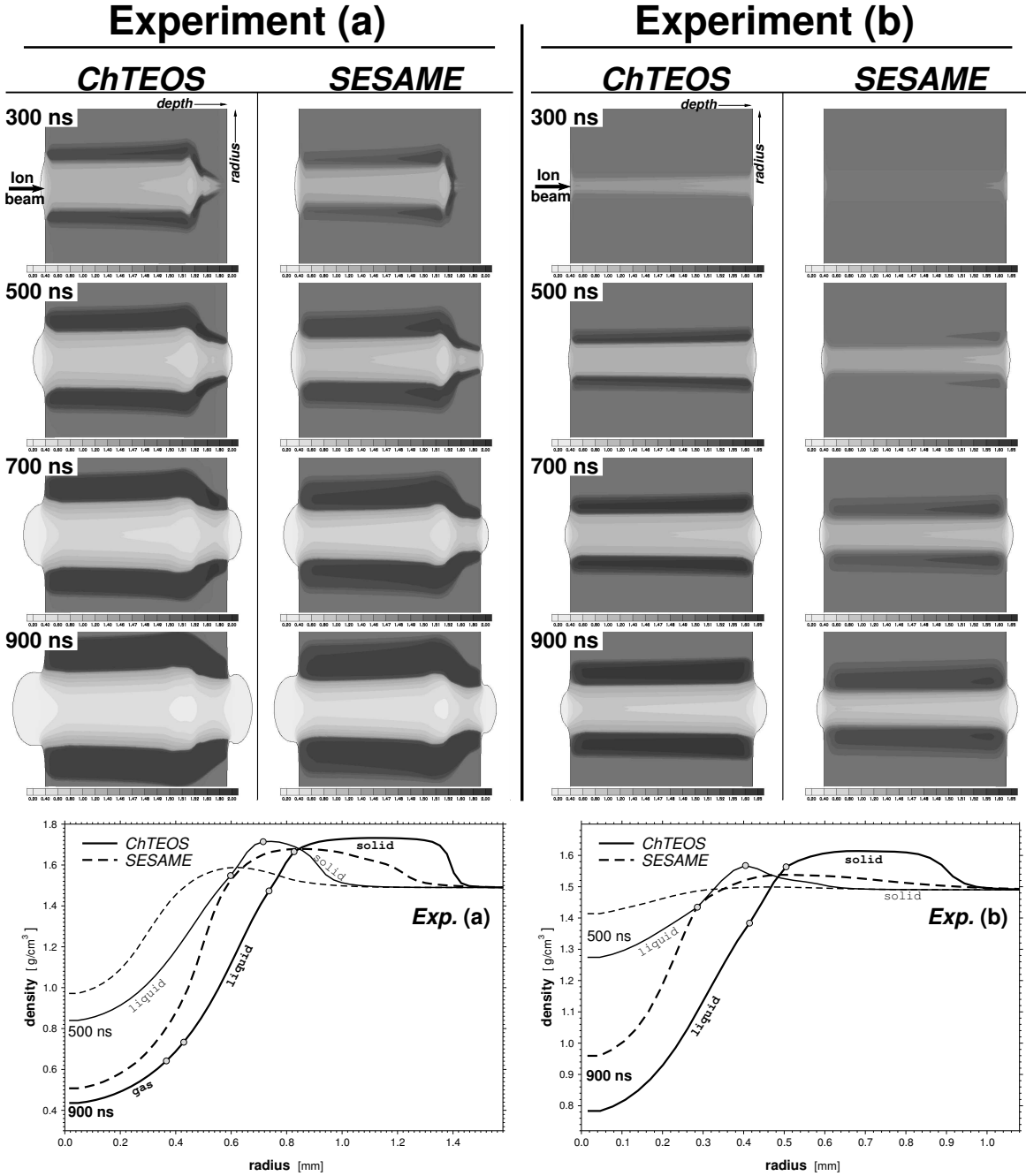
Figure 5.10: Hydrodynamic simulations for the Exp. (a) and (b) with different EOS models (see Table 5.1(a), Table 5.1(b) p. 64 for description of the experiments and Fig. 5.5, p. 71, Fig. 5.7, p. 74, Fig. 5.6, p. 72 and Fig. 5.8, p. 75 for the details of the target parameters and the corresponding ELD data). Two-dimensional target density distributions are shown at different time moments for simulations made using SESAME and ChTEOS equation-of-state models (top). Radial profiles of the target density in the middle of the target at different time moments (500 ns and 900 ns), taken from the upper figures, are plotted in the bottom. The phase transition boundaries are marked on the radial density profiles with empty circles (for the calculations with ChTEOS tables, solid lines).

large difference in all the thermophysical properties of matter at different states, such as solid, liquid, gas and plasma as well as at two-phase states between the phase transition boundaries. All the above mentioned properties of the target material must be incorporated in an EOS model in order to obtain a correct theoretical description of the interaction phenomena.

Table 5.2: Thermodynamic parameters of different materials assuming that a specific internal energy of $\mathcal{E} = 1\,\text{kJ/g}$ is induced in matter at normal (solid) density, $\rho = \rho_0$. The values have been calculated using ChTEOS data [Lom02].

		Ne	Al	Fe	Pb
Temperature (T),	K	1090	13600	2440	6890
Pressure (P),	GPa	2.4	6.79	22.3	14
Entropy (S),	J/g/K	4.27	1.42	0.94	0.47
Sound velocity (c_0),	km/s	2.46	5.75	5.32	2.63

In Figure 5.10 the time development of the target density distribution during irradiation, calculated with ChTEOS and SESAME EOS data is presented. The simulations are done for the experiments (a) and (b) (see Tab. 5.1, p. 64). The corresponding ELD dependencies, calculated for the same cases have been shown earlier, in Fig. 5.6, p. 72 and Fig. 5.8, p. 75, respectively. In all these simulations with the BIG2 code, the beam and target parameters were set exactly the same and only the EOS model for **Ne** has been varied. One can see that the EOS data used for the simulations changes the results considerably. Due to a higher sound velocity in **Ne** given by ChTEOS tables, the amplitude of the density wave in solid, surrounding the expanding axial channel is higher and the radial density distributions differ from the calculations with SESAME data (see Fig. 5.10). The correct description of the phase transition boundaries and properties of the solid and hot liquid **Ne** changes the shape of the density profiles significantly. The ChTEOS data also gives higher values of induced pressure in the target material.

The overall expansion of the target matter in the heated region is faster when the ChTEOS model for **Ne** is used in the simulations. This is seen by comparing the values of density on the axis at different times (Fig. 5.10). In turn, the evolution of the line density on the axis is directly reflected in the energy loss of the projectile ions, i. e. in the ELD data (see Fig. 5.6 and Fig. 5.8). The difference in the ELD values (and correspondingly, in the evolution of the line density), which is given only by the difference in the EOS model, is as large as 20–25 % in the above described simulations. The influence of the EOS can be even more pronounced for special beam-target interaction geometries, for example in the case when a regime of radial implosion of the target matter is induced. This can be done for example, by employing *hollow targets* which have a hole or a lower density region along the axis [Var98c].

As it is seen, ELD measurements can be employed for the verification of EOS models for the target material, since the difference in the ELD data caused by an EOS is larger than the typical error bar of the ELD measurements in many cases. However, for this purpose not only the ELD values itself but also the initial beam and target parameters have to be measured precisely. These include the spatial distribution of the ion beam in the target (focal spot size and beam envelop)

and initial energy of the beam. For example, in the first ELD experiment (Fig. 5.6, p. 72), the inaccuracy in measuring these parameters led to a partial overlapping of the confidence corridors for the ELD simulations made with different EOS models, whereas the difference between the mean ELD curves calculated with different EOS data is rather large (about 20 %). Nevertheless, one cannot fully destinguish between the EOS models in this case and the experimental ELD data can be in principle explained by the both models.

The situation is different for the experiments (b) and (c), Fig. 5.8, p. 75. In these cases the influence of the EOS data on the ELD curve is also large (up to 20 %) but the precision to what the focal spot size and initial beam energy are measured is better, about 5 % and 2 %, respectively. Therefore, the confidence corridors for the simulations with different EOS models do not overlap when the experimental inaccuracy in the inital parameters is taken into account. The ELD data itself has also been measured to a much better precision than in the experiment (a). However, although in these cases the ChTEOS model gives a better agreement with the experiment than the SESAME tables, both calculated theoretical ELD curves deviate from the measured data.

An idea to explain the difference between the ELD data measured in the experiments (b) and (c) and the corresponding simulations, even those made using the advanced EOS model (ChTEOS) was an influence of the elastic effects in solid **Ne**. The two-dimensional hydrodynamic code BIG2 which was used in the simulations does not account for elastic effects. However, it is known that the properties of solids and, in particular, the speed of propagation of acoustic compression waves differ in cases of small and large deformations [Zel67].

In case of sufficiently high loads (on the order of a kilobar), the solid material loses its firmness and becomes similar to a fluid (*plastic state*). The elastic properties of the material are then isotropic and characterized by a single quantity, the compressibility $\kappa = (1/\rho)(\partial\rho/\partial P)_S$ which determines the speed of propagation of acoustic compression waves, or the *(plastic) sound velocity*

$$c_0^2 = \left(\frac{\partial P}{\partial \rho}\right)_s = \frac{1}{\rho\kappa}. \tag{5.1}$$

This is true only in the case when the pressure is high and the effects connected with strength of solids and the existence of shear strains and stresses are not important. If the loads are small, then it becomes necessary to take into account the elastic properties of solid that distinguish it from a liquid and some quantities (such as pressure) become direction-dependent (*elastic state*). This has an appreciable effect on the character of dynamic processes and in particular it is found that acoustic waves can propagate in solid matter with different speeds.

The propagation speed of weak acoustic (longitudinal) waves in elastic solids is given by the following expression [Zel67]:

$$c_l^2 = c_0^2 + \frac{E'}{\rho}, \tag{5.2}$$

where E' depends on the Young modulus and Poisson ratio of the material. The *elastic sound velocity* c_l, i. e. the propagation speed of longitudinal waves in an infinite elastic medium, is always greater than the plastic sound velocity c_0. For example, for polycrystalline **Ne** $c_0 = 850\,\mathrm{m/s}$ and $c_l = 1120\,\mathrm{m/s}$ at $T \approx 10\,\mathrm{K}$ [Bal71], which gives about 30 % difference. The transition from elastic to plastic state accures when the pressure in the solid material becomes greater than a cerain critical

value, P_{cr}. The value of the critical compressive load $P_{cr} = \frac{1-\sigma}{1-2\sigma}2\sigma_{cr}$ is defined by the Poisson ratio σ and the critical shear stress σ_{cr} and is typically about 0.2 kbar. In case of very high pressures, the propagation speed of compression waves (*shock wave velocity*) depends on the wave strength and is always greater than c_0 or close to this value.

During the beam-target interaction in the experiments (b) and (c), the compression wave penetrates outward in radial direction from the heated axial channel into the solid material. The pressure in solid which is induced due to the compression as well as the propagation speed depends on the state of the solid **Ne**, elastic or plastic. Neglecting the elastic-plastic transition in solid may lead to an underestimation of the propagation speed of the compression wave and result in wrong radial density and pressure distributions.
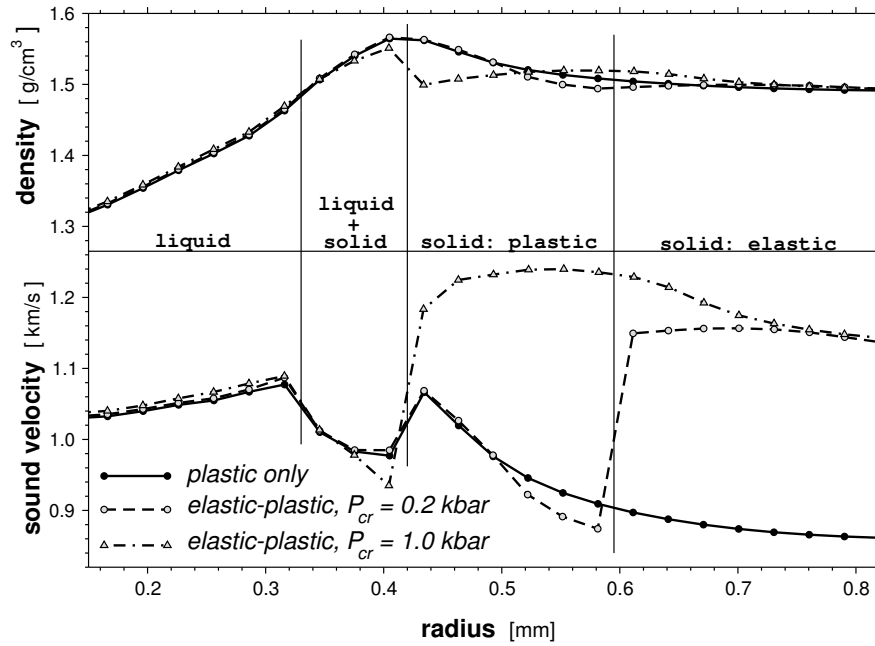

Figure 5.11: Model simulations for exp. (a) including elastic-plastic transition in solid **Ne**. Radial profiles ($t = 500\,ns$) of target density (top) and sound velocity (bottom) are shown for different assumptions about elastic-plastic transition: neglecting the transition (solid curves), for $P_{cr} = 0.2\,\mathrm{kbar}$ (dashed curves) and for $P_{cr} = 1\,\mathrm{kbar}$ (dashed-dotted curves).

In order to perform model simulations taking into account the elastic-plastic transition and to estimate its influence on the ELD data, the BIG2 code has been modified [Shu02]. The correct description of the elastic effects in a hydrodynamic code is a very difficult three-dimensional problem since the elastic properties may depend also on the preparation of a sample, defects, details and history of the applied load. A simplified scheme has been employed in the BIG2, taking advantage of the geometry of the hydro-motion in these particular cases. Since in the experiments (b) and (c) the heavy ion beam was heating the targets almost uniformly along the axis, the material moves only in radial direction, $v_z \ll v_r$ and the problem is almost one-dimensional. Therefore, the elastic-plastic transition has been introduced by increasing the sound velocity in solid **Ne** and, correspondingly, the pressure from a value given by the EOS data $c_0(T, \rho)$ by a factor of c_l/c_0, if $P < P_{cr}$. The experimental values of elastic sound velocity c_l for polycrystalline **Ne** have been taken from the work [Bal71]. Although this treatment of the elastic properties is

simplified, it allows to estimate at least the order of magnitude of the effects.

An example of such model simulations for the experiment (b) are presented in Fig. 5.11. There the density profiles in the middle of the target at $t = 500\,ns$ are plotted for different calculations: one where the elastic-plastic transition in solid **Ne** is neglected and the others where this effect is taken into account in the above described way, assuming $P_{cr} = 0.2\,\mathrm{kbar}$ and $P_{cr} = 1\,\mathrm{kbar}$. The performed simulations have demonstrated that accounting for the elastic-plastic transition effect changes the density profiles of the compression wave in a solid considerably. For instance, new features such as an "elastic precursor" running away from the "main" compression wave are now visible on the radial density profiles and the amplitude of the density wave and the pressure induced in solid target material differ as well.

However, the corresponding calculations of the ELD values have shown that the influence of the elastic properties of solid **Ne** on the evolution of the target line density *on the axis* is negligible (below 0.5 %) for experiments (b) and (c). Therefore, accounting for the elastic-plastic transition cannot explain the difference between the measured ELD data and the simulations in this case.
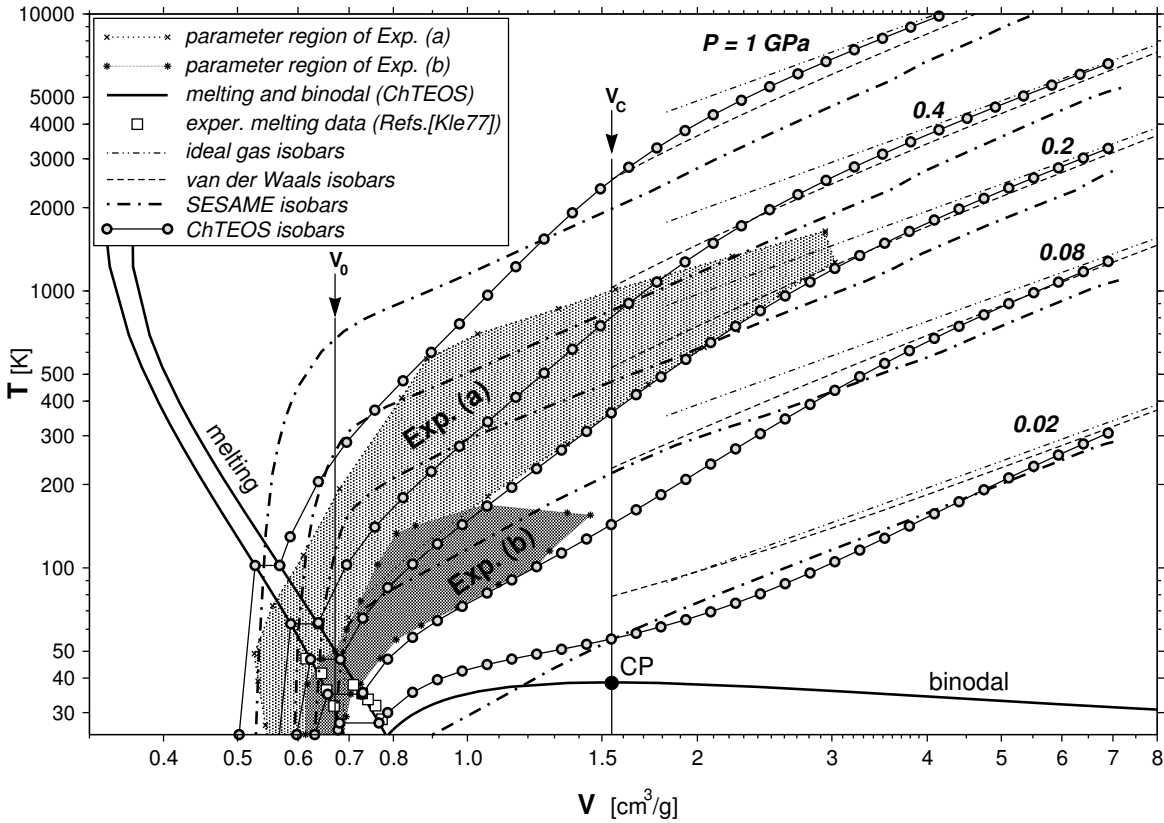
Figure 5.12: $T - V$ phase diagram of **Ne** in the parameter region of the ELD experiments. Isobars for $P = 10\,\mathrm{kbar}\,(1\,\mathrm{GPa})$, $4\,\mathrm{kbar}$, $2\,\mathrm{kbar}$, $800\,\mathrm{bar}$ and $200\,\mathrm{bar}$ calculated using different EOS models (ideal gas, van der Waals, SESAME and ChTEOS) are shown. Melting and evaporation (binodal) curves defining two phase solid-liquid and liquid-gas regions, respectively, were calculated using ChTEOS model. CP is the critical point of **Ne**, $V_0 = 1/\rho_0$ is the normal volume of solid **Ne** at $T = 10\,K$ and V_c is the critical volume.

It is to be concluded that the explanation for this difference is the influence of the EOS model on the simulation results. In the experiments (b) and (c) the beam

intensity was much lower than in the experiment (a) and the specific energy deposition in the target material was by more than a factor of five smaller. In turn, according to the simulations, the target matter has been heated only to about 200 K maximum temperature while in the experiment (a) this value was more than 1700 K. Consequently, in the experiments (b) and (c) the target material was at liquid state during most of the interaction time and much lower pressures have been induced in the target (see Fig. 5.12), whereas in case (a) the target material was heated up to expanded gaseous states. Therefore, the influence of the thermophysical properties of liquid **Ne** and the melting region is more pronounced in the simulations carried out for the experiments (b) and (c) rather than for the case (a).

It is seen from Fig. 5.12 that for the dense gaseous **Ne** ($V \geqslant 1 - 1.5\,V_c$) in the pressure range of the present ELD experiments ($1 - 10\,\text{kbar}$) the isobars calculated with both ChTEOS and SESAME EOS models already approach those of the ideal or van der Waals gas. This can explain the fact that it is possible to describe the ELD data measured in experiment (a) (Fig. 5.6, p. 72) using both EOS models. However, the slope of the isobars calculated with SESAME follows that of the ideal gas down to very small volumes (high densities) of the order of the solid density. Moreover, the SESAME model does not account for the melting transition, as it can be clearly seen from Fig. 5.12. Therefore, one can expect that the simulations performed using the ChTEOS model will be more accurate than those with the SESAME EOS for the parameter region of the experiments (b) and (c) (see Fig. 5.8, p. 75).

In the ChTEOS model the data on the properties of solid **Ne** and the parameters of the melting curve obtained in static experiments was used to fit the empirical coefficients [Lom02]. However, most of these experimental data has been obtained in 60s and 70s (Refs. [Kle77]), while only a limited amount of work on measuring thermodynamic properties of **Ne** has been reported during the past two decades. The properties of hot liquid neon have not been studied at all. Furthermore, for a detailed description of the thermodynamic properties, the conditions under which cryo-crystal were grown have to be taken into account. For example, the melting curve depends considerably on whether the sample is a single crystal or a polycrystalline material.

In conclusion to this section, it is to be noted that the measured ELD data is useful for verifying different EOS models. This work has clearly demonstrated that the SESAME EOS data in case of solid **Ne** is inaccurate in the high density, low temperature region. The new ChTEOS model that includes a correct description of the phase transitions and is based on advanced theories for solid and liquid phases shows a better agreement with the present ELD experimental results. However, there still is a noticeable difference between the experimental data and the simulation results for **Ne**. This discrepancy is due to the fact that the new EOS model is still not accurate enough because of the limited experimental data on the thermodynamic properties of RGS materials that is available. It is therefore concluded that more experimental work needs to be done that will allow to improve the wide-range multi-phase ChTEOS model for RGS materials. The present work already stimulated further experimental and theoretical research in this field, where the future ELD experiments will also make a significant contribution.

6 Conclusions and suggestions for future experiments

6.1 Main results of the work

The main results of the study described in this thesis are outlined below:

1. A novel diagnostic technique for high energy density (HED) matter experiments has been proposed, where one uses the same intense heavy ion beam that heats the target to provide information about the physical state of the interior of the target. This is accomplished by measuring the *energy loss dynamics* (ELD) of the beam emerging from the back surface of the target.

2. A new method for measuring the energy of intense energetic heavy ion beams with high temporal resolution has been developed. In this method, the effects of complete slowing down of a beam in the bulk of a fast scintillating material are employed. A collimated part of the beam around the axis is stopped after the target in a fast plastic or liquid scintillator. The specific luminescence profile along the axis of the scintillator (Bragg-curve), recorded by a fast electronic streak-camera is used to obtain the energy spectrum of the beam at every moment in time during the interaction.

3. Based on the above method, a new small and elegant time-resolving spectrometer, which is called *scintillating Bragg-peak* (SBP) spectrometer, has been designed and constructed. The SBP spectrometer allows for wide-range precision measurements of the heavy-ion beam energy spectra with temporal resolution. A special mathematical model to process the ELD data obtained with this instrument has been developed and realized in a new computer code. The analysis of accuracy limitations and main sources of measurement errors for ELD experiments with the SBP spectrometer has been conducted as well.

4. For the first time, the energy loss dynamics of intense heavy ion beams interacting with dense matter has been observed experimentally. The ELD measurements of intense ($10^8 - 10^{10}$ particles/pulse) focused beams of ^{238}**U**, ^{86}**Kr**, ^{40}**Ar** and ^{18}**O** ions with 150–350 MeV/u initial energy interacting with rare-gas solid (RGS) targets, such as solid **Ne** and solid **Xe** have been carried out. A significant reduction in the ion beam energy loss during the interaction due to rapid hydrodynamic response of the ion-beam heated target matter has been recorded. The SBP spectrometer has been used in these experiments.

5. In order to interpret the experimentally observed physical phenomena, theoretical calculations of the ELD of intense heavy ion beams interacting with initially solid targets have been performed. For the simulations a sophisticated two-dimensional hydrodynamic code BIG-2 (IPCP-Chernogolovka and GSI-Darmstadt) has been employed as well as different equation-of-state (EOS)

models for the RGS target materials: the SESAME EOS (Los Alamos, USA) and ChTEOS (Chernogolovka, Russia). The latter EOS model has been recently developed at IPCP-Chernogolovka to explain the results of the ELD experiments. A comparison of the simulation results and the measured ELD data is also provided. In particular, it has been demonstrated that the SESAME EOS data for RGS materials has a limited accuracy in certain parameter regimes, where a correct description of the phase transitions is essential. The simulations performed with the ChTEOS model are in better agreement with the experimental ELD data for solid **Ne** targets.

6. In the framework of the present study, experimental and theoretical investigations on a new generation of high-current pulsed magnetic lenses have also been carried out. These devices can be an attractive alternative to conventional steel-dominated or superconducting magnets as to be used in construction of a magnetic spectrometer for the ELD measurements as well as for other applications. For example, strong final focusing systems and ion-beam transport lines. In this study, the construction of the high-current cylindrical strip-line magnets has been optimized. In particular, an enhancement of the strength and quality of the magnetic field by means of multilayer conductor arrangements has been achieved. A new type of high-current pulsed iron-free dipole, called "Helmholtz-loops dipole" has also been proposed. The ion-optical properties and magnetic field distribution of different pulsed high-current dipole and quadrupole magnets have been studied in experiments with heavy ion beams.

7. For a precise description of the ion-optical properties of high-current pulsed magnetic lenses, a new computer code called VARDIOS has been developed. The code is based on the novel Differential Algebra computational technique and is able to calculate transfer maps of systems containing pulsed magnets up to an arbitrary order, taking into account realistic three-dimensional magnetic field distributions as well as all the fringe field effects. Simulations of the ion-optical properties of various pulsed magnetic lenses have been performed with this code. These simulations have demonstrated that the transfer matrix elements of pulsed lenses can differ significantly from those of conventional iron-dominated magnets, especially for high-order aberrations.

6.2   Future applications of ELD diagnostics

6.2.1   ELD diagnostics with imaging beam

In order to achieve the most efficient heating of a target and the highest energy density in matter with a heavy ion beam, the beam pulse should be as short as possible. In this case, the line density of the target and, correspondingly, the energy deposition in the target material do not change significantly during the interaction time, in contrast to the present experiments with long beam pulses (see chap. 5). On the other hand, if the target density does not change during the interaction the ELD diagnostics cannot be applied, except for the cases when the target is heated to high temperatures, so that the plasma stopping effects (sec. 2.1.2) become important.
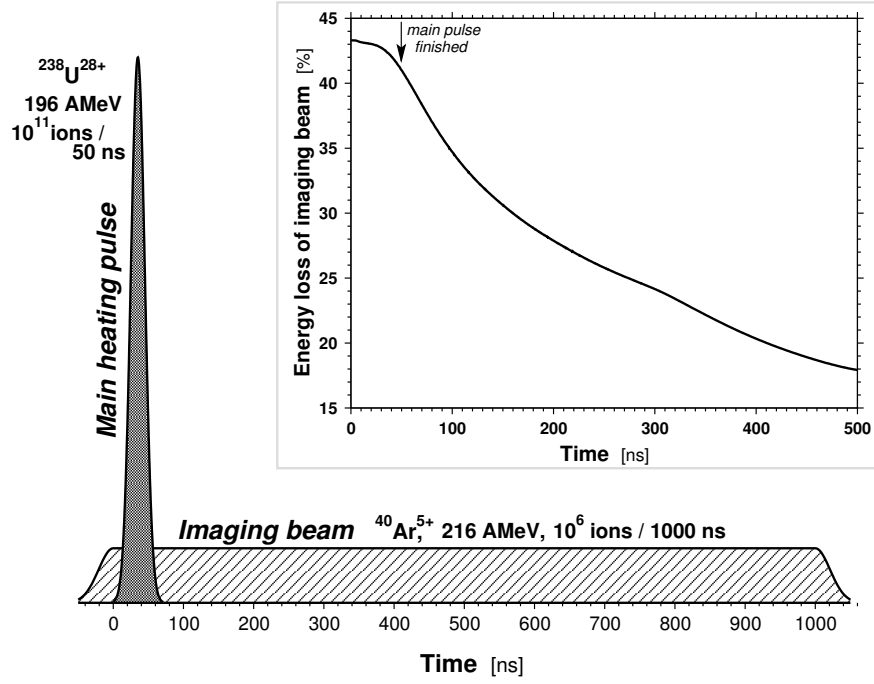
Figure 6.1: ELD diagnostics using an additional imaging beam (see explanations in the text).

To overcome this difficulty, it has been proposed [Spi99, Var00a] to irradiate the target with two beams of different ion species. One, a high intensity bunched beam of some heavy element like uranium is used to efficiently heat the target material. The second beam of a lighter element that has a long pulse length and possibly a higher initial energy, is employed only for the diagnostic purposes (an *imaging beam*, see Fig. 6.1). One can therefore use the ELD diagnostic technique in such experiments without reducing the efficiency of heating due to a longer beam pulse.

Later it has also been proposed that these two beams of different ion species can be accelerated simultaneously in the existing SIS-18 synchrotron and transported for the HED matter experiments [Hof01, Tah02c]. This can be done if the magnetic rigidity (Eq. (2.18)) of both beams is equal over the whole acceleration cycle. Furthermore, the difference in revolution frequency must be large enough that the individual beams can be handled by the two separate RF acceleration systems available at SIS-18, without interference. The two ion beams may be produced in parallel by two different ion sources, accelerated by the UNILAC linear accelerator and injected into SIS-18 synchrotron using the fast repetitive multi-turn injection scheme (see sec. 3.1.1). After the acceleration and debunching, the preparation of the main heating beam pulse can be performed using both RF acceleration systems and eventually third RF system for compression. Finally both, the compressed heating pulse and the coasting diagnostic beam can be fast extracted from the synchrotron and delivered to the experimental area.

A possible configuration of such a beam pair can be, for example, an intense $(2 \cdot 10^{11}$ particles in a $50\,\mathrm{ns}$ pulse) beam of $^{238}\mathrm{U}^{28+}$ ions with 196 AMeV energy and a long (about $1\,\mu s$) accompanying low intensity $^{40}\mathrm{Ar}^{5+}$, 216 AMeV imaging beam. Both the beams have magnetic rigidity of about 18 Tm. This idea is illustrated in Fig. 6.1 along with the ELD calculations for the imaging beam [Tah02b, Tah02c]. In these calculations a lead target of a 4 mm length was considered. Since the range of uranium ions with the energy of 196 AMeV in lead is much shorter than

the length of the target, the main heating beam is completely stopped during the interaction time and deposits its entire energy in the target. However, the imaging **Ar** ions, although losing initially about 43 % of the energy in the target matter, can penetrate through and escape the target. Therefore, measuring the ELD of the imaging beam would provide important information about the physical state of the interior of the target during and after the heating. At the moment such "embedded-beams" acceleration scheme is being worked out in detail at GSI.

6.2.2 Implosion of hollow targets for verification of EOS model

It has been shown in sec. 5.2.2 that the hydrodynamic processes in a beam-heated target matter and consequently the energy loss dynamics of incident beam during the interaction depend significantly on the equation of state (EOS) of the target material. Thus the experimental ELD data can be used for verification of the theoretical EOS models. It is therefore important to find beam-target configurations for which the influence of the EOS model on the ELD dependence is most pronounced. In order to find such systems for future HED matter experiments, extensive computer simulations with the two-dimensional hydrodynamic code BIG-2 have been performed, varying parameters of the beam and target geometry [Var98c].
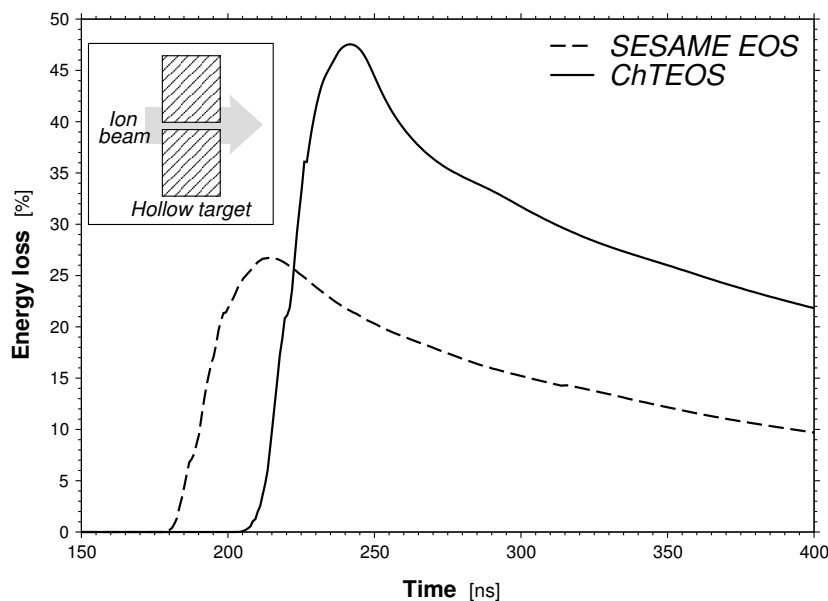

Figure 6.2: ELD of intense uranium beam in a hollow lead target. A 500 ns [238]**U** beam of 10^{10} particles with initial energy of 300 AMeV, focused in a 0.5 mm (FWHM) spot interacts with a lead target that has a 0.5 mm hole along the axis. The simulations [Tah02a] have been performed using two different EOS models for lead: SESAME EOS and ChTEOS.

As a result of this study it has been found that the ELD of a beam interacting with a *hollow target* (i. e. a target that has a hole, cavity or a low-density region around the axis) differs considerably depending on the EOS model used in the simulations. Let us assume a target that has a small hole along the axis (Fig. 6.2). Initially, the beam ions from the vicinity of the axis are passing through the hole and do not lose their energy in the target. However, the transverse distribution of the beam intensity has always a Gaussian shape. Therefore, if the diameter of the hole is smaller or comparable to the beam focal spot size (FWHM), the "wings" of the beam intensity distribution heat the target material around the walls of the

hole. The heated target matter which is melted and possibly evaporated, starts to implode on the axis. After a certain time, this material reaches the axis causing a sharp increase in the beam energy loss along the axis (see Fig. 6.2). At the stagnation of such cylindrical implosion, the density of the hot target material on the axis can be of the same order of magnitude as the solid density and the ELD curve has its maximum. At later times, due to overall hydrodynamic expansion of the heated target matter the energy loss on the axis decreases again.

The ELD dependencies for this beam-target configuration, calculated using different EOS models for the target material are presented in Fig. 6.2 [Tah02a]. It is seen that the calculated ELD of the beam changes dramatically depending on the theoretical EOS model employed in the simulations. In the example plotted in Fig. 6.2, the time moments of the implosion differ by about 13 %, whereas the values of the energy loss differ by about 60 % at stagnation and by more than 75 % during the following expansion. Such a big difference may be caused by the limited accuracy of the SESAME EOS data in the low temperature, high density regime, where a correct description for the phase transitions is essential. Subsequently, different implosion velocities and different compressibilities of the material, suggested by different EOS models cause a large difference in the target density at the stagnation time, resulting in different ELD dependencies.

An idea for EOS measurements, somewhat similar to the above described using of the hollow targets has been recently suggested by I. Iosilevski [Ios02]. It has been proposed to use porous target material heated by intense heavy ion beams. The phenomenon called "isobaric heating" occurs in this case: the target material condensed in the grains is being heated by the beam and expands into the surrounding pores. Until the pores are completely filled with the target matter, the average pressure in the target does not increase and no macroscopic expansion of the material occurs. However, at later times the pressure in the target rapidly increases and the target expands. By measuring the time moment of this expansion one can obtain useful information about the EOS of the target material, provided the initial beam and target parameters (specific energy deposition, average size and uniformity of the grains and pores) are known precisely. The ELD diagnostic technique can also be used in such experiments. While the target material is expanding into the pores, the line target density does not change, whereas when the pours are filled and overall hydrodynamic expansion of the target begins, the energy loss of the beam ions will rapidly decrease as well.

6.2.3   HI-HEX EOS measurement technique and ELD diagnostics

Recently, a novel technique for EOS studies with intense heavy ion beams called HI-HEX (*Heavy Ion beam Heating and EXpansion*) has been proposed [Hof02]. Due to the unique feature of the heavy-ion beam energy deposition process (volume character of heating) it is possible to generate high entropy states in matter without necessity of shock compression. Such high entropy states cover wide region of the phase diagram including hot liquid, evaporation region with the critical point and strongly coupled plasmas. Previously, these regions could only be accessed by using most powerful shock wave generators like underground nuclear explosions and powerful lasers. However, most of the data obtained in these experiments refers only to a narrow parameter range in the vicinity of the shock adiabats (principal and porous Hugoniots).

In the HI-HEX technique, exotic high entropy states in matter are generated using quasi-isochoric heating by intense heavy ion beam without necessity of any shocks. During the following isentropic expansion, the heated target material would pass through different above mentioned states, depending on the initial value of the entropy. The range of thermodynamic parameters that can be covered in a single HI-HEX experiment is extremely wide: six orders of magnitude in pressure and four orders of magnitude in density [Hof02].

The ELD diagnostics is an indispensable tool for the HI-HEX experiments. By measuring the ELD of the ion beam during the heating phase, one can obtain precisely the value of entropy induced by the beam in the target matter. Furthermore, employing the above imaging beam technique (sec. 6.2.1), it is possible to diagnose the target density and stopping power during the following isentropic expansion phase.

A   An analytic approximation for stopping power

In the paper [Sne99] an analytic approximation function for the stopping power has been proposed. Although the authors have used it for light ions ($Z \leq 8$) in the (1–100) AMeV energy region and for target material similar to plastic scintillator, it has been found extremely useful for heavier ions and higher energies as well. This approximation has been used in several steps of the data analysis for SBP spectrometer (see sec. 4.2) with a great success.

According to [Sne99] the stopping power can be described by the following equation:

$$-\frac{dE}{dx} \equiv \mathcal{S}(E) = \frac{Z^2}{A} \frac{\kappa}{1+\mu} \frac{1}{(E+\epsilon)^\mu} \,, \tag{A.1}$$

where E is the particle kinetic energy, Z and A are the atomic number and mass of the projectile, κ, μ and ϵ are the fitting parameters. The units are chosen as follows:

$$[E] = AMeV, \quad [x] = mm, \quad [\mathcal{S}] = AMeV/mm. \tag{A.2}$$

Comparing this equation with the Bethe-Bloch formula (see sec. 2.1.1) shows that the logarithmic term ("Coulomb logarithm"), inconvenient for computations, is now incorporated in the parameters μ and ϵ. The parameter κ contains the material-dependent properties such as electron density. The expression Eq. (A.1) should be fitted to calculated or measured stopping data for a certain ion-target combination in specific energy region via the three fitting parameters: κ, μ and ϵ.

A sharp cut-off approximation for the stopping power is assumed here:

$$\mathcal{S}(E) \equiv 0, \qquad E < E_{\min}, \tag{A.3}$$

where

$$\mathcal{S}(E_{\min}) = \frac{Z^2}{A} \frac{\kappa}{1+\mu} \frac{1}{\epsilon^\mu} \approx \mathcal{S}^{\max}. \tag{A.4}$$

The value of $E_{\min}$ which corresponds to the maximum value of the stopping power $\mathcal{S}^{\max}$ can be incorporated in parameter ϵ and therefore in the following equations the value of energy, E will be counted from zero. This cut-off approximation implies that the Eq. (A.1) can be used only for $E \geq E_{\min}$.

Once an analytic expression Eq. (A.1) for the stopping power $\mathcal{S}(E)$ is available, one can easily obtain analytic expressions for all the related quantities such as particle range $\mathcal{R}(E)$, stopping power along the particle trajectory in the medium (*Bragg-curve*) $\mathcal{S}(E, x)$ and others.

The energy of an ion penetrated the distance x in the medium can be obtained by integrating Eq. (A.1):

$$E(x, E_0) = \left[(E_0 + \epsilon)^{\mu+1} - \frac{Z^2}{A} \kappa x \right]^{\frac{1}{\mu+1}} - \epsilon \,, \tag{A.5}$$

where E_0 is initial energy. The expression for the Bragg-curve can therefore be derived as

$$S(E_0, x) = \frac{dE(x)}{dx} = \frac{Z^2}{A}\frac{\kappa}{\mu+1}\left[(E_0 + \epsilon)^{\mu+1} - \frac{Z^2}{A}\kappa x\right]^{-\frac{\mu}{\mu+1}}. \tag{A.6}$$

The range of an ion in medium $\mathcal{R}$ is related to its initial energy E_0 as

$$\mathcal{R}(E_0) = \int_0^{E_0} S^{-1}(E, x)\,dE = \frac{A}{Z^2}\frac{1}{\kappa}\left[(E_0 + \epsilon)^{\mu+1} - \epsilon^{\mu+1}\right]. \tag{A.7}$$

It is also convenient to have expressions where the range $\mathcal{R}$ is used as an independent variable instead of initial energy E_0:

$$E(x, \mathcal{R}) = \left[\frac{Z^2}{A}\kappa(\mathcal{R} - x) + \epsilon^{\mu+1}\right]^{\frac{1}{\mu+1}} - \epsilon, \qquad x \leq \mathcal{R}, \tag{A.8}$$

and

$$S(\mathcal{R}, x) = \frac{Z^2}{A}\frac{\kappa}{\mu+1}\left[\frac{Z^2}{A}\kappa(\mathcal{R} - x) + \epsilon^{\mu+1}\right]^{-\frac{\mu}{\mu+1}}, \qquad x \leq \mathcal{R}. \tag{A.9}$$

Finally, the relation (A.7) between range and energy can be written in *relative variables*, $\tilde{\mathcal{R}} = \mathcal{R}/\mathcal{R}_0$ and $\tilde{E} = E/E_0$, where $\mathcal{R}_0 = \mathcal{R}(E_0)$:

$$\tilde{\mathcal{R}}(\tilde{E}) = \frac{\left(\tilde{E} + \frac{\epsilon}{E_0}\right)^{\mu+1} - \left(\frac{\epsilon}{E_0}\right)^{\mu+1}}{\left(1 + \frac{\epsilon}{E_0}\right)^{\mu+1} - \left(\frac{\epsilon}{E_0}\right)^{\mu+1}}. \tag{A.10}$$

If the value of $\frac{\epsilon}{E_0}$ is small, the range-energy relation written in relative variables approaches a simple power dependence $\tilde{\mathcal{R}}(\tilde{E}) = (\tilde{E})^{\mu+1}$.
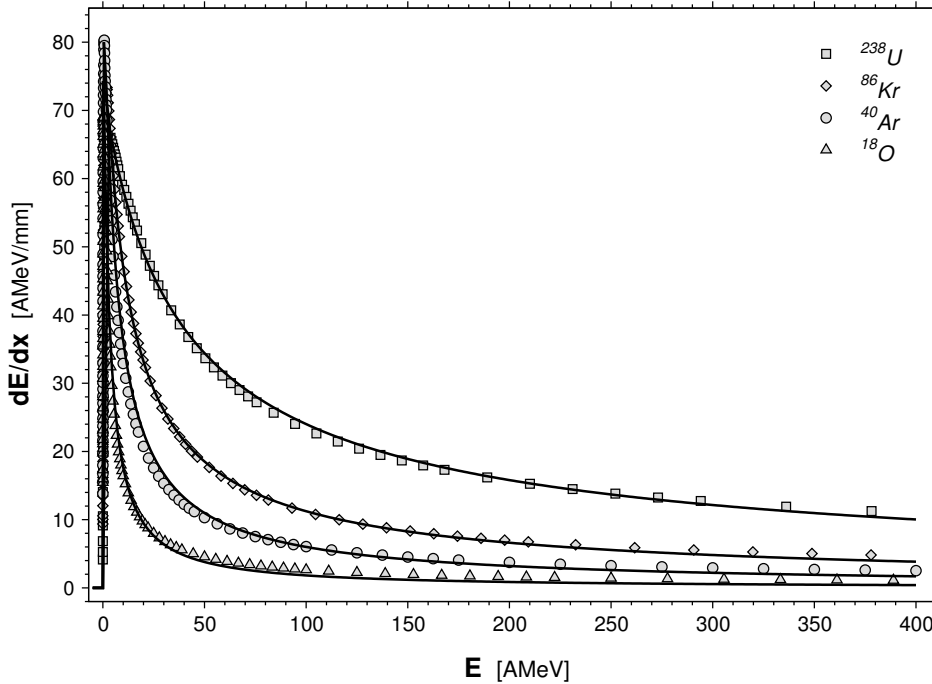

Figure A.1: Fitting of the stopping power of plastic scintillator by analytic approximation on a wide energy region for different ions.

An example how Eq. (A.1) resembles the stopping data in a wide energy region is shown in Fig. A.1. The approximation formula has been fitted to the stopping power values of the plastic scintillator (see Tab. 4.1, p. 44) calculated by the SRIM code [Zie96]. The figure presents the curves for different ion species. The accuracy of the data representation by the approximating formula is not worse than 5 % over the entire energy region from E_{min} (0.2–3.5 AMeV) to about 400 AMeV for all the ions.
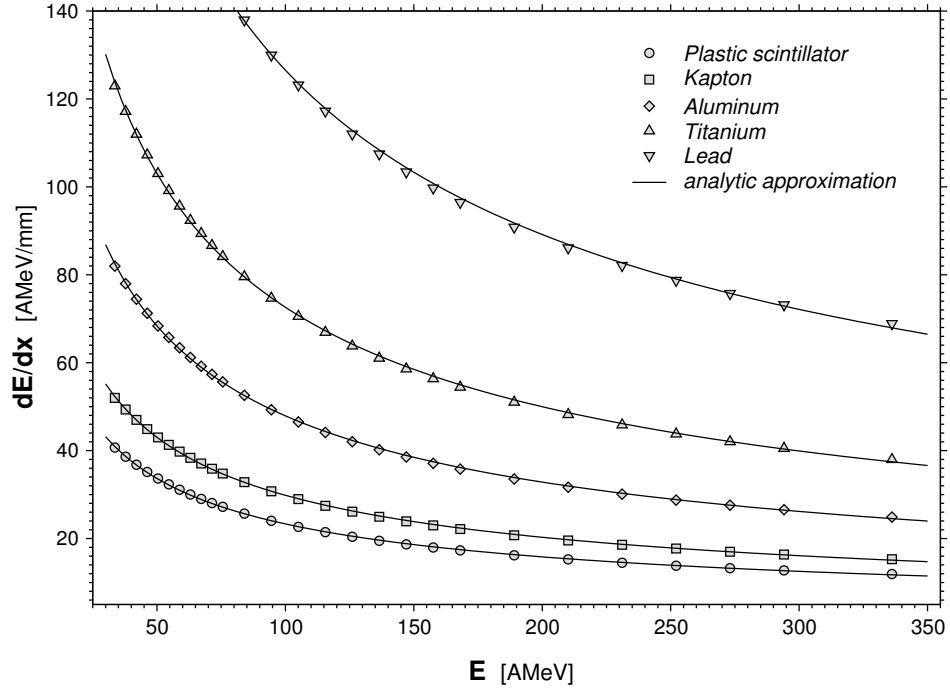

Figure A.2: Stopping power of different materials to ^{238}U ions calculated by SRIM code and represented by analytic approximation.

A much better accuracy of fitting can be obtained for a specific energy region. Such an approximation can then be used, for example for precision calculation of the energy loss in a material of given thickness with Eq. (A.5). The use of a simple analytic expression for such estimations is indispensable when it is necessary to calculate repetitively the energy loss of a beam penetrating through a set of vacuum windows or degraders made of different materials and with different thicknesses. Moreover, the analytic expression can be used to find the thickness of the medium if the initial and final energies of the ions are known. In Fig. A.2 the approximation of the stopping data for different materials to ^{238}U ions is shown. The accuracy of the data representation by the analytic expression is better than 1 % over the energy region of 30–350 AMeV. Although the accuracy of fitting can be even better for a narrower energy regions or for different ion species, it is not needed due to the limited precision of the original stopping data calculated with the SRIM code.

The quality of the representation of the stopping data by the analytic approximation can be verified on range calculations. When the parameters in Eq. (A.1) are fitted to a given stopping power data, the range as a function of energy can be obtained from Eq. (A.7). These values can be compared with an independent range-energy data. For example, in the SRIM code which is a semi-empirical model, the calculation of ranges is made not only by integrating the stopping power but the ranges are also adjusted to experimental data. The correct representation of the range-energy relation is important because it is used as a calibration function in
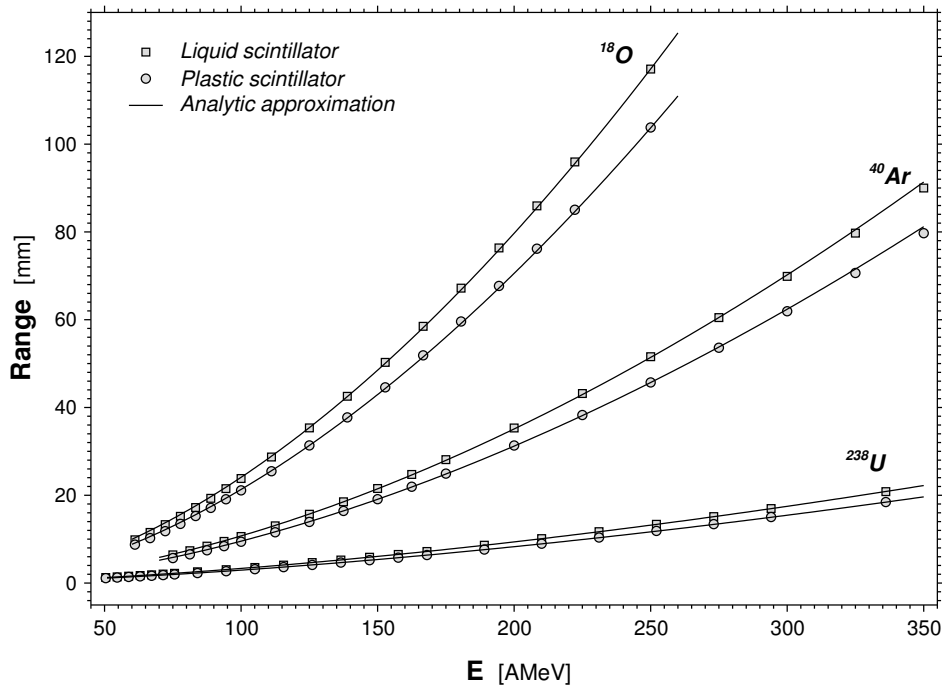
Figure A.3: Ranges of different ions in organic scintillators calculated by SRIM code and represented by analytic approximation.

the SBP spectrometer data processing (sec. 4.2). An example of the range-energy relation reproduced by the analytic expression (A.7) is given in Fig. A.3. The plot presents the ranges of different ions in organic scintillators calculated with SRIM code and by Eq. (A.7). The accuracy of the analytic representation compared with the original SRIM data is better than 0.5–1 % for all the plotted curves.

Bibliography

[Ahl80] S. P. Ahlen (1980), Rev. Mod. Phys. **52** p. 121.

[Ahl82] S. P. Ahlen (1982), Phys. Rev. A **25** p. 1856.

[Ahl83] S.P. Ahlen and G. Tarlé (1983), Phys. Rev. Lett. **50** p. 1110.

[Ant82] J.M. Anthony and W.A. Landford (1982), Phys. Rev. A **25** p. 1868.

[ATI]   *Description of the ATIMA code.*
         URL http://www-aix.gsi.de/ scheid/ATIMA1.html

[Bal71] R. Balzer, D.S. Kupperman and R.O. Simmons (1971), Phys. Rev. B **4** p. 3636.

[Bar63] W.H. Barkas, N.J. Dyer and H.H Heckmann (1963), Phys. Rev. Lett. **11** p. 26.

[Bas84] M. M. Basko (1984), Fiz. Plasmy **10** p. 1195. [Sov. J. Plasma Phys. 10 (1984) 689].

[Bec76] F.D. Becchetti, C.E. Thorn and M.J. Levine (1976), Nucl. Instr. and Meth. **138** p. 93.

[Ber87] M. Berz and H. Wollnik (1987), Nucl. Instr. and Meth. A **258** p. 364.

[Ber91a] Julien Bergoz (1991), *Handbook for Fast Current Transformer for Heavy Ion Fusion at GSI*, *Technical report*, Bergoz.

[Ber91b] Julien Bergoz (1991), *Handbook for Integrating Current Transformer for Heavy Ion Fusion at GSI*, *Technical report*, Bergoz.

[Ber98] M. Berz (1998), Part. Accel. **24** p. 109.

[Bet30] H. Bethe (1930), Ann. Physik **5** p. 325.

[Bet32] H. Bethe (1932), Z. Phys. **76** p. 293.

[Bet70] H.D. Betz (1970), Phys. Rev. Lett. **25** p. 903.

[BF96]   O. Boine-Frankenheim and J. D'Avanzo (1996), Phys. Plasmas **3** p. 792.

[Bir52] J. B. Birks (1952), Phys. Rev. **86** p. 569.

[Bla02] A. Blazevic, H.G. Bohlen and W. von Oertzen (2002), Nucl. Instr. and Meth. B **190** p. 64.

[Blo33] F. Bloch (1933), Ann. Phys. (Leipzig) **16** p. 285.

[Bog99] S.D. Bogdanov, S.S. Bogdanov, E.E. Zhurkin and V.F. Kosmach (1999), Jorn. Exp. and Theor. Phys. **88** p. 220.

[Boh13] N. Bohr (1913), Philos. Mag. **25** p. 10.

[Boh41] N. Bohr (1941), Phys. Rev. **59** p. 270.

[Bor96] Th. Bornath, D. Kremp, W.D. Kraeft and M. Schlanges (1996), Phys. Rev. E **54** p. 3274.

[Bus93] A.V. Bushman, G.I Kanel, A.L. Ni and V.E. Fortov, *Intense Dynamic Loading of Condensed Matter* (Taylor&Francis, 1993).

[Con01] C. Constantin, E. Dewald, C. Niemann, S. Udrea, D. Varentsov, U.N. Funk, D.H.H. Hoffmann, J. Jacoby, U. Neuner, P. Spiller and A. Tauschwitz, in *GSI Scientific Report 2000*, GSI-2001-1 (GSI-Darmstadt, 2001), 129.

[Con02] C. Constantin (2002), *Multiple weak shock waves induced by heavy ion beams in solid matter*, Ph.D. thesis, Technische Universität Darmstadt.

[Cou94] C. Couillard, R. Deicas, Ph. Nardin, M.A. Beuve, J.M. Guihaumé and M. Renaud (1994), Phys. Rev. E **49** p. 1545.

[D'A92] J. D'Avanzo, M Lontano and P.F. Bortignon (1992), Phys. Rev. A **45** p. 6126.

[Dat96] S. Datz, H.F. Krause, C.R. Vane, H. Knudsen, P. Grafström and R.H. Schuch (1996), Phys. Rev. Lett. **77** p. 2925.

[Dew01] E. Dewald, C. Constantin, S. Udrea, D. Varentsov, J. Jacoby, U. Neuner, A. Tauschwitz, P. Spiller and D.H.H. Hoffmann, in *GSI Scientific Report 2000*, GSI-2001-1 (GSI-Darmstadt, 2001), 130.

[Die92] K.-G Dietrich, D.H.H. Hoffmann, E. Boggasch, J. Jacoby, H. Wahl, M. Elfers, C.R. Haas, V.P. Dubenkov and A.A. Golubev (1992), Phys. Rev. Lett. **69** p. 3623.

[Dor96] M. Dornik, V.P. Dubenkov, A. Filimonov, D.H.H. Hoffmann, M. Kulish, W. Laux, W. Seelig, B. Sharkov, P. Spiller, M. Stetter, C. Stöckl, S. Stöwe, W. Süß and H. Wetzler (1996), Fus. Eng. Des. **32–33** p. 511.

[Fan63] U. Fano (1963), Ann. Rev. Nucl. Sci. **13** p. 1.

[Fer40] E. Fermi (1940), Phys. Rev. **57** p. 485.

[For96] V.E. Fortov, B. Goel, C.D. Munz, A.L. Ni, A.V. Shutov and O. Yu. Vorobiev (1996), Nucl. Sci. Eng. **123** p. 169.

[For97] V.E. Fortov and I.V. Lomonosov (1997), J. Pure and Appl. Chem. **69** p. 893.

[For98] V.E. Fortov, K.V. Khishchenko, P.R. Levashov and I.V. Lomonosov (1998), Nucl. Instr. and Meth. A **415** p. 604.

[For01] V.E. Fortov, V.K. Gryaznov, V.B. Mintsev, V.Ya. Ternovoi, I.L. Iosilevski, M.V. Zhernokletov and M.A. Mochalov (2001), Contrib. Plasma Phys. **41** p. 215.

[Fri48] P. Frier, E.J. Lofgren, E.P. Ney and F. Oppenheimer (1948), Phys. Rev. **74** p. 1818.

[Fun98] U.N. Funk, R. Bock, M. Dornik, M. Giessel, M. Stetter, S. Stöwe, N. Tahir and D.H.H. Hoffmann (1998), Nucl. Instr. and Meth. A **415** p. 68.

[Fun99a] U.N. Funk (1999), *Aufbau und erster Einsatz einer Kryoanlage zur Herstellung von Wasserstofftargets für Experimente mit Schwerionenstrahlen*, Ph.D. thesis, Universität Erlangen-Nürenberg. GSI-DISS.99-02.

[Fun99b] U.N. Funk, R. Bock, M. Dornik, M. Geissel, D.H.H. Hoffmann, M. Kulish, F.B. Rosmej, M. Stetter, N. Shilkin, S. Stöwe, N.A. Tahir, A. Tauschwitz and V. Yakushev, in *High Energy Density in Matter Produced by Heavy Ion Beams*, GSI-99-04 (GSI-Darmstadt, 1999), 13.

[Gei98] H. Geissel and C. Scheidenberger (1998), Nucl. Instr. and Meth. B **136** p. 114.

[Ger99] D.O. Gericke and M. Schlanges (1999), Phys. Rev. E **60** p. 904.

[Ger02] D.O. Gericke, M. Schlanges and Th. Bornath (2002), Phys. Rev. E **65** p. 36406.

[Gol64] R. Gold (1964), *Report ANL-6984*, Argonne National Laboratory.

[Gol98] A. Golubev, M. Basko, A. Fertman, A. Kozodaev, N. Mesheryakov, B. Sharkov, A. Vishnevskiy, V. Fortov, M. Kulish, V. Gryaznov, V. Mintsev, E. Golubev, A. Pukhov, V Smirnov, U. Funk, S. Stoewe, M. Stetter, H.-P. Flierl, D.H.H. Hoffmann, J. Jacoby and I. Iosilevski (1998), Phys. Rev. E **57** p. 3363.

[Gol01] A. Golubev, V. Turtikov, A. Fertman, I. Roudskoy, B. Sharkov, M. Geissel, U. Ne-
         uner, M. Roth, A. Tauschwitz, H. Wahl, D.H.H. Hoffmann, U. Funk, W. Süß and
         J. Jacoby (2001), Nucl. Instr. and Meth. A **464** p. 247.

[Gry98] V.K. Gryaznov, V.E. Fortov and I.L. Iosilevski (1998), Nucl. Instr. and Meth. A **415**
         p. 581.

[Gry99] V.K. Gryaznov, I.L. Iosilevski and V.E. Fortov (1999), Contrib. Plasma Phys. **39** p.
         3363.

[Hei54] W. Heitler, *The Quantum Theory of Radiation* (Oxford University Press, 1954), 3
         edition.

[Hem89] R.J. Hemley, C.S. Zha, A.P. Jephcoat, H.K. Mao, L.W. Finger and D.E. Cox (1989),
         Phys. Rev. B **39** p. 11820.

[Hof88] D.H.H. Hoffmann, K. Weyrich, H. Wahl, T. Peter, J. Jacoby, R. Bimbot, D. Gardes,
         M.F. Rivet, C. Fleurier, C. Deutsch, R. Noll and R. Haas (1988), Z. Phys. A **30** p.
         339.

[Hof90] D.H.H. Hoffmann, K. Weyrich, H. Wahl, D. Gardés, R. Bimbot and C. Fleurier
         (1990), Phys. Rev. A **42** p. 2313.

[Hof94] D.H.H. Hoffmann, J. Jacoby, W. Laux, M. de Magistris, E. Boggasch, P. Spiller,
         C. Stöckl, A. Tauschwitz, K. Weyrich, M. Chabot and D. Gardes (1994), Nucl.
         Instr. and Meth. B **90** p. 1.

[Hof00] D.H.H. Hoffmann, R. Bock, A.Ya. Faenov, U. Funk, M. Geissel, U. Neuner, T.A.
         Pikuz, F. Rosmej, M. Roth, W. Süß, N. Tahir and A. Tauschwitz (2000), Nucl. Instr.
         and Meth. B **161–163** p. 9.

[Hof01] I. Hofmann, O. Boine-Frankenheim, R.W. Hasse, Y Liu and P. Spiller, in *High
         Energy Density in Matter Produced by Heavy Ion Beams*, GSI-2001-4 (GSI-
         Darmstadt, 2001), 29.

[Hof02] D.H.H. Hoffmann, V.E. Fortov, I.V. Lomonosov, N.A. Tahir, D. Varentsov and
         J. Wieser (2002), Phys. Plasmas Lett. **9** p. 3651.

[Hub89] F. Hubert, R. Bimbot and H. Gauvin (1989), Nucl. Instr. and Meth. B **36** p. 357.

[Hub90] F. Hubert, R. Bimbot and H. Gauvin (1990), Atom. Data and Nucl. Data Tables
         46 p. 1.

[ICR93] ICRU-49 (1993), *Stopping Powers of Protons and Alpha Particles*, *Technical report*,
         Intl. Comm. on Rad. Units.
         URL http://physics.nist.gov/PhysRefData/

[Ign02] Lj.M. Ignjatović and A.A. Mihajlov (2002), J. Quant. Spectr. and Radiat. Trans. **72**
         p. 677.

[Ios02] I.L. Iosilevski (2002), *private communications*.

[Jac72] J.D. Jackson and R.L. McCarthy (1972), Phys. Rev. B **6** p. 4131.

[Jac75] J.D. Jackson, *Classical Electrodynamics* (John Wiley, 1975), 2 edition.

[Jac89] J. Jacoby (1989), *Untersuchungen zur Erzeugung hoher Energiedichte in Materie mit
         intensiven Schwerionenstrahlen*, Ph.D. thesis, Universität Heidelberg. GSI.DISS-
         89-24.

[Jac90] J. Jacoby, D.H.H. Hoffmann, R.W. Müller, K. Mahrt-Olt, R.C. Arnold, V. Schneider
         and J. Maruhn (1990), Phys. Rev. Lett. **65** p. 2007.

[Jac95] J. Jacoby, D.H.H. Hoffmann, W. Laux, R.W. Müller, H. Wahl, K. Weyrich, E. Bog-
         gasch, B. Heimrich, C. Stöckl, H. Wetzler and S. Miyamoto (1995), Phys. Rev. Lett.
         74 p. 1550.

[Jan70] P.A. Jansson (1970), J. Opt. Soc. Am. **60** p. 184.

[Ker83] G.I Kerley, *Molecular Based Studies of Fluids* (Amer. Chemical Soc., Washington DC, 1983), 107.

[Khi98] K.V. Khishchenko, I.V. Lomonosov and V.E. Fortov (1998), High Temp. High Press. **30** p. 373.

[Kle77] M.K. Klein and J.A. Venables (eds.), *Rare Gas Solids*, volume 1,2 (Academic Press, New York, 1977).

[Kox87] S. Kox, A. Gamp, C. Perrin, J. Arvieux, R. Bertholet, J.F. Bruandet, M. Buenerd, R. Cherkaoui, A.J. Cole, Y. El-Masri, N. Longequeue, J. Menet, F. Merchez and J.B. Viano (1987), Phys. Rev. C **35** p. 1678.

[Kra86] W.D. Kraeft, D. Kremp, W. Ebeling and G. Röpke, *Quantum Statistics of Charge Particle Systems* (Plenum, 1986).

[Krä00] M Krämer, O. Jäkel, T. Haberer, G. Kraft, D. Schardt and U. Weber (2000), Phys. Med. Biol. **45** p. 3299.

[Krö91] W. Krötz, A. Ulrich, B. Busch, G. Ribitzki and J. Wieser (1991), Phys. Rev. A **43** p. 6089.

[Lan76] D. Landau and E.M. Lifshitz, *Course of Theoretical Physics*, volume 5 (Pergamon, 1976). [Nauka, Moscow, 1995].

[Leh98] A. Leharch (1998), *Erarbeitung und Umsetzung eines Konzepts zur Beschleunigung polarisierter Protonen im Kühlersynchrotron COSY*, Ph.D. thesis, Forschungszentrum Jülich. Jül-3501.

[Li00] G. Li, U. Czok, A. Kalimov, M. Winkler and H. Wollnik (2000), Rev. Sci. Instr. **71** p. 376.

[Lin76] J. Lindhard (1976), Nucl. Instr. and Meth. **132** p. 1.

[Lin96] J Lindhard and A.H. Sørensen (1996), Phys. Rev. A **53** p. 2443.

[Lom02] I.V. Lomonosov (2002), *private communications*.

[Mac74] H. D. Maccabee and M. A. Ritter (1974), Radiat. Res. **60** p. 409.

[Mat99] N. Matsufuji, T. Kanai, H. Komami and T. Kohno (1999), Nucl. Instr. and Meth. A **437** p. 346.

[May01a] G. Maynard, K. Katsonis, C. Deutsch, G. Zwicknagel, M. Chabot and D. Gardés (2001), Nucl. Instr. and Meth. A **464** p. 86.

[May01b] G. Maynard, G Zwicknagel, C. Deutsch and K. Katsonis (2001), Phys. Rev. A **63** p. 52903.

[Meh81] T. A. Mehlhorn (1981), J. Appl. Phys. **52** p. 6522.

[Mic95] K. Michaelian, A. Menchaca-Rocha and E. Belmont-Moreno (1995), Nucl. Instr. and Meth. A **356** p. 297.

[Mot29] N. F. Mott (1929), Proc. Roy. Soc. London A **124** p. 425.

[Mot32] N. F. Mott (1932), Proc. Roy. Soc. London A **135** p. 429.

[MR99] A. Menchaca-Rocha, M. Buénerd, L. Gallin-Martel, F. Ohlsson-Malek and T. Thuillier (1999), Nucl. Instr. and Meth. A **438** p. 322.

[Nar78] E. Nardi, E. Peleg and Z. Zinamon (1978), Phys. Fluids **21** p. 574.

[Neu00] U. Neuner, R. Bock, M. Roth, P. Spiller, C. Constantin, U.N. Funk, M. Geissel, S. Hakuli, D.H.H. Hoffmann, J. Jacoby, A. Kozyreva, N.A. Tahir, S. Udrea, D. Varentsov and A. Tauschwitz (2000), Phys. Rev. Lett. **85** p. 4518.

[Neu01] U. Neuner, R. Bock, C. Constantin, E. Dewald, U.N. Funk, M. Geissel, D.H.H. Hoff-
         mann, J. Jacoby, A. Kozyreva, D. Penache, P. Pirzadeh, F.B. Rosmej, O. Rosmej,
         M. Roth, W. Süß, N.A. Tahir, A. Tauschwitz, S. Udrea, D. Varentsov and H. Wahl
         (2001), Nucl. Instr. and Meth. A **464** p. 326.

[Nor63] L. C. Northcliffe (1963), Ann. Rev. Nucl. Sci. **13** p. 67.

[Nor70] L.C. Northcliffe and R.F. Schilling (1970), Nucl. Data Tables A **7** p. 233.

[Pau01] H. Paul and A. Schinner (2001), Nucl. Instr. and Meth. B **179** p. 299.
         URL http://www.exphys.uni-linz.ac.at/stopping/MstarWWW/

[Pet91] Th. Peters and J. Meyer-ter Vehn (1991), Phys. Rev. A **43** p. 2015.

[Pet01] A. Peters, P. Forck, A. Weiss and A. Bank, in *DIPAC Proceedings* (2001).

[Pie68] T.E. Piece and M. Blann (1968), Phys. Rev. **173** p. 390.

[Ree01] N. Reeg and N. Schneider, in *DIPAC Proceedings* (2001).

[Rot00] M. Roth, C. Stöckl, W. Süß, O. Iwase, D.O. Gericke, R. Bock, D.H.H. Hoffmann,
         M. Geissel and W. Seelig (2000), Europhys. Lett. **50** p. 28.

[Roz96] J.P. Rozet, D. Vernhet and C. Stéphan (1996), Nucl. Instr. and Meth. B **107** p. 67.

[Rut11] E. Rutherford (1911), Philos. Mag. **21** p. 669.

[Sal98] M. Salvermoster, A. Ulrich and J. Wieser (1998), Phys. Rev. E **58** p. 6531.

[Sch71] W. Schimmerling, K. Vosburgh, P. Todd and C.B. Schroy (1971), Science **174** p.
         1123.

[Sch89] W. Schimmerling, J. Miller, M. Wang, M. Rapkin, J. Howard, H.G. Spieler and B.V.
         Jarret (1989), Radiat. Res. **120** p. 36.

[Sch93] I. Schall, D. Schardt, H. Geissel, H. Irnich, G. Kraft, A. Magel, M.F. Mohar,
         G. Münzenberg, F. Nickel, C. Scheidenberger, W. Schwab and L. Sihver (1993),
         Radiat. Eff. and Def. in Solids **126** p. 385.

[Sch96a] I. Schall, D. Schardt, H. Geissel, H. Irnich, G. Kraft, A. Magel, M.F. Mohar,
         G. Münzenberg, F. Nickel, C. Scheidenberger and W. Schwab (1996), Nucl. Instr.
         and Meth. B **117** p. 221.

[Sch96b] A. Schamass, N. Schneider and R. Steiner (1996), *A Beam Intensity Monitor
         for Synchrotron Beams with Fast Beam Extraction Mode*, *Technical report*, GSI-
         Darmstadt. Unpublished; H. Reeg, private communications.

[Sch96c] D. Schardt, I. Schall, H. Geissel, H. Irnich, G. Kraft, A. Magel, M.F. Mohar,
         G. Münzenberg, F. Nickel, C. Scheidenberger, W. Schwab and L. Sihver (1996),
         Adv. Space Res. **17** p. 87.

[Sch96d] C. Scheidenberger, H. Geissel, H.H. Mikkelsen, F. Nickel, S. Czajkowski, H. Fol-
         ger, H. Irnich, G. Münzenberg, W. Schwab, Th. Stöhlker, T. Suzuki and B. Voss
         (1996), Phys. Rev. Lett. **77** p. 3987.

[Sch97] C. Scheidenberger and H. Geissel (1997), *Penetration of Relativistic Heavy Ions
         Through Matter*, *Preprint GSI-97-34*, GSI-Darmstadt.

[Sch98a] C. Scheidenberger, Th. Stöhlker, W.E. Meyerhof, H. Geissel, P.H. Mokler and
         B. Blank (1998), Nucl. Instr. and Meth. B **142** p. 441. The program CHARGE is
         available at the GSI under UNIX and VMS.
         URL http://www.gsi.de/~scheid/charge.html

[Sch98b] M. Schlanges, D.O. Gericke, W.D. Kraeft and Th. Bornath (1998), Nucl. Instr.
         and Meth. A **415** p. 517.

[Sch99] G. Schiwietz and P.L. Grande (1999), Nucl. Instr. and Meth. B **153** p. 1.
         URL http://www.hmi.de/people/schiwietz/casp.html

[Sch01a] V. Schaa (2001), *private communications*.

[Sch01b] C. Scheidenberger (2001), *private communications*.

[Sea88] M.P. Seah, W.A. Dench, B. Gale and T.E. Groves (1988), J. Phys. E: Sci. Instrum. **21**(4) p. 351.

[Shu02] A. Shutov (2002), *private communications*.

[Sig98] P. Sigmund (1998), Nucl. Instr. and Meth. B **135** p. 1.

[Sig01] P. Sigmund and A. Schinner (2001), Nucl. Instr. and Meth. B **174** p. 535.

[Sig02] P. Sigmund and A. Schinner (2002), Nucl. Instr. and Meth. B In print.

[Sne99] R.J.M. Snellings, W. Hulsbergen, E.P. Prendergast, A. van den Brink, A.P. de Haas, J.J.L.M. Habets, R. Kamermans, M. Koopmans, P.G. Kuijer, C.T.A.M. de Laat, R.W. Ostendorf, A. Péghaire and M. Rossewij (1999), Nucl. Instr. and Meth. A **438** p. 368.

[Sør02] A. H. Søresen (2002), Nucl. Instr. and Meth. B In print.

[Spi93] P. Spiller, M. Winkler, A. Tauschwitz, D.H.H. Hoffmann and H. Wollnik (1993), Il Nuovo Cimento A **106** p. 1719.

[Spi99] P. Spiller (1999), *private communication*.

[Ste71] R.M. Sternheimer and R.F. Peierls (1971), Phys. Rev. B **3** p. 3681.

[Ste93] M. Stetter, J. Christiansen, U. Neuner, S. Stöwe, R. Tkotz, T. Wagner, E. Boggasch, A. Tauschwitz, D.H.H. Hoffmann and P. Spiller (1993), Il Nuovo Cimento A **106** p. 1725.

[Ste96] M. Stetter, U. Neuner, S. Stöwe, M. Dornik, D.H.H. Hoffmann, R. Kowalewicz, P. Spiller and A. Tauschwitz (1996), Fus. Eng. Des. **32-33** p. 503.

[Stö96] C. Stöckl, O. Boine-Frankenheim, M. Roth, W. Süß, H. Wetzler, W. Seelig, M. Kulish, M. Dornik, W. Laux, P. Spiller, M. Stetter, S. Stöwe, J. Jacoby and D.H.H. Hoffmann (1996), Laser and Part. Beams **14** p. 561.

[Stö98] S. Stöwe, R. Bock, M. Dornik, P. Spiller, M. Stetter, V.E. Fortov, V. Mintsev, M. Kulish, A. Shutov, V. Yakushev, B. Sharkov, A. Golubev, B. Bruynetkin, U.N. Funk, M. Geissel, Hoffmann. D.H.H. and N.A. Tahir (1998), Nucl. Instr. and Meth. A **415** p. 61.

[Tah98] N.A. Tahir, D.H.H. Hoffmann, J.A. Maruhn, K.-J. Lutz and R. Bock (1998), Phys. Lett. A **249** p. 489.

[Tah99] N.A. Tahir, D.H.H. Hoffmann, J.A. Maruhn, P. Spiller and R. Bock (1999), Phys. Rev. E **60** p. 4715.

[Tah00a] N.A. Tahir, D.H.H. Hoffmann, A. Kozyreva, A. Shutov, J.A. Maruhn, U. Neuner, A. Tauschwitz, P. Spiller and R. Bock (2000), Phys. Rev. E **62** p. 1224.

[Tah00b] N.A. Tahir, D.H.H. Hoffmann, A. Kozyreva, A. Shutov, J.A. Maruhn, U. Neuner, A. Tauschwitz, P. Spiller and R. Bock (2000), Phys. Rev. E **61** p. 1975.

[Tah01a] N.A. Tahir, D.H.H. Hoffmann, A. Kozyreva, A. Tauschwitz, A. Shutov, J.A. Maruhn, P. Spiller, U. Neuner, J. Jacoby, M. Roth, R. Bock, H. Juranek and R. Redmer (2001), Phys. Rev. E **63** p. 16402.

[Tah01b] N.A. Tahir, A. Kozyreva, P. Spiller, D.H.H Hoffmann and A. Shutov (2001), Phys. Plasmas **8** p. 611.

[Tah02a] N.A. Tahir (2002), *private communications*.

[Tah02b] N.A. Tahir, A. Shutov, D Varentsov, D.H.H. Hoffmann, P. Spiller, I. Lomonosov, J. Wieser and J. Jacoby (2002), Laser and Part. Beams In print.

[Tah02c] N.A. Tahir, A. Shutov, D. Varentsov, P. Spiller, D.H.H. Hoffmann, I. Lomonosov, J. Wieser, M. Kirk, R. Piriz, V.E. Fortov and R. Bock (2002), Phys. Rev. E Submitted.

[Tik77] A. N. Tikhonov and V.Y. Arsenin, *Solutions of Ill-Posed Problems* (Wiley, 1977).

[Tik87] A. N. Tikhonov and A.V. Goncharsky (eds.), *Ill-Posed Problems in the Natural Sciences* (MIR, 1987).

[Tow88] L.W. Townsend and J.W. Wilson (1988), Phys. Rev. C **37** p. 892.

[Udr01] S. Udrea, E. Dewald, C. Constantin, D. Varentsov, J. Jacoby, U. Neuner, A. Tauschwitz, P. Spiller and D.H.H. Hoffmann, in *GSI Scientific Report 2000*, GSI-2001-1 (GSI-Darmstadt, 2001), 128.

[Udr02] S. Udrea (2002), Ph.D. thesis, Technische Universität Darmstadt.

[van31] P.H. van Cittert (1931), Z. Phys. **69** p. 298.

[Var98a] D. Varentsov (1998), *Development and tests of a pulsed strip-line spectrometer for energetic heavy ion beams*, Master's thesis, St.-Petersburg Tech. Univ. / GSI-Darmstadt.

[Var98b] D. Varentsov, H. Eickhoff, U. Funk, P. Spiller and S. Stöwe, in *GSI Scientific Report 1997*, GSI-1998-1 (GSI-Darmstadt, 1998), 177.

[Var98c] D. Varentsov, N.A. Tahir, A. Shutov and P. Spiller (1998), *internal report*, GSI-Darmstadt, PP. Unpublished.

[Var99] D. Varentsov, D.H.H. Hoffmann, U. Neuner, P. Spiller and A. Tauschwitz, in *GSI Scientific Report 1998*, GSI-1999-1 (GSI-Darmstadt, 1999), 113.

[Var00a] D. Varentsov, in *17th International Conference on Physics of High Energy Density in Matter* (2000).

[Var00b] D. Varentsov, P. Spiller, U. Neuner and D.H.H. Hoffmann, in *GSI Scientific Report 1999*, GSI-2000-1 (GSI-Darmstadt, 2000), 126.

[Var01] D. Varentsov, P. Spiller, U.N. Funk, D.H.H. Hoffmann, A. Kozyreva, N.A. Tahir, C. Constantin, E. Dewald, J. Jacoby, U. Neuner, S. Udrea and R. Bock (2001), Nucl. Instr. and Meth. B **174** p. 215.

[Var02a] D. Varentsov, P. Spiller, H. Eickhoff and D.H.H. Hoffmann (2002), Nucl. Instr. and Meth. A **485** p. 238.

[Var02b] D. Varentsov, P. Spiller, N.A. Tahir, D.H.H. Hoffmann, C. Constantin, E. Dewald, J. Jacoby, I.V. Lomonosov, U. Neuner, A. Shutov, J. Wieser, S. Udrea and R. Bock (2002), Laser and Part. Beams In print.

[Vol66] R. Voltz and J. Lopes da Silva (1966), J. Chem. Phys. **45** p. 3306.

[Vor97] O. Vorobiev, A. Shutov, I.N. Lomov, D.A. Shishov, S.A. Medin and V.E. Fortov (1997), Int. J. Impact Eng. **20** p. 805.

[Wea02] B.A. Weaver and A.J. Westphal (2002), Nucl. Instr. and Meth. B **187** p. 285. URL http://ultraman.ssl.berkeley.edu/~weaver/dedx/

[Web73] W.R. Webber, J.A. Lezniak and J. Kish (1973), Nucl. Instr. and Meth. **111** p. 301.

[Wei00a] H. Weick, H. Geissel, C. Scheidenberger, F. Attallah, T. Baumann, D. Cortina, M. Hausmann, B. Lommel, G. Münzenberg, N. Nankov, F. Nickel, T. Radon, H. Schatz, K. Schmidt, J. Stadlmann, K. Sümmerer, M. Winkler and H. Wollnik (2000), Nucl. Instr. and Meth. B **164** p. 168.

[Wei00b] H. Weick, H. Geissel, C. Scheidenberger, F. Attallah, D. Cortina, D. Hausmann, G. Münzenberg, T. Radon, H. Schatz, K. Schmidt, J. Stadlmann, K. Sümmerer and M. Winkle (2000), Phys. Rev. Lett. **85** p. 2725.

[Wei02] H. Weick, A.H. Søresen, H. Geissel, C. Scheidenberger, F. Attallah, V. Chichkine, S. Elisseev, M. Hausmann, H. Irnich, Y. Litvinov, B. Lommel, M. Maier, M. Mato, G. Münzenberg, N. Nankov, F. Nickel, W. Schwab, Th. Stöhlker, K. Sümmerer and B. Voss (2002), Nucl. Instr. and Meth. B **193** p. 1.

[Wet97] H. Wetzler, W. Süß, C. Stöckl, A. Tauschwitz and D.H.H. Hoffmann (1997), Laser and Part. Beams **15** p. 449.

[Wie88] J. Wieser (1988), *Bestimmung der Ansprechfunktion eines optischen Monochromator-Detektor-Systems und Messung der Lichtemission von Edelgastargets bei Schwerionenstrahlanregung*, Master's thesis, Technische Universität München.

[Wie00] J. Wieser (2000), *Time Resolved Determination of Temperatures in Heavy Ion Beam Induced Plasmas*, *proposal for Experimental Committee S255*, GSI-Darmstadt. Accepted Dec. 2000.

[Win94] M. Winkler, G. Li, C. Weil, H. Wollnik, P. Spiller, D.H.H. Hoffmann and A. Tauschwitz (1994), Nucl. Instr. and Meth. A **344** p. 455.

[Win96] M. Winkler, H. Wollnik, B. Pfreundtner, E.I. Esch and P. Spiller (1996), Fus. Eng. Des. **32-33** p. 386.

[Wol87] H. Wollnik, *Optics of charged particles* (Academic Press Inc., 1987).

[Xu94] Ch. Xu, I. Assaoui and S. Jacquery (1994), J. Opt. Soc. Am. A **11**(11) p. 2804.

[Yam92] S. Yamada, H. Ogawa, K. Kawachi, N. Araki, M. Kanazawa, A. Kitagawa, T. Kohno, M. Kumada, T. Murakami, M. Muramatsu, K. Noda, S. Sato, Y. Sato, E. Takada, A. Tanaka, K. Tashiro, M. Torikoshi, J. Yoshizawa, M. Endo, Y. Furusawa, T. Kanai, H. Koyama-Ito, N. Matsufuji, S. Minohara, N. Miyahara, F. Soga, M. Suzuki, H. Tomura, Y. Hirao, K. Sato and A. Itano (1992), Nucl. Phys. A. **588** p. 229c.

[Zar95] E. Zaremba, A. Arnau and P.M. Echenique (1995), Nucl. Instr. and Meth. B **96** p. 619.

[Zel67] Ya.B. Zel'dovich and Yu.P. Raizer, *Physics of Shock Waves and High-Temperature Hydrodynamic Phenomena*, volume 2 (Academic Press, 1967).

[Zhu00] E.E. Zhurkin and S.D. Bogdanov (2000), Nucl. Instr. and Meth. B **164** p. 230.

[Zie96] J.F. Ziegler, J.P Biersack and U. Littmark, *The Stopping and Ranges of Ions in Solids* (Pergamon, New York, 1996).
URL http://www.srim.org/

[Zwi99] G. Zwicknagel, C. Toepffer and P.-G. Reinhard (1999), Phys. Rep. **309** p. 117.

Acknowledgments

At the end of my work, I am very glad to have the opportunity to express my gratitude to the people whose collaboration and support have made the completion of this work ever possible. For the last five years my research activities have concentrated on high-energy-density matter studies and heavy-ion plasma physics as well as on accelerator physics and engineering, and the pleasure of coming to understand some of these things really well has been surpassed only by the pleasure of working with extraordinary people who were just as consumed by the topic: the members of the Plasma Physics Group and Accelerator Division at the GSI.

First of all, I am happy to acknowledge Prof. Dr. Dr.h.c. Dieter H.H. Hoffmann for his invaluable encouragement, support and advice on every aspect of the work as well as for his kind care and friendly assistance that was always there even besides the professional activities.

I am particularly indebted to my friend and collaborator, Dr. Naeem A. Tahir for his expert help in all the aspects of the theoretical interpretation and understanding of the results of my work. Without his assistance, performing the sophisticated computer simulations would not be possible. He also has generously provided detailed comments on the thesis that has improved its quality significantly. I thank him for his advice and his effort.

It also has been a pleasure to me during all the past years to work hand in hand with Dr. Peter Spiller. His wonderful guidance, plenty of fruitful discussions we had, his indispensable knowledge in many different fields and his tremendous enthusiasm have enriched the progress of my work dramatically. Many of the important ideas of this work originated with him.

I deeply appreciate the great help in preparation of our experiments and sharing with me the long and difficult beamtime shifts by the entire HHT experimental team, all the graduate students, postdoctoral fellows and researchers: Carmen Constantin, Dr. Eduard Dewald, Dr. Ulrich Funk, Udo Geißler, Dr. Joachim Jacoby, Dr. Ulrich Neuner, Serban Udrea and Dr. Jochen Wieser. In particular, I would like to thank Dr. Ulrich Funk, who provided me with a lot of important knowledge about the HHT experimental area and who was very helpful during many of my experiments. The elaborate cryogenic target preparation system developed and constructed by him at the HHT has enabled me to do the present experiments with the RGS targets. Interesting discussions and prompt assistance in all experimental activities during the final stages of my work by Dr. Jochen Wieser have also to be greatly acknowledged.

I wish to especially thank my collaborators from the IPCP, Chernogolovka, Russia for their important contributions to this work. It is a pleasure to acknowledge the great help by Prof. Dr. Igor Lomonosov in making me understand the subject of the equation-of-state physics. He developed a new model for the **Ne** EOS, specially to interpret the experimental results of my work. I am also grateful to him for

many useful discussions, helpful suggestion and wonderful friendship. The help of Alexander Shutov in developing the BIG-2 code and carrying out simulations of the experiments, is highly appreciated. Finally, I like to thank the other collaborators from Chernogolovka, including Michail Kulish and Dr. Victor Gryaznov for many illuminating discussions.

I would also like to express my gratitude:

To Dr. Hartmut Eickhoff, who was my first supervisor at the GSI and who got me interested in the GSI activities.

To Walter Bourgeois, whose help in all the construction work and manufacturing of the experimental devices, including the SBP spectrometer and pulsed high current magnets was absolutely essential. I am also indebted to the TU and GSI workshop people for their efficient work.

To the entire GSI Plasma Physics Group for being wonderful colleagues and for very pleasant time spent together: Vladimir Arsov, Abel Blazevic, Erik Brambrink, Matthias Geißel, Anna Kozyreva, Christoph Niemann, Dan Penache, Pascal Pirzadeh, Frank and Olga Rosmej, Markus Roth, Malene Rytter, Theodor Schlegel, Andreas Tauschwitz, Heinrich Wahl and Karin Weyrich.

Last but not least, I am very grateful for the continuous encouragement and support of my family during this work as well as during my whole life. I would like to specially thank my father, Dr. Victor Varentsov, who being a good physicist himself made me interested in physics, and indeed for his invaluable advice that is guiding me both in physics and elsewhere. My special thanks also go to my mother, Dr. Elena Varentsova, who with her love, wisdom and patience is softening the advice of my father... This thesis is dedicated to them, with gratitude and affection.

Curriculum Vitae

Name:	**Dmitry V. Varentsov**
Birth date / place:	September 1, 1975 / Saint-Petersburg, Russia
Citizenship:	Russian

EDUCATIONAL PROFILE:

1982–1988	Primary and secondary school in St.-Petersburg.
1988–1992	High-school for Mathematics and Physcis in St.-Petersburg.
1992–1998	**B. Sc.** at the State Technical University (STU) of St.-Petersburg, 1996. Thesis: *"Space charge effects of pulsed beams in isotrajectory dynamics"*, advisor: Dr. A. Matyshev.
	M. Sc. with honor at the STU St.-Petersburg, 1998. Thesis: *"Development and tests of a pulsed strip-line spectrometer for energetic heavy ion beams"*, advisors: Dr. O. Tsybin (STU, St.-Petersburg) and Dr. H. Eickhoff (GSI, Darmstadt).
	Awarded and named as a "Soros Student" by International Soros Science Education Program in 1994, 1995 and 1996. Participated in the GSI Summer Student Program, 1996.
since Oct. 1998	**Ph.D. student** at the Technical University of Darmstadt and GSI-Darmstadt, Germany. Since Jul. 1999 a member of *Graduiertenkolleg "Physik und Technik von Beschleunigern" (GRAKO)*.

Hiermit erkläre ich, daß ich die Arbeit selbständig und nur mit den angegebenen Hilfsmitteln angefertigt und nicht schon früher eine Promotion versucht habe.

14. Oktober 2002   Dmitry Varentsov